

Jet fragmentation kinematics and the analysis $\pi^0 - h^\pm$ azimuthal correlations in $p + p$ collisions

J. Rak, M. Tannenbaum

September 16, 2005

Abstract

This analysis note discusses an extraction of $\sqrt{\langle j_T^2 \rangle}$ and $\sqrt{\langle k_T^2 \rangle}$ from the two-particle correlation function. Similar analysis of the fixed- p_T correlations has been already discussed in [1]. Here we focus on $\pi^0 - h^\pm$ correlation function, we discuss an extraction of the fragmentation function from the shape analysis of associated x_E -distributions, we give more details on k_T -smearing and momentum unbalance which has not been taken into account in [1].

Contents

1	Introduction	3
1.1	Formulae for $\langle j_T \rangle$ and $\langle k_T \rangle$	3
1.2	Run-2/run-3 comparison	5
1.3	Assorted correlations	6
2	What do we learn from pythia?	13
2.1	Conditional distributions	14
2.2	k_T -unbalance	16
2.3	Width and yields from pythia and data	17
3	k_T-smearing.	19
3.1	2D Lorentz invariant smearing.	19
4	Fragmentation function	22
4.1	Inclusive fragmentation	22
4.2	Associated x_E distributions	23
4.3	Conditional fragmentation	23
4.4	Fragmentation function from the combined fit	27
4.4.1	Effective “ k_T smeared” $f_Q(\hat{p}_T)$ and D_π^q distributions	28
4.4.2	Unsmeared $f_Q(\hat{p}_T)$ and D_π^q distributions	30
5	$\langle k_T \rangle$ results	33
6	Summary	36
A	Appendix	37
A.1	First and second moments of normally distributed quantities	37
A.2	The correct way to analyze the azimuthal correlation function.	37
A.3	$f_Q(\hat{p}_T)$ parameterizations for the case of $\hat{p}_T \rightarrow 0$ and $\hat{p}_T \rightarrow \sqrt{s}/2$	39
A.4	Resolution Smearing of a Momentum Spectrum	39
A.4.1	1D smearing.	40
A.4.2	2D vector smearing.	40
A.4.3	Lorentz transform formulae	43
A.5	Fragmentation function with parton momentum	44
A.6	π^0 reconstruction in run-3 data	44
A.7	Data tables	46

1 Introduction

This is an extension of an $\langle j_T \rangle$, $\langle k_T \rangle$ analysis (notation summarized in App. B) presented in [1] where only $h^\pm - h^\pm$ correlation in fixed p_T -bins (transverse momentum of the trigger particle, p_{Tt} , is equal to the momentum of the associated particle, p_{Ta}) were studied. In order to fully explore the kinematics of the hard scattering events we performed an analysis of assorted $\pi^0 - h^\pm$ correlations ($p_{Tt} \neq p_{Ta}$) where significantly higher p_T -region is accessible.

In addition to what has been shown in [1] an effect of k_T -smearing is discussed in section 3. The impact of k_T -smearing and momentum unbalance which leads to the modification of formulae used for evaluation of $\langle z_t \rangle \sqrt{\langle k_T^2 \rangle}$ from the measured width of the near and away-side correlation peak is discussed in 1.1. The detailed discussion on the extraction of the fragmentation function, based on the simultaneous analysis of associated π^0 -inclusive p_T and associated x_E distributions, is presented in section 4.2. The main issue here which was not taken into account in the previous analysis is related to the fact that despite the naive expectation, the $\langle z_t \rangle$ values depend not only on the magnitude of p_{Tt} but also on p_{Ta} . It was expected that the trigger particle momentum determines the hardness, $\langle Q^2 \rangle$, of the scattering and thus the $\langle z_t \rangle$ value is determined solely by the magnitude of p_{Tt} . This assumption turns out to be incorrect. The variation of p_{Ta} affects the parton distribution function of the trigger jet and thus the $\langle z_t \rangle$ is a function of both p_{Tt} and p_{Ta} (see section 4.3).

This analysis focuses on $\pi^0 - h^\pm$ correlations, where π^0 is used as a trigger particle. Direct identification of π^0 particles via two-photons invariant mass distribution allows to trigger on much higher jets momenta than it would be in the case of unidentified charge particle track, where the particle tracks of $p_T > 4.5\text{-}5 \text{ GeV}/c$ are dominated by background coming from low- p_T particles decaying deep inside the magnetic field region.

1.1 Formulae for $\langle j_T \rangle$ and $\langle k_T \rangle$

The relation between the angular width of the correlation peak and $\langle |j_{Ty}| \rangle$ and $\langle z \rangle \langle |k_{Ty}| \rangle$ were discussed in [1] (see Eq. (18) and (20)). Here we would like to explore more general case of assorted correlations and, more importantly, in [1] we did not account for a jet momenta unbalance which has to be present whenever asymmetric correlations ($p_{Tt} \neq p_{Ta}$) are studied.

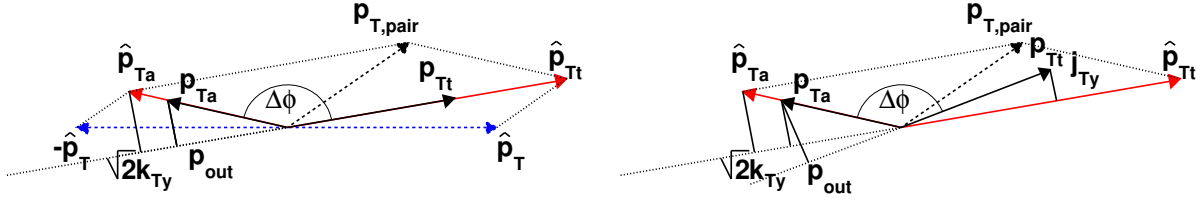


Figure 1: (a) Schematic view of a hard scattering event in the plane perpendicular to the beam. Two scattered partons with transverse momenta \hat{p}_T in partons' center of mass frame are seen in the laboratory frame to have momenta \hat{p}_{Tt} and \hat{p}_{Ta} . The net pair transverse momentum $\hat{p}_{T,pair}$ corresponds to the sum of two \vec{k}_T -vectors of the trigger and associated jet. The trigger and associated jet fragment producing high- p_T particles labeled as p_{Tt} and p_{Ta} . The projection of k_T perpendicular to \hat{p}_{Tt} is labeled as k_{Ty} . The transverse momentum component of the away-side particle p_{Ta} perpendicular to trigger particle \hat{p}_{Tt} is labeled as p_{out} . (b) The same schematics as on (a), but the jet fragmentation transverse momentum component j_{Ty} of the trigger jet is also shown.

For two particles with transverse momenta p_{Tt} , p_{Ta} from the same jet, the width of the near-side correlation can be related to the RMS value of the two-dimensional vector j_T as¹

$$\sigma_N^2 = \langle \Delta\phi^2 \rangle = \left\langle \left(\frac{j_{Ty}}{p_{Ta}} \right)^2 + \left(\frac{j_{Ty}}{p_{Tt}} \right)^2 \right\rangle$$

where we assume $\sqrt{\langle j_{Ty}^2 \rangle} \ll p_{Tt}$ and p_{Ta} and thus the asin function can be approximated by its argument and we can solve for $\sqrt{\langle j_{Ty}^2 \rangle}$

$$\sqrt{\langle j_T^2 \rangle} = \sqrt{2 \langle j_{Ty}^2 \rangle} \simeq \sqrt{2} \frac{p_{Tt} \cdot p_{Ta}}{\sqrt{p_{Tt}^2 + p_{Ta}^2}} \sigma_N. \quad (1)$$

¹For relations between $\sqrt{\langle X^2 \rangle}$ and $\langle |X_y| \rangle$, where X is any 2D quantity, see App.A.1

In order to extract $\langle |k_{Ty}| \rangle$, or $\langle k_T^2 \rangle$, we start with the relation between the magnitude of

$$p_{\text{out}} = p_{Ta} \sin \Delta\phi \quad (2)$$

the transverse momentum component of the away-side particle \vec{p}_{Ta} perpendicular to trigger particle \vec{p}_{Tt} in the azimuthal plane (see Fig. 1), and k_{Ty} , from references [4] and [5]

$$\langle |p_{\text{out}}| \rangle^2 = x_E^2 \left[2 \langle |k_{Ty}| \rangle^2 + \langle |j_{Ty}| \rangle^2 \right] + \langle |j_{Ty}| \rangle^2 \quad (3)$$

where

$$x_E = -\frac{\vec{p}_{Tt} \cdot \vec{p}_{Ta}}{p_{Tt}^2} = -\frac{p_{Ta} \cdot \cos \Delta\phi}{p_{Tt}} = \frac{z_a \cdot \hat{p}_{Ta}}{z_t \cdot \hat{p}_{Tt}} \quad (4)$$

represents the fragmentation variable of the away-side jet. We note however, that [5] explicitly neglected $\langle z_t \rangle = \langle p_{Tt} / \hat{p}_{Tt} \rangle$ in the formula at ISR energies, where $\langle z_t \rangle \simeq 0.85$, while it is not negligible at $\sqrt{s}=200$ GeV. Furthermore, as mentioned earlier, the average values of trigger and associated jet momenta are generally not the same. There is a systematic momentum unbalance which appears to be a consequence of the k_T -smearing of steeply falling parton momentum distribution. The event sample with a condition of $p_{Tt} > p_{Ta}$ is dominated by configurations where k_T -vector is parallel with trigger jet and antiparallel with associated jet and $\langle \hat{p}_{Tt} - \hat{p}_{Ta} \rangle \neq 0$. Let us introduce the hadronic and partonic variables x_h and \hat{x}_h

$$x_h \equiv \frac{p_{Ta}}{p_{Tt}} \quad \hat{x}_h = \hat{x}_h(\langle k_T^2 \rangle, x_h) \equiv \frac{\langle \hat{p}_{Ta} \rangle}{\langle \hat{p}_{Tt} \rangle} \quad (5)$$

The detailed discussion on the magnitude of this unbalance is given in sections 3 and 2. In order to derive the relation between the magnitude of p_{out} and k_T let us first consider the simple case where we have neglected both trigger and associated $\langle j_T \rangle$ (see panel (a) on Fig. 1). In this case one can see that

$$\langle |p_{\text{out}}| \rangle |_{j_{Tt}=j_{Ta}=0} \equiv \langle |p_{\text{out}}| \rangle_{00} = \sqrt{2} \langle |k_{Ty}| \rangle \frac{p_{Ta}}{\langle \hat{p}_{Ta} \rangle} = \sqrt{2} \langle |k_{Ty}| \rangle x_h \frac{p_{Tt}}{\langle \hat{p}_{Tt} \rangle} \frac{\langle \hat{p}_{Ta} \rangle}{\langle \hat{p}_{Ta} \rangle} = \sqrt{2} \langle |k_{Ty}| \rangle \langle z_t \rangle \frac{x_h}{\hat{x}_h}.$$

Rewriting the formula for p_{out} in terms of RMS we get

$$\sqrt{\langle p_{\text{out}}^2 \rangle_{00}} = \langle z_t \rangle \sqrt{\langle k_T^2 \rangle} \frac{x_h}{\hat{x}_h}.$$

However, the jet fragments are produced with finite jet transverse momentum j_T . The situation when the trigger particle is produced with $j_{Ty} > 0$ GeV/c and the associated particle with $j_{Ty}=0$ GeV/c is shown on the right panel of Fig. 1. The p_{out} vector picks an additional component

$$\langle p_{\text{out}}^2 \rangle |_{j_{Tt}>0, j_{Ta}=0} = \left[\langle p_{\text{out}}^2 \rangle_{00} + \frac{\langle j_{Tty}^2 \rangle}{p_{Tt}^2} (p_{Ta}^2 - \langle p_{\text{out}}^2 \rangle_{00}) \right] \frac{p_{Tt}^2 - \langle j_{Tty}^2 \rangle}{p_{Tt}^2}$$

With an assumption of $j_{Tty} \ll p_{Tt}$ we found that

$$\langle p_{\text{out}}^2 \rangle |_{j_{Tt}>0, j_{Ta}=0} = x_h^2 \left[\langle z_t \rangle^2 \langle k_T^2 \rangle \frac{1}{\hat{x}_h^2} + \langle j_{Tty}^2 \rangle \right]$$

In order to include also j_{Ta} we assumed collinearity of j_{Ta} and p_{out} and we simply write

$$\langle p_{\text{out}}^2 \rangle |_{j_{Tt}>0, j_{Ta}>0} = x_h^2 \left[\langle z_t \rangle^2 \langle k_T^2 \rangle \frac{1}{\hat{x}_h^2} + \langle j_{Tty}^2 \rangle \right] + \langle j_{Tay}^2 \rangle \quad (6)$$

and we solve it for $\langle z_t \rangle \sqrt{\langle k_T^2 \rangle} / \hat{x}_h$

$$\frac{\langle z_t \rangle \sqrt{\langle k_T^2 \rangle}}{\hat{x}_h} = \frac{1}{x_h} \sqrt{\langle p_{\text{out}}^2 \rangle - \langle j_{Tay}^2 \rangle - x_h^2 \langle j_{Tty}^2 \rangle}$$

and if we assume no difference between j_{Tt} and j_{Ta} then we have

$$\frac{\langle z_t(k_T, x_h) \rangle \sqrt{\langle k_T^2 \rangle}}{\hat{x}_h(k_T, x_h)} = \frac{1}{x_h} \sqrt{\langle p_{\text{out}}^2 \rangle - \langle j_{Ty}^2 \rangle (1 + x_h^2)} \pm \frac{1}{x_h} \sqrt{\frac{\langle p_{\text{out}}^2 \rangle \cdot \delta \langle p_{\text{out}}^2 \rangle + \langle j_{Ty}^2 \rangle \cdot \delta \langle j_{Ty}^2 \rangle (1 + x_h^2)^2}{\langle p_{\text{out}}^2 \rangle - \langle j_{Ty}^2 \rangle (1 + x_h^2)}} \quad (7)$$

All quantities on the right-hand side of Eq. (7) can be directly extracted from the correlation function. The correlation functions are measured in the variable $\Delta\phi$ in bins of p_{Tt} and p_{Ta} (*e.g.* see Fig. 4), and the rms of the near and away peaks σ_N and σ_A are extracted. We tabulated σ_N and σ_A for many combinations of p_{Tt} and p_{Ta} (see *e.g.* Fig. 7). In previous versions we have used the approximation $\sqrt{\langle p_{out}^2 \rangle} \sim p_{Ta} \sin \sigma_A$. However we have recently noticed that this approximation and other approximations for $\sqrt{\langle p_{out}^2 \rangle}$ proposed by Peter Levai and Jiangyong Jia (see appendix A.2) are inadequate for $\sigma_A > 0.4$ radians, so we no longer use σ_A to calculate k_T . We now extract $\sqrt{\langle p_{out}^2 \rangle}$ directly for all values of p_{Tt} p_{Ta} (even for wide bins in p_{Ta} using the $\langle p_{Ta} \rangle$ of the bin) by fitting the correlation function in the $\pi/2 < \Delta\phi < 3\pi/2$ region by Eq. (57) to extract $\sqrt{\langle p_{out}^2 \rangle}$ in the bin. We still use a Gaussian function in $\Delta\phi$ in the near angle peak to extract $\sqrt{\langle j_T^2 \rangle}$.

In order to extract $\langle z_t \rangle$ and \hat{x}_h the knowledge of the fragmentation function is needed and the detailed discussion is given in following sections.

1.2 Run-2/run-3 comparison

Let us first review the results from the $h^\pm - h^\pm$ analysis presented in [1] also shown in [3] (see Fig. 2 and compare it with the new results extracted from the run-3 $\pi^0 - h^\pm$ analysis done in the same fixed- p_T bins. This should serve as a consistency check between these two different analyzes on two different data sets (run-2 and run-3 pp data) and different correlations ($h^\pm - h^\pm$ and $\pi^0 - h^\pm$).

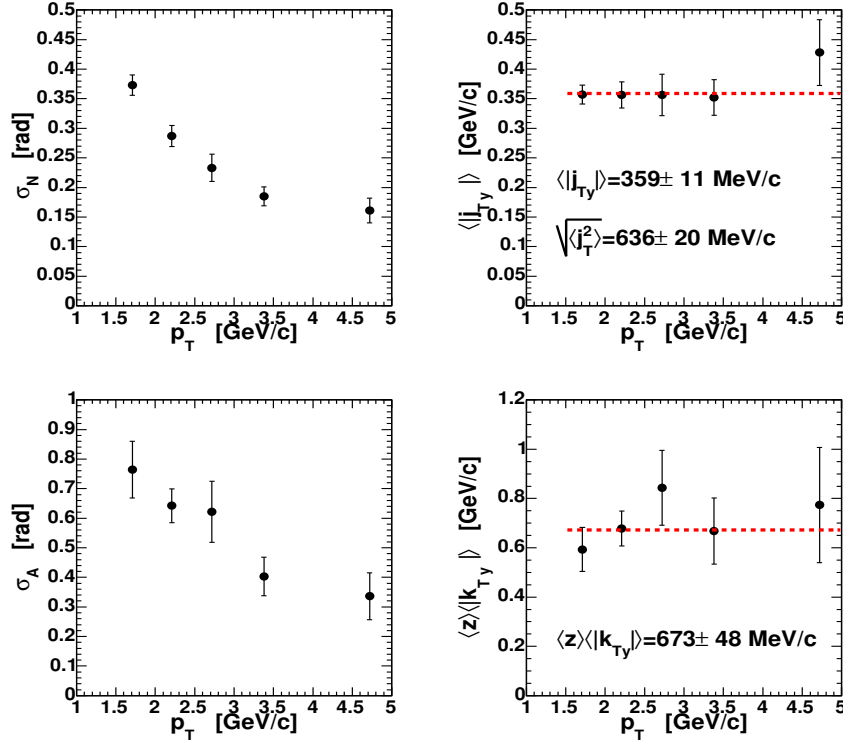


Figure 2: *Left:* Measured values of σ_N and σ_A for “fixed” $h^\pm - h^\pm$ correlation (no distinction between trigger and associated particle, events are selected with both particles in the same p_T -bin) in run-2 $p + p$ taken from [1]. *Right:* Extracted $\langle |j_{Ty}| \rangle$ and $\langle |k_{Ty}| \rangle$ for $h^\pm - h^\pm$ in run-2 pp using formulae (18) and (20) in [1].

From the run-2 $h^\pm - h^\pm$ correlation width the values of $\langle |j_{Ty}| \rangle = 359 \pm 11$ MeV/c and $\langle z \rangle \langle |k_{Ty}| \rangle = 673 \pm 48$ MeV/c were obtained (see [1] p.22). Dividing by $\langle z \rangle = 0.7$, which is the average value extracted from inclusive cross section analysis, we get the value $\langle |k_{Ty}| \rangle = 961 \pm 68$ MeV/c as in [3].

If we now repeat the same analysis with run-3 $\pi^0 - h^\pm$ correlations (see Fig. 3) we get following results: $\langle |j_{Ty}| \rangle = 305 \pm 4$ MeV/c and $\langle z \rangle \langle |k_{Ty}| \rangle = 643 \pm 22$ MeV/c (see Tab. 1). It is evident that the away-side width and $\langle |k_{Ty}| \rangle$ from both run-2 $h^\pm - h^\pm$ and run-3 $\pi^0 - h^\pm$ analyzes are in good agreement. However, the near-side peak width and extracted $\langle |j_{Ty}| \rangle$ are about 10% smaller in run-3 $\pi^0 - h^\pm$ analysis. It may be interesting to repeat the

Table 1: Comparison of the run-2 results presented at QM04 [3] with the values extracted from run-3 $\pi^0 - h^\pm$ correlation function.

	$\langle j_{Ty} \rangle$	$\langle z_t \rangle \langle k_{Ty} \rangle$
run-2 $h^\pm - h^\pm$	$359 \pm 11 \text{ MeV}/c$	$673 \pm 48 \text{ MeV}/c$
run-3 $\pi^0 - h^\pm$	$305 \pm 4 \text{ MeV}/c$	$643 \pm 22 \text{ MeV}/c$

$h^\pm - h^\pm$ analysis with run-3 data. This is however not the subject of this note and we will just conclude that the new $\pi^0 - h^\pm$ run-3 analysis is consistent with what we have seen in run-2.

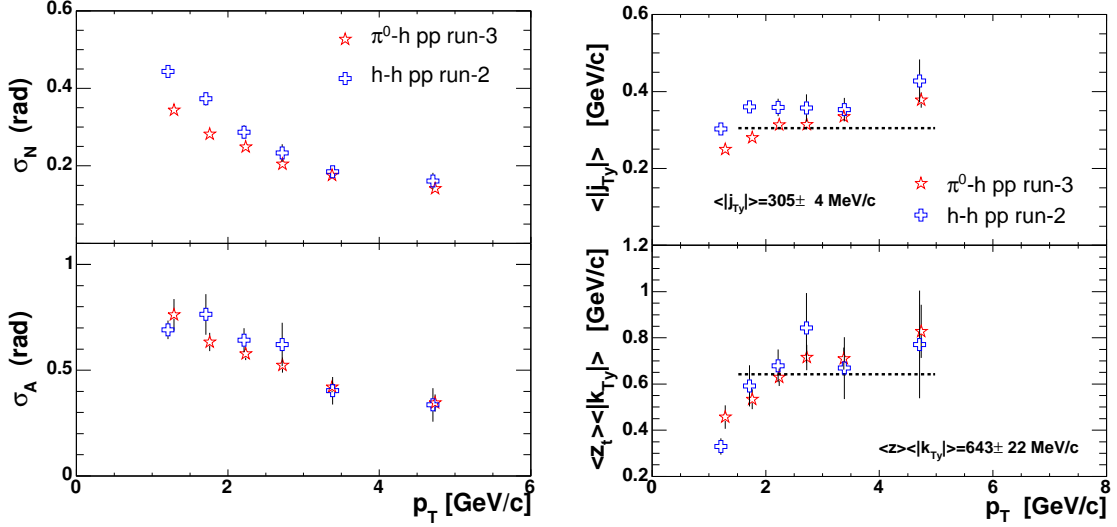


Figure 3: *Left*: Measured values of σ_N and σ_A for “fixed” $h^\pm - h^\pm$ correlation (no distinction between trigger and associated particle, events are selected with both particles in the same p_T -bin) in run-2 pp taken from [1] (the same as on Fig. 2) and new values obtained from $\pi^0 - h^\pm$ run-3 pp correlations. *Right*: Extracted $\langle |j_{Ty}| \rangle$ and $\langle z_t \rangle \langle |k_{Ty}| \rangle$ for $\pi^0 - h^\pm$ in run-3 pp using formulae from [1]. The dashed lines correspond to the 0th order polynomial fit.

1.3 Assorted correlations

Fixed- p_T correlation technique ($p_{Tt}=p_{Ta}$) explores only the diagonal terms in back-to-back jets fragmentation space. On the other hand, the assorted correlation ($p_{Tt} \neq p_{Ta}$) allows mapping of the full fragmentation space.

Identified π^0 tracks are used as a trigger particle (see Sec. A.6) and charged particle track as an associated particle. The details on the quality cuts on charged track are discussed in great details in [1]. Let us remind the requirements for tracks used in this analysis:

- 3σ matching cut between DC and PC3 and PC2 in WA.
- 2σ matching cut between DC and EMC.
- $|z_{DC}| < 75 \text{ cm}$

Whenever the π^0 was found in the event the real, $dN_{\text{uncorr}}/d\Delta\phi$, and mixed, $dN_{\text{mix}}/d\Delta\phi$ distribution for given p_{Tt} (π^0) and p_{Ta} (charged hadron) was cumulated (see left panel of Fig. 4). In order to extract the widths and yields we fitted the raw $dN_{\text{uncorr}}/d\Delta\phi$ distribution with the product of

$$\frac{dN_{\text{uncorr}}}{d\Delta\phi} = \frac{1}{\mathcal{N}} \frac{dN_{\text{mix}}}{d\Delta\phi} \cdot (a_0 + C_1 \cdot \text{Gauss}(0) + C_2 \cdot \left. \frac{dN_{\text{away}}}{d\Delta\phi} \right|_{\pi/2}) \quad (8)$$

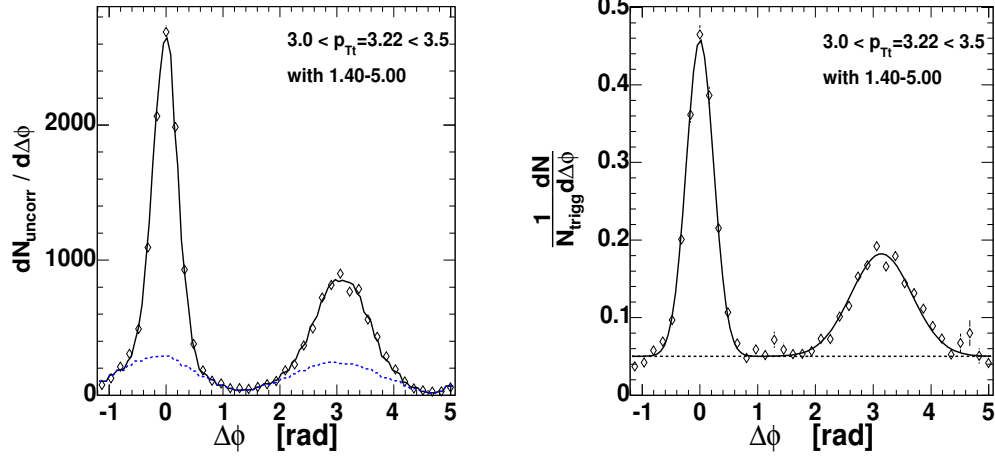


Figure 4: An example of the correlation functions for $3 < p_{Tt} < 3.5$ GeV/ c and associated particles in $1.4 < p_{Ta} < 5$ GeV/ c . Unnormalized pair-yield distribution (left panel) plotted with the fit function Eq. (8) modulated by pair detection efficiency derived from the mixed distribution (blue dashed line). Per π^0 trigger yield distribution corrected for the pair detection efficiency (right panel). Dashed line represents the constant term in the fit.

where the mixed event distribution is normalized to 2π ($\mathcal{N} = \sum dN_{\text{mix}}^i/d\Delta\phi$), $dN_{\text{away}}/d\Delta\phi|_{\pi/2}^{3\pi/2}$ is the away-side $\Delta\phi$ distribution according Eq. (57) and a_0 , C_1 , C_2 , σ_N and $\langle p_{\text{out}}^2 \rangle$ are parameters to be determined from the fit. Then the normalized correlation function was constructed as ratio of real and mixed distributions multiplied by η -acceptance correction factor $R_{\Delta\eta}$, divided by p_T -dependent efficiency correction $\epsilon(p_T)$ (see left panel of Fig. 5) and divided by number of π^0 triggers.

$$\frac{1}{N_{\text{trigg}}} \frac{dN}{d\Delta\phi} = \frac{R_{\Delta\eta}}{N_{\text{trigg}} \epsilon(p_T)} \frac{dN_{\text{uncorr}}(\Delta\phi)/d\Delta\phi}{dN_{\text{mix}}(\Delta\phi)/d\Delta\phi} \cdot \mathcal{N} \quad (9)$$

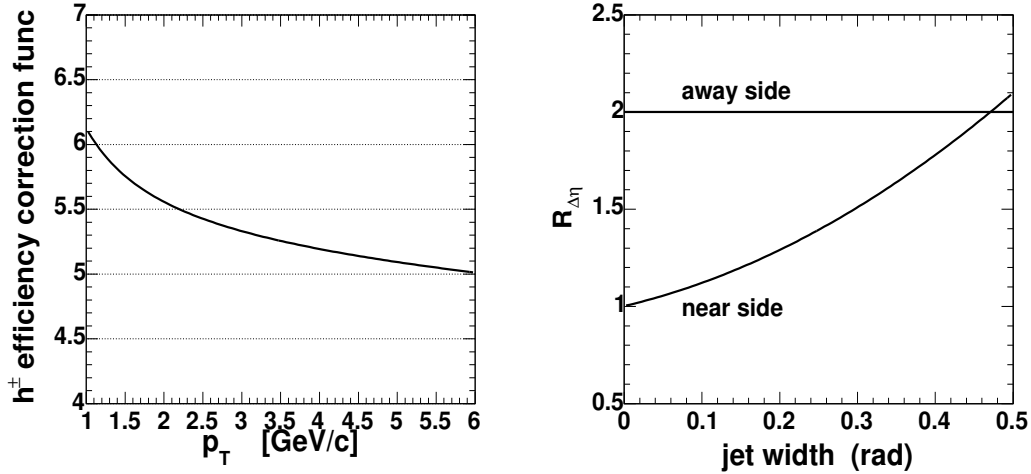


Figure 5: *Left*: Inclusive charged hadron efficiency correction function taken from Jiangyong AN. *Right*: η acceptance correction factor for loss of jet pairs outside limited η -acceptance of the PHENIX experiment.

The $R_{\Delta\eta}$ correction factor which accounts for limited η acceptance of the PHENIX experiment (see right panel of Fig. 5) for the the near-side yield, with an assumption that the angular jet width is the same in $\Delta\eta$ and in $\Delta\phi$,

can be written as

$$R_{\Delta\eta} = \frac{1}{\frac{1}{\sqrt{2\pi\sigma_N^2}} \int_{-0.7}^{0.7} \exp\left(-\frac{\Delta\eta}{2\sigma_N^2}\right) acc(\Delta\eta) d\eta} \quad (10)$$

where $acc(\Delta\eta)$ represent the PHENIX pair acceptance function in $|\Delta\eta|$. It can be obtained by convolving two flat distributions in $|\Delta\eta| < 0.35$, so $acc(\Delta\eta)$ has a simple triangular shape: $acc(\Delta\eta) = (0.7 - |\Delta\eta|)/0.7$. For the away-side yield the corresponding $R_{\Delta\eta}$ is

$$R_{\Delta\eta} = \frac{2 \times 0.7}{\frac{1}{\sqrt{2\pi\sigma_N^2}} \int_{-0.7}^{0.7} acc(\Delta\eta) d\eta} = 2 \quad (11)$$

$R_{\Delta\eta}$ equal 2, because the pair efficiency has a triangular shape in $|\Delta\eta| < 0.7$, which results in 50% average efficiency when the real jet pair distribution is flat in $|\Delta\eta| < 0.7$.

Normalized correlation functions for various p_{Tt} and p_{Ta} are shown on Fig. 6.

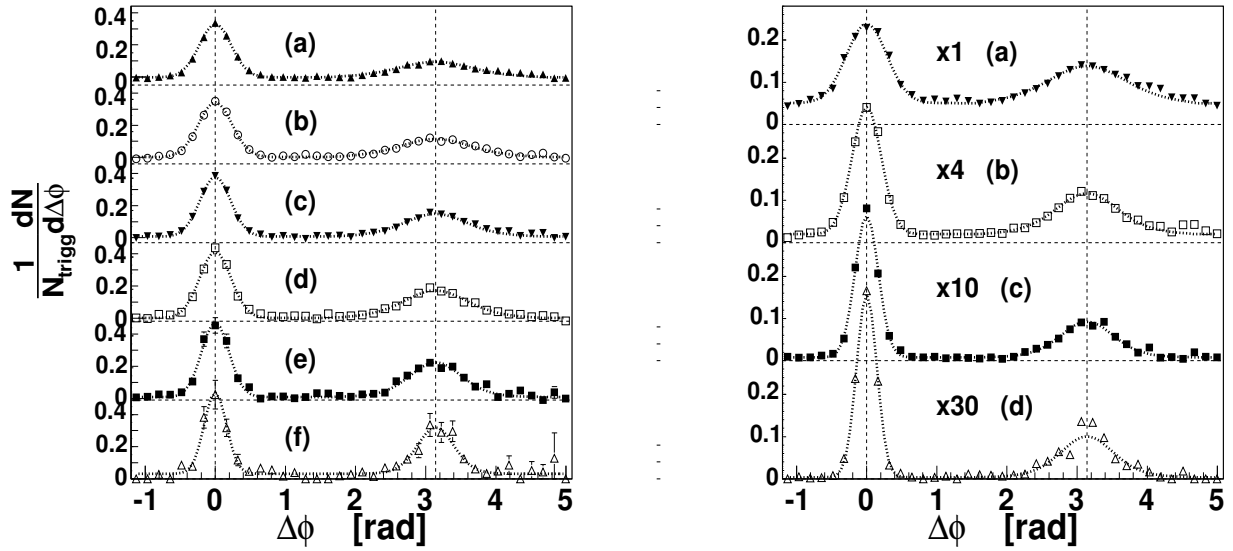


Figure 6: *Left:* Measured yield of charged hadrons associated with trigger π^0 of various transverse momenta as indicated in the table. *Right:* Measured yield of charged hadrons associated with trigger π^0 of fixed transverse momenta and various associated momenta. The dashed lines corresponds to the fit of Eq. (8).

	$1.4 < p_{Ta} < 5.0 \text{ GeV}/c$	$3.0 < p_{Tt} < 10.0 \text{ GeV}/c$
(a)	$2.5 < p_{Tt} < 3.0 \text{ GeV}/c$	(a) $1.7 < p_{Ta} < 2.0 \text{ GeV}/c$
(b)	$3.0 < p_{Tt} < 3.5 \text{ GeV}/c$	(b) $2.0 < p_{Ta} < 2.5 \text{ GeV}/c$
(c)	$3.5 < p_{Tt} < 4.5 \text{ GeV}/c$	(c) $2.5 < p_{Ta} < 3.0 \text{ GeV}/c$
(d)	$4.5 < p_{Tt} < 5.5 \text{ GeV}/c$	(d) $3.0 < p_{Ta} < 3.5 \text{ GeV}/c$
(e)	$5.5 < p_{Tt} < 6.5 \text{ GeV}/c$	
(f)	$6.5 < p_{Tt} < 8.0 \text{ GeV}/c$	

Extracted widths of the near and away-side correlation peaks as a function of p_{T_a} and p_{T_t} are shown on Fig. 7. Both p_{T_a} and p_{T_t} distributions of the near and away-side peak show the decreasing trend according an expectation based on formulae discussed in section 1.2. Whereas the magnitude of σ_N , according to Eq. (1), should vanish for large values of p_{T_t} and p_{T_a} , the σ_A magnitude, according to Eq. (7), should not vanish even for large values of p_{T_a} and its value saturates at around $\hat{x}_h^{-1} \langle z_t \rangle \sqrt{\langle k_T^2 \rangle} / p_{T_t}$.

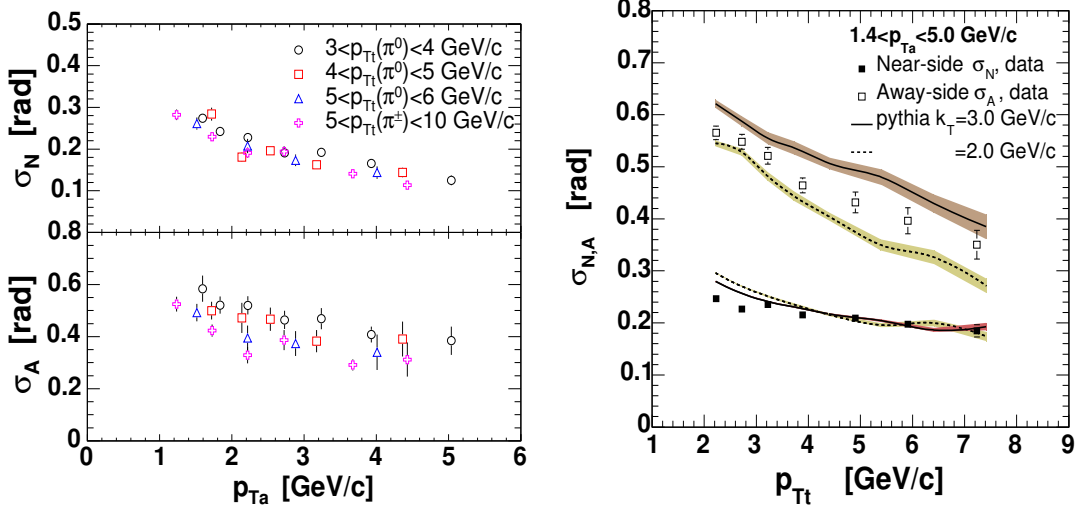


Figure 7: *Left*: Extracted values of σ_N and σ_A for $\pi^0 - h^\pm$ in run-3 pp data for various trigger π^0 p_{T_t} , as indicated in the legend, as a function of p_{T_a} . *Right*: Extracted values of σ_N and σ_A for $\pi^0 - h^\pm$ in run-3 pp data for fixed associated bin $1.4 < p_{T_a} < 5.0$ as a function of trigger p_{T_t} . The brown and yellow bands represents the PYTHIA simulation (for details see section 2) with $\sqrt{\langle k_T^2 \rangle} = 2$ and 3 GeV/c.

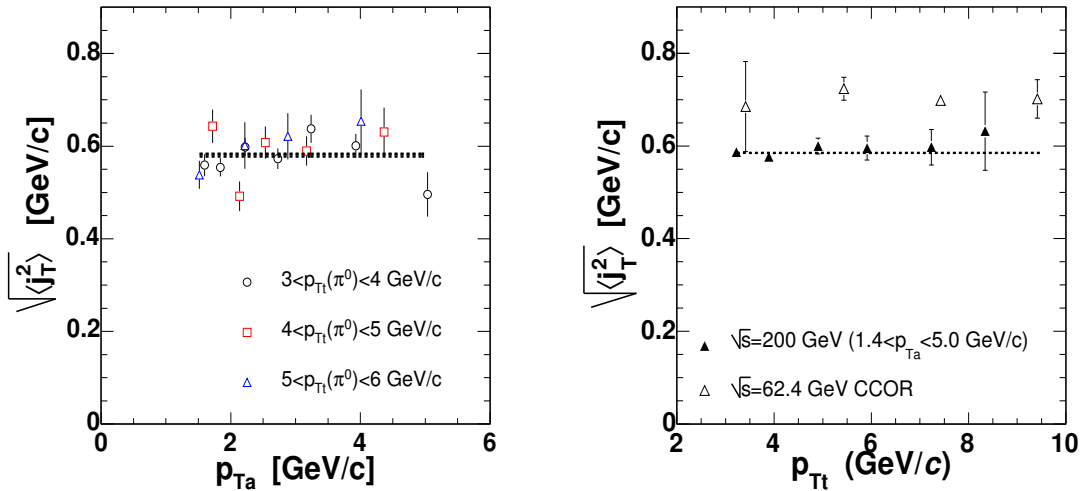


Figure 8: *Left*: RMS of j_T for various p_{T_t} as a function of p_{T_a} . *Right*: RMS of j_T for the fixed associated bin $1.4 < p_{T_a} < 5.0$ GeV/c as a function of p_{T_t} . The dashed line corresponds to the 0^{th} order polynomial fit.

There is clearly no variation of $\sqrt{\langle j_T^2 \rangle}$ with p_{T_a} nor on p_{T_t} . It is expected that $\sqrt{\langle j_T^2 \rangle}$ can not remain constant for arbitrarily small values of p_{T_a} because of the phase space limitation. In the region where $p_{T_a} \leq \sqrt{\langle j_T^2 \rangle}$, the magnitude of the j_T -vector is truncated, similar to the “Seagull effect”. [7]. Since the $\langle j_T^2 \rangle$ values are on the order

of 600 MeV/c, we assume that the phase space limitation can be safely neglected for $p_{T_a} > 1.5$ GeV/c and we extract the values of $\sqrt{\langle j_T^2 \rangle}$ averaged over p_{T_a} and p_{T_t} (see Fig. 8)

$$\sqrt{\langle j_T^2 \rangle} = 0.585 \pm 0.006 \text{ GeV/c} \quad \text{or} \quad \langle |j_{Ty}| \rangle = 0.330 \pm 0.003 \text{ GeV/c} \quad (12)$$

The independence of $\sqrt{\langle j_T^2 \rangle}$ on either p_{T_t} or \sqrt{s} has been observed by the CCOR experiment in the range $\sqrt{s}=31\text{--}62.4$ GeV [4]. The $\sqrt{\langle j_T^2 \rangle}$ values at $\sqrt{s}=62.4$ GeV (open triangles on right panel of Fig. 8) are systematically larger than values found in this analysis. The discrepancy should not be taken as significant, as CCOR used a slightly different technique than in this paper. CCOR extracted the $\sqrt{\langle j_T^2 \rangle}$ values from measurements of $\langle |p_{\text{out}}| \rangle$ for different values of the x_E variable Eq. (4). According to Eq. (3) the $\langle |p_{\text{out}}| \rangle^2$ magnitude should depend linearly on x_E^2 ; and the $\langle |j_{Ty}| \rangle$ value was extracted from the intercept of the $\langle |p_{\text{out}}| \rangle^2(x_E)$ fit at $x_E=0$, rather than from a measurement of σ_N .

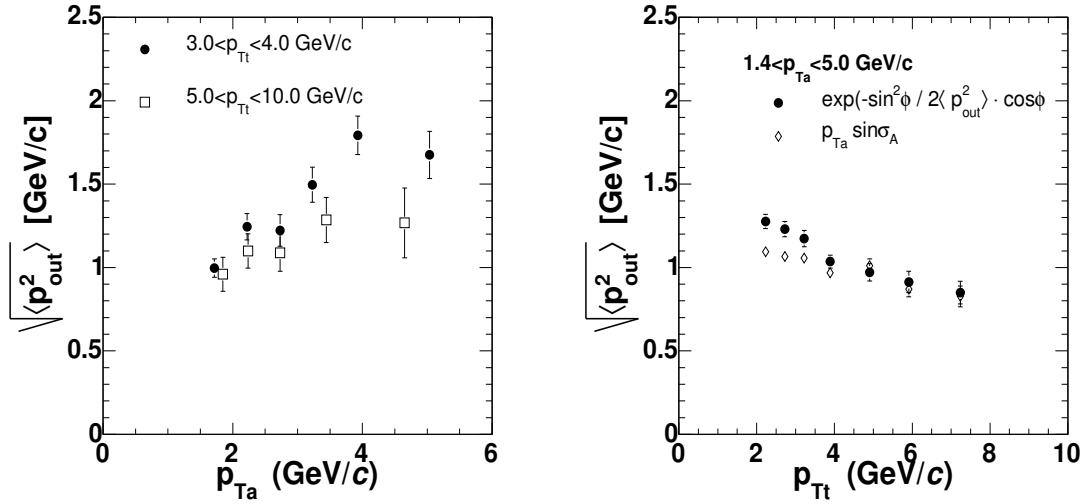


Figure 9: *Left*: Extracted values of $\sqrt{\langle p_{\text{out}}^2 \rangle}$ for $3.0 < p_{T_t} < 4.0$ and $5.0 < p_{T_t} < 10.0$ GeV/c for various values of p_{T_a} using the direct p_{out} extraction method based on fitting the away-side peak by Eq. (57). *Right*: Extracted values of $\sqrt{\langle p_{\text{out}}^2 \rangle}$ for $1.4 < p_{T_a} < 5.0$ GeV/c for various values of p_{T_t} from Eq. (57) (solid circles). For a comparison the indirect $p_{\text{out}} = p_{T_a} \sin(\sigma_A)$ values are also shown (open diamonds).

The $\sqrt{\langle p_{\text{out}}^2 \rangle}$ values directly extracted from the fit of Eq. (57) into a correlation function are shown on Fig. 9. The $p_{\text{out}} = p_{T_a} \sin(\sigma_A)$ approximation (open diamonds) is shown as well (right panel of Fig. 9). It is evident that this approximation is not quite acceptable for p_{T_t} below 4 GeV/c where σ_A is larger than 0.4 rad. The relative error may be as large as 20% (see also Fig. 34).

The $\hat{x}_h^{-1} \langle z_t \rangle \sqrt{\langle k_T^2 \rangle}$ values calculated according to Eq. (7) are shown on Fig. 10. The small systematic error is mainly due to the assumption of collinearity between p_{out} and j_T . The p_{T_a} and p_{T_t} dependences of extracted $\hat{x}_h^{-1} \langle z_t \rangle \sqrt{\langle k_T^2 \rangle}$ reveals a striking trend (opposite to p_{out} on Fig. 9). It was expected, that by fixing the value of p_{T_t} , the kinematics of the hard scattering is fixed independently of the value of p_{T_a} . Various values of p_{T_a} sample just various region of the fragmentation function and the value of $\hat{x}_h^{-1} \langle z_t \rangle \sqrt{\langle k_T^2 \rangle}$ was expected to be constant. For the same reason, we also expected the magnitude of σ_A varies less with p_{T_a} because it is proportional to the quadratic sum of large and constant k_T -component and relatively small j_T -component. It is evident that neither of these assumptions are true.

Exploring more the hard scattering kinematics, we have realized that the reason for the variation of $\hat{x}_h^{-1} \langle z_t \rangle \sqrt{\langle k_T^2 \rangle}$ with p_{T_a} is caused by a strong variation of $\langle z_t \rangle$ which was not expected from the analysis of the inclusive $d\sigma/p_T dp_T$ distribution (see section 3. in [1]). By changing the value of p_{T_a} even though the p_{T_t} is fixed, the partons' momenta on both sides are changed as well as the $\langle z_t \rangle$ and $\langle z_a \rangle$. This is also confirmed by the PYTHIA simulation (see left panel of Fig. 11) which was done for $\sqrt{\langle k_T^2 \rangle}=3$ GeV/c and the initial/final state QCD radiation (MSPT(61) and MSTP(71)) turned off. More details on PYTHIA simulation are given in section 2. Let us point out here that for the fixed- p_T correlation the results are less sensitive to the bias discussed previously. By simultaneous increase

of both p_{Tt} and p_{Ta} the average Q^2 increases and it leads to the compensation which keeps both $\langle z_t \rangle$ and $\langle z_a \rangle$ approximately constant.

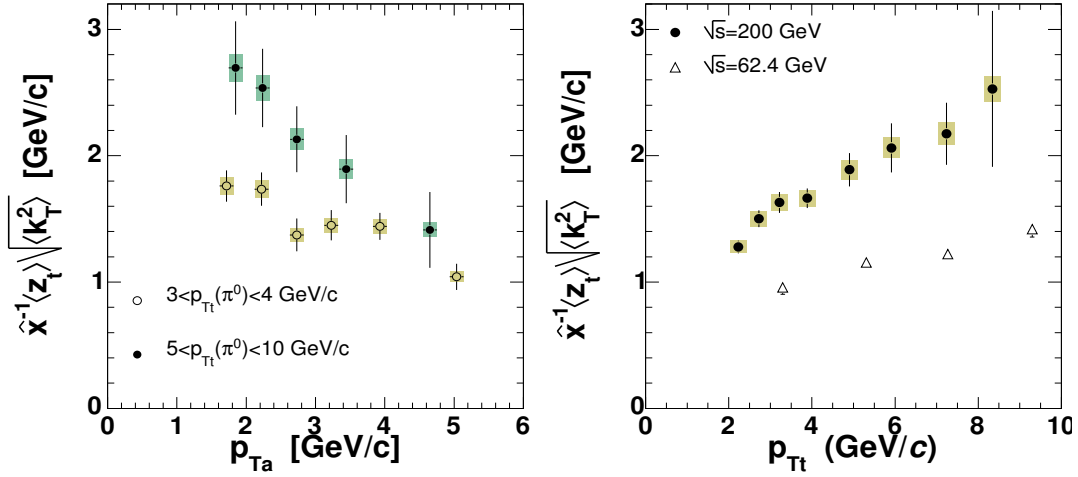


Figure 10: *Left:* $\hat{x}_h^{-1} \langle z_t \rangle \sqrt{\langle k_T^2 \rangle}$ values calculated according to Eq. (7) for trigger π^0 in $3 < p_{Tt} < 4$ GeV/c and $5 < p_{Tt} < 6$ GeV/c as a function of p_{Ta} . *Right:* The same calculation according Eq. (7) for fixed associated bin $1.4 < p_{Ta} < 5.0$ GeV/c as a function of p_{Tt} . The systematic errors indicated by colored rectangles. The results obtained by CCOR collaboration at $\sqrt{s}=62.4$ GeV [4] displayed by empty triangles.

Conditional yield as a function of p_{Tt} is shown on right panel of Fig. 11.

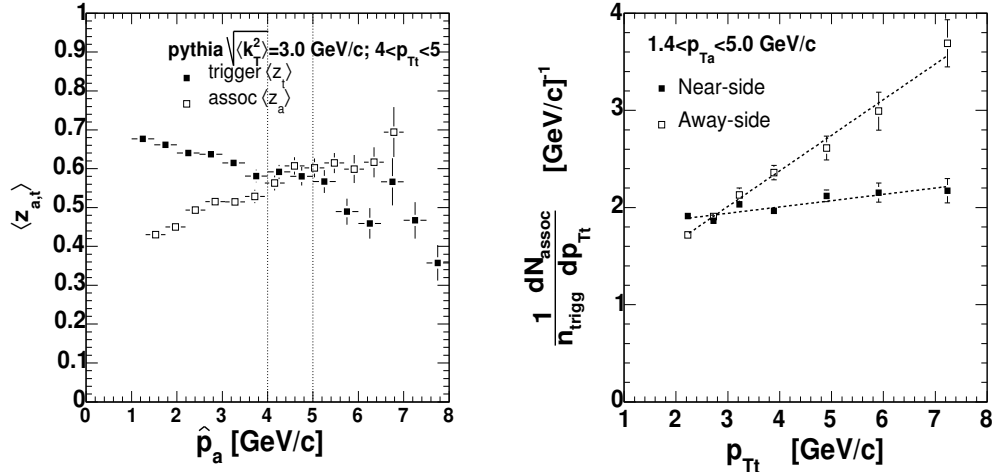


Figure 11: *Left:* The average values $\langle z_t \rangle$ and $\langle z_a \rangle$ as a function of associated particle momentum p_{Ta} from the PYTHIA simulation with $4 < p_{Tt} < 5$ GeV/c, $\sqrt{\langle k_T^2 \rangle}=3$ GeV/c and no initial and final state QCD radiation (MSPT(61) and MSTP(71)). The dashed lines indicates the symmetric region where $\langle p_{Tt} \rangle = \langle p_{Ta} \rangle$ and where, obviously, the $\langle z_t \rangle = \langle z_a \rangle$. *Right:* Conditional yield measured for fixed associated momentum $1.4 < p_{Ta} < 5.0$ GeV/c as a function of p_{Tt} in the near-angle peak (solid squares) and in the far-angle peak (open squares). The two dashed lines represent the 1st-order polynomial fit.

There is a distinct behavior of the near-side yield which varies with trigger p_{Tt} much less than the away-side yield (see Fig. 11). It reflects the fact that the particle detected in the fixed associated bin are produced from the lower z region of the fragmentation function for events with higher trigger p_{Tt} . This multiplicity increase is reduced

on the near-side jet due to the fact that with increasing p_{T_t} the near-side jet multiplicity increases, however, at the same time the larger fraction of this multiplicity is taken away by more energetic trigger particle.

As it was mentioned in section 1.1 the knowledge of the fragmentation function is necessary for extraction of $\langle k_T \rangle$ from the angular width of the away-side peak according formula Eq. (7). The fragmentation function should provide us with $\langle z_t \rangle$ value and it is also needed for the evaluation of the momentum unbalance characterized by \hat{x}_h . The extraction of the fragmentation function from the associated x_E -distributions is a subject of next section.

2 What do we learn from pythia?

In order to test the analysis scheme we used PYTHIA 6.319 event generator. The same cuts and selection as in the real data analysis and also identical software for constructing the correlation functions and extraction of $\langle z \rangle$, j_T and k_T was used. The typical parameter setting was as follow:

```
PDFtyp      1      D=1, MSTP(51)
PDFlib      7      D=7, MSTP(52)
msel        1      D=1, MSEL()
ckin3       3.0    D=0, CKIN(3); this has been studied in details, see below
procMode    3      D=1, MSTP(82)
```

```
KTmode      1      D=1, MSTP(91)
meanKT      3.0    D=1.0 PARP(91)
KTupperCut  10.0   D=5.0 PARP(93)
meanJTY     0.45   D=0.36 PARJ(21)
virtuality  4.0    D=1 PARP(67)
```

```
doFrag      2      D=1 MSTJ(1)
doFragGlue  1      D=3 MSTJ(2)
fragMomConv  1      D=0 MSTJ(3)
iniStateShow 0      D=1 MSTP(61)
finStateShow 0      D=1 MSTP(71)
```

The π^0 particles were selected as a trigger particles within PHENIX acceptance $-0.35 < \eta < 0.35$. The correlation function were reconstructed for full azimuthal acceptance so we did not produced mixed event distributions. The invariant π^0 cross section from pythia is shown on Fig. 12.

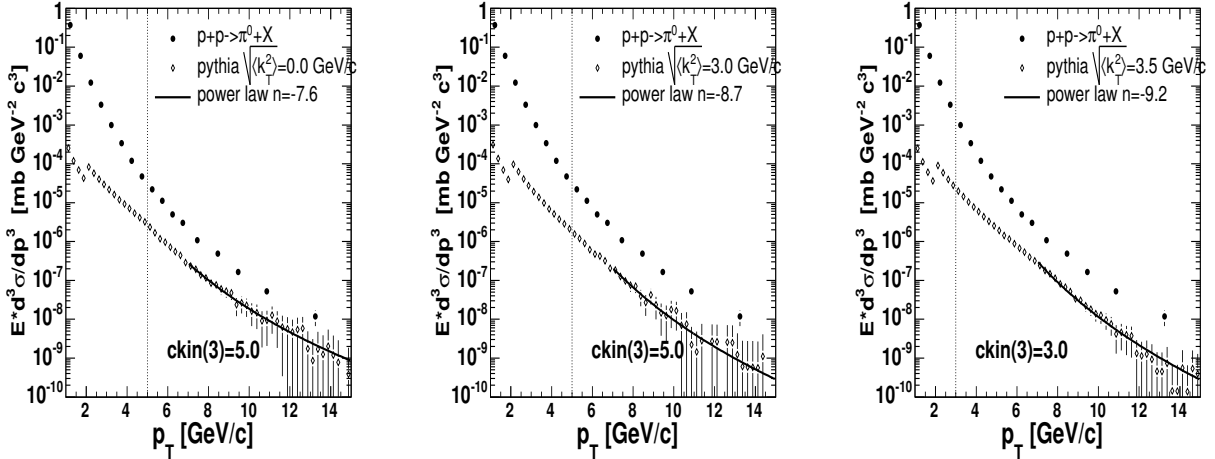


Figure 12: Pythia simulated π^0 invariant cross section for CKIN(3)=5 GeV/c & $\sqrt{\langle k_T^2 \rangle}=0$ GeV/c (left panel), CKIN(3)=5 GeV/c & $\sqrt{\langle k_T^2 \rangle}=3$ GeV/c (middle panel) and CKIN(3)=3 GeV/c & $\sqrt{\langle k_T^2 \rangle}=3.5$ GeV/c (right panel) compared to the data. Only events with at least one π^0 of $p_T > 2$ GeV/c were analyzed and this causes the kink at 2 GeV/c. The minimum hard-scattering transverse momentum, given by the value of CKIN(3) parameter, makes small kink at 3 or 5 GeV/c. The influence of CKIN(3) value will be discussed in details.

The exponent of the power law fit to the pythia-simulated distributions is somewhat smaller than what we see in the data. More importantly, it does not increase dramatically with k_T as demonstrated from in the previous section. When we increase the $\sqrt{\langle k_T^2 \rangle}$ from 0 to 3 GeV/c the power n increased only from 7.6 to 8.7. The spectrum is, however, smeared by the fragmentation process and the effect of the k_T -smearing may be partially washed out.

The k_T -smearing should be more pronounced on the parton distributions before fragmentation Fig. 13. But even in this case, the power n increases from 7.4 to 8.1 for $\sqrt{\langle k_T^2 \rangle}$ increasing from 0 to 3 GeV/c ($\sqrt{\langle k_{Tx}^2 \rangle}$ from

0 to 2.1 GeV/c). One would expect that the power changes at least by 2. In order to fully understand this one would need to explore the simulations with small or zero value of CKIN(3) parameter, but this requires much more statistics.

Table 2: Magnitudes of $\langle |\hat{p}_{\text{out}}| \rangle$ (see Eq. (13)) and $\sqrt{\langle (\hat{p}_{Tt} - \hat{p}_{Ta})^2 \rangle}$ from pythia simulations. All values are given in GeV/c. The $\langle |\hat{p}_{\text{out}}| \rangle \cdot \sqrt{2\pi}$ value should be equal to the input value of $\sqrt{\langle k_T^2 \rangle}$. Shower yes/no indicates whether the initial and final state showering (MSTP(61) and MSTP(71)) was on or off.

	$\sqrt{\langle k_T^2 \rangle}=0$ shower = yes	$\sqrt{\langle k_T^2 \rangle}=2.5$ shower = no	$\sqrt{\langle k_T^2 \rangle}=3.0$ shower = no	$\sqrt{\langle k_T^2 \rangle}=3.0$ shower = yes
$\langle \hat{p}_{\text{out}} \rangle$	0.98	2.02	2.43	2.19
$\langle \hat{p}_{\text{out}} \rangle \cdot \sqrt{2\pi}$	-	2.53	3.05	2.74
$\sqrt{\langle (\hat{p}_{Tt} - \hat{p}_{Ta})^2 \rangle}$	1.4	2.50	3.00	2.78

Since in the simulation the parton kinematics is accessible, we have calculated the magnitude of \hat{p}_{out} vector which is defined in the same way as the p_{out} for parton's fragments

$$\hat{p}_{\text{out}} = -\frac{\vec{\hat{p}}_{Tt} \times \vec{\hat{p}}_{Ta}}{\hat{p}_{Tt}}. \quad (13)$$

The magnitude of \hat{p}_{out} should be equal to the $\sqrt{2}\sqrt{\langle k_T^2 \rangle} = \sqrt{2\pi}\langle |k_T| \rangle$. The results for various k_T values are summarized in Tab. 2. It indicates that the \hat{p}_{out} , a measure of diparton acoplanarity, reflects to very good approximation the k_T value.

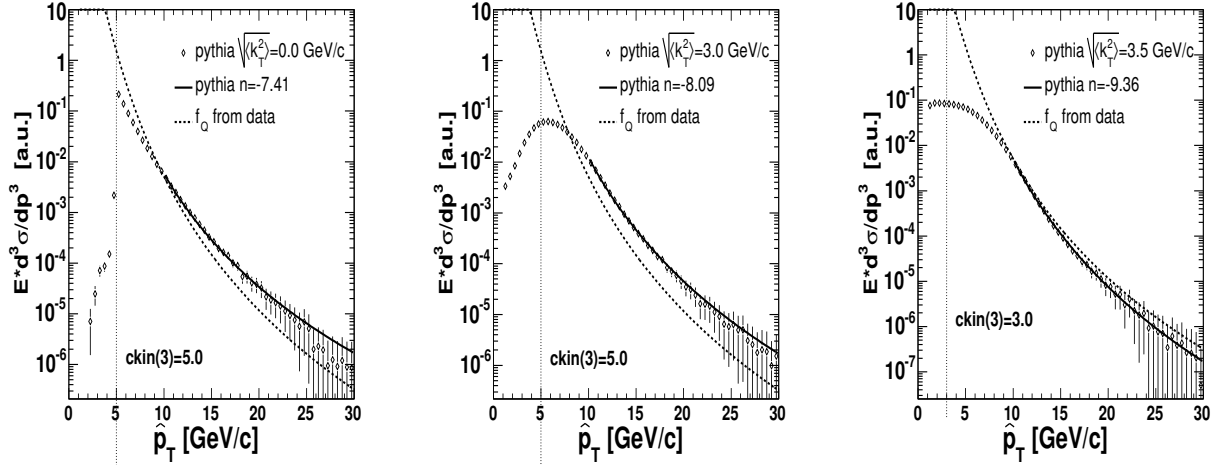


Figure 13: Pythia simulated final state parton distribution for CKIN(3)=5 GeV/c & $\sqrt{\langle k_T^2 \rangle}=0$ GeV/c (left panel), CKIN(3)=5 GeV/c & $\sqrt{\langle k_T^2 \rangle}=3$ GeV/c (middle panel) and CKIN(3)=3 GeV/c & $\sqrt{\langle k_T^2 \rangle}=3.5$ GeV/c (right panel). The dashed line on right panel represents the final state parton distribution derived from data.

2.1 Conditional distributions

In order to verify the influence of lower hard scattering p_T -cut CKIN(3), the large statistics sample with CKIN(3)=2 GeV/c and $\sqrt{\langle k_T^2 \rangle}=2.5$ and 3.0 GeV/c was generated, trigger π^0 were selected and correlated with an associated h^\pm . The invariant π^0 distribution is shown again on Fig. 14. The absolute normalization of pythia cross section

is not quite clear. If the final cross section from pythia is used to scale the resulting distribution the cross section undershoots the data by factor of 10. However, this is not important for this analysis so we ignore it.

Conditional parton distributions are shown on the right panel of Fig. 14. There is rather good agreement between the $f_Q(\hat{p}_T)$ derived from data and the inclusive distribution (open diamonds). There is obviously strong dependence on the input value of $\langle k_T^2 \rangle$ and, as it was mentioned earlier, the best agreement can be reached if $\sqrt{\langle k_T^2 \rangle}$ lies in 3-3.5 GeV/c range. The parton distribution with a single ($4 < p_{Tt} < 5$ GeV/c) and double condition ($4 < p_{Tt} < 5$ & $2 < p_{Ta} < 3$ GeV/c) as a function of p_{Tt} and as a function of \hat{p}_T are also shown.

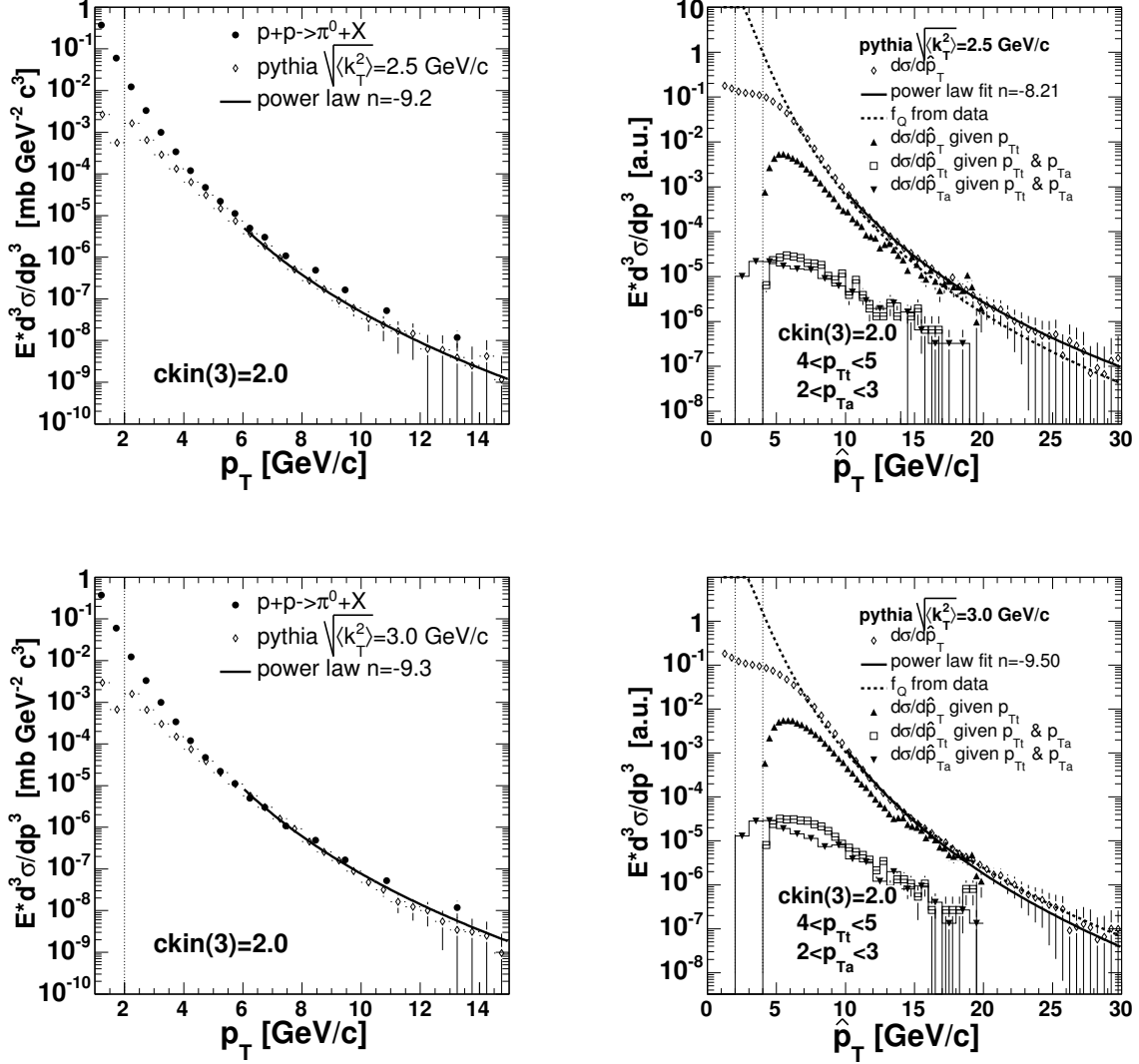


Figure 14: *Left:* Pythia simulated π^0 invariant cross section for $\sqrt{\langle k_T^2 \rangle} = 2.5$ and 3.0 GeV/c. CKIN(3)=2 GeV/c was used. *Right:* Inclusive parton distribution (open diamonds). The parton distribution with a single condition of $4 < p_{Tt} < 5$ GeV/c (filled triangles) and with double condition $4 < p_{Tt} < 5$ & $2 < p_{Ta} < 3$ GeV/c as a function of p_{Tt} (open squares) and as a function of \hat{p}_T (filled triangles).

One important feature can be learned from the shape of the conditional parton distribution near $z \rightarrow 1$ which corresponds to $\hat{p}_{Tt} \rightarrow p_{Tt}$. The distribution turns rather smoothly down. This indicates that the pythia fragmentation function has a strong suppression factor at the end of the phase space where $\hat{p}_T \rightarrow \sqrt{s}/2$. This suppression factor was studied also here but not used for the final analysis.

2.2 k_T -unbalance

One of the issues raised by Yasuyuki in his comments to ppg029/039 release concerns the momentum unbalance between the b2b partons. Fig. 15, where the average difference between the trigger and associated partons' momenta is plotted with p_{Tt} , indicates that this is a valid concern. The difference grows proportionally to the difference $\langle p_{Tt} \rangle - \langle p_{Ta} \rangle$ and saturates around $\sqrt{\langle k_T^2 \rangle}$. The last statements is proven in section 4.3.

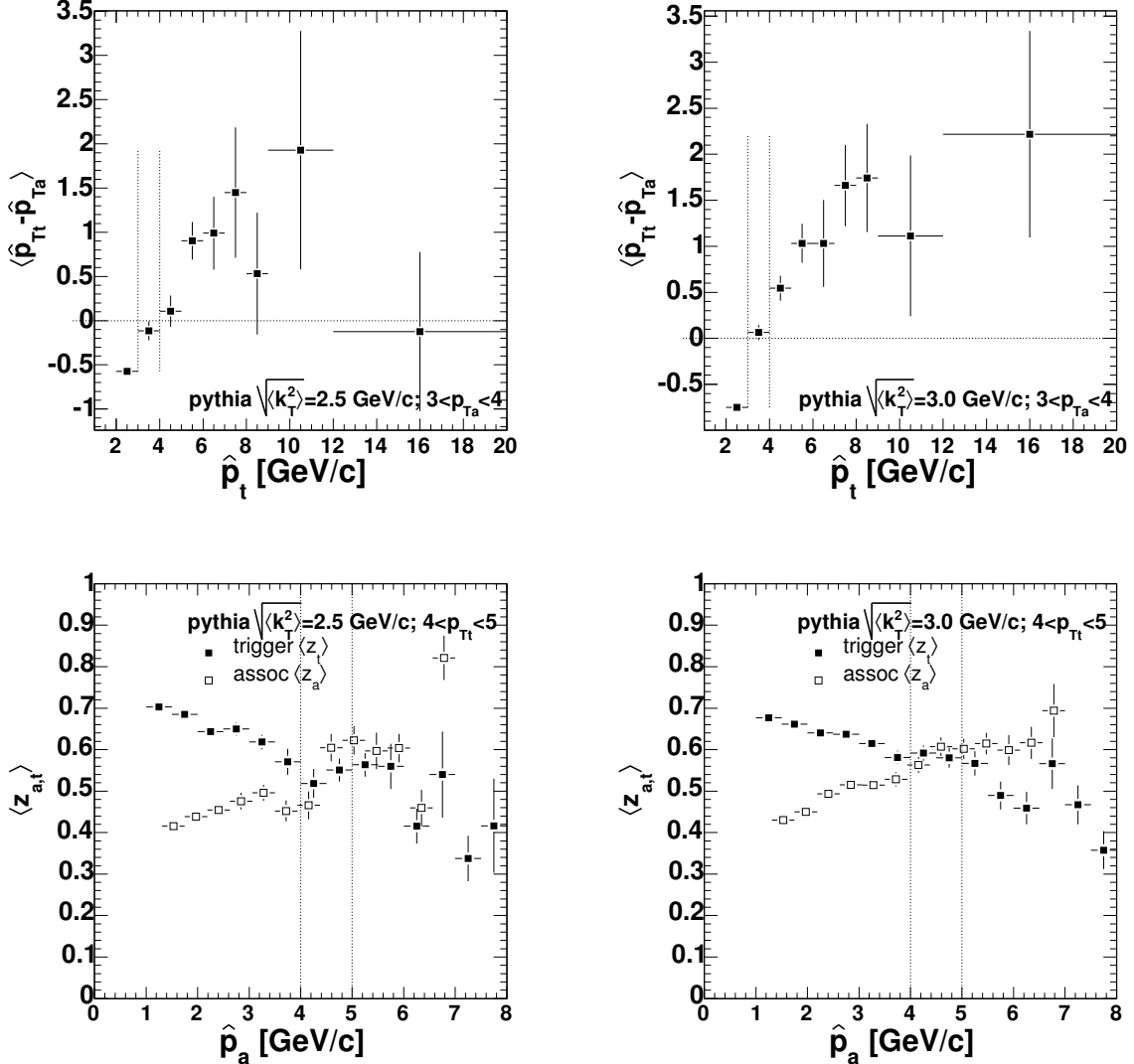


Figure 15: *Upper:* Pythia simulated mean difference between quark momenta on trigger and away side when detecting a trigger particle p_{Tt} an associated particle in $3 < p_{Ta} < 4$ GeV/c range. Again, calculation was done for two values of $\sqrt{\langle k_T^2 \rangle} = 2.5$ (left) and 3.0 GeV/c (right) and CKIN(3)=2 GeV/c. *Lower:* The average z of trigger and associated particle as a function of p_{Ta} when momentum of the trigger particle is kept in the $4 < p_{Tt} < 5$ GeV/c range.

This unbalance affects the this analysis in two steps:

- when we relate the p_{out} magnitude to the $\langle z_t \rangle \sqrt{\langle k_T^2 \rangle}$ in [1] we assumed that both trigger and away-side parton momenta are in average the same. As demonstrated by Fig. 15 this is not true and the formula (20) in [1] had to be revised (see section 1.1 Eq. (7)).

- In the finale stage of the analysis we solve

$$x_h^{-1} \sqrt{\langle p_{\text{out}}^2 \rangle - \langle j_{Ty}^2 \rangle} (x_h^2 + 1) - \hat{x}_h^{-1}(k_T, x_h) \langle z_t(k_T, x_h) \rangle \sqrt{\langle k_T^2 \rangle} = 0 \quad (14)$$

for $\sqrt{\langle k_T^2 \rangle}$. The $\langle z_t \rangle$ and \hat{x}_h quantities are functions of $\langle k_T^2 \rangle$ and the evaluation has to be based on the knowledge of the fragmentation function and the framework of Lorentz invariant smearing (see section 3).

2.3 Width and yields from pythia and data

For the data comparison 100 M pythia events were generated with

- $\langle j_{Ty} \rangle = 0.45$ GeV/c, D=0.36 PARJ(21)
- independent fragmentation scheme, MSTP(1)=2
- initial and final state showering set to 0 (MSTP(61)=MSTP(71)=0)
- CKIN(3) = 2 GeV/c

and various values of $\sqrt{\langle k_T^2 \rangle}$. The comparison of the correlation width observed in the data as a function of $\langle p_{Tt} \rangle$ and $\langle p_{Ta} \rangle$ and simulated width for $\sqrt{\langle k_T^2 \rangle} = 2.5$ and 3.0 GeV/c is shown on Fig. 16.

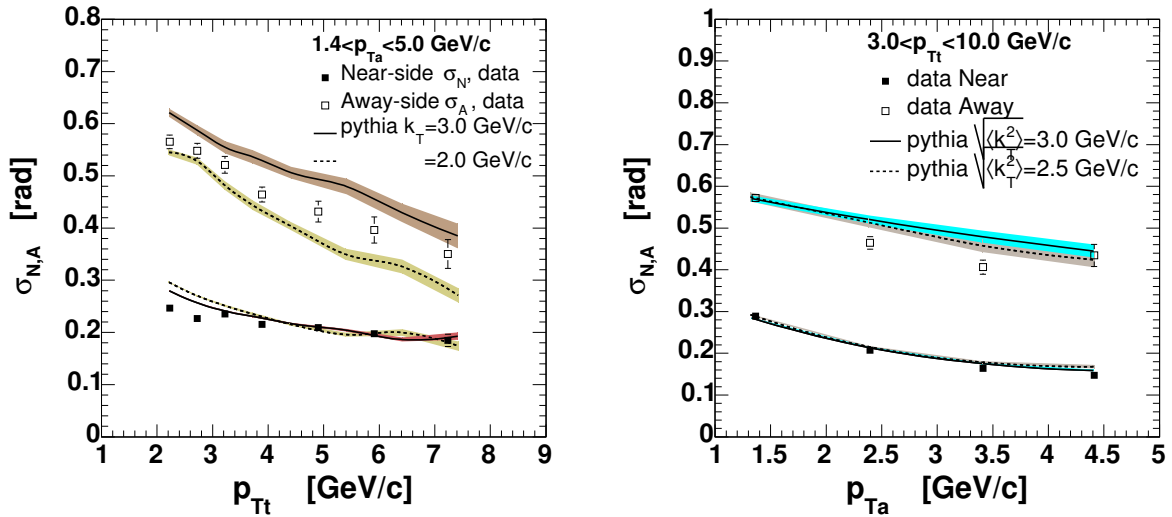


Figure 16: *Left*: The width of the near and away side peak for various $\langle p_{Tt} \rangle$ for relatively broad associated bin $1.4 < p_{Ta} < 5.0$ GeV/c compared to pythia with $\sqrt{\langle k_T^2 \rangle} = 3.0$ GeV/c (solid line) and 2.5 GeV/c (dashed line). The colored bands indicate the “statistical” error-bars due to the finite statistics in the pythia simulations. *Right*: The width of the near and away side peak for various $\langle p_{Ta} \rangle$ (the same bins as used in ppg039) for trigger bin $3.0 < p_{Tt} < 10.0$ GeV/c compared to pythia with $\sqrt{\langle k_T^2 \rangle} = 3.0$ GeV/c (solid line) and 2.5 GeV/c (dashed line).

It seems that pythia prefers $kt=2.5-3.0$ GeV/c. The per trigger yield for fixed $1.4 < p_{Ta} < 5.0$ GeV/c plotted with p_{Tt} is shown on lower panel of Fig. 17. The description of the yield extraction can be found in section 1.3 and App. A.2. The data are shown on lower panel (solid and empty boxes). When increasing the trigger momentum, the associated yield on the away side is increasing, reflecting the higher Q^2 and harder jet productions which leads to the higher multiplicity in the final state. The increase of the multiplicity on the near side is obviously suppressed by larger amount of energy taken from jet by higher momentum trigger particle.

Fig. 17 also indicates the importance of the initial/final state showering in pythia. Upper panel show the correlation function from the data (left) and from pythia (right) when both, initial and final showering, are turned off. The per trigger yield in this case undershoots the data by factor of 5-10.

In conclusion:

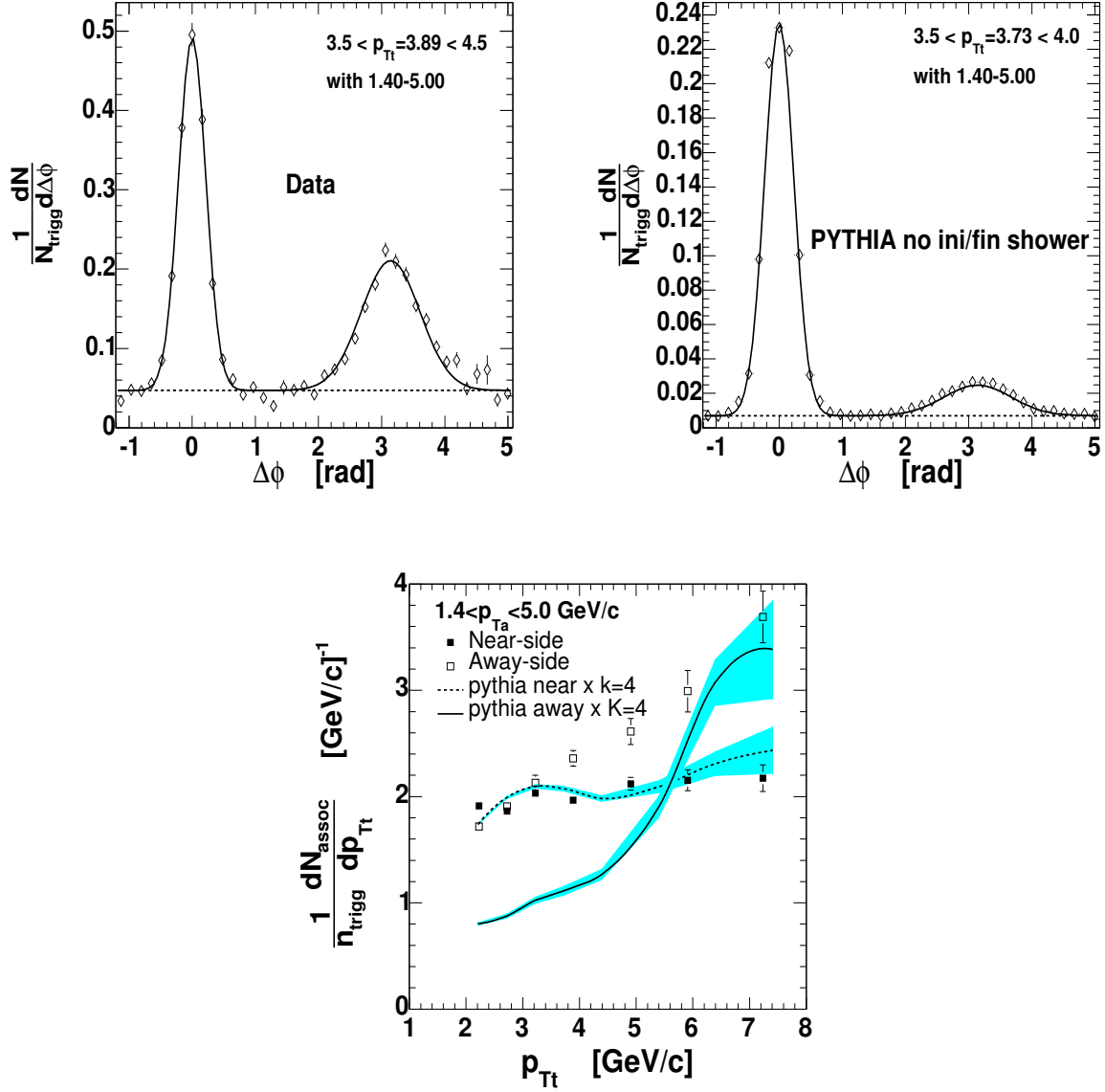


Figure 17: *Top*: Conditional yield $\Delta\phi$ distribution from the data (left panel) for $3.5 < p_{Tt} < 4.5$ GeV/ c and $1.4 < p_{Ta} < 5.0$ GeV/ c and for the same p_T selection yield distribution simulated by pythia when initial and final state showering is turned off. *Bottom*: Conditional yield $\Delta\phi$ distribution from the data (solid and open boxes) and from pythia plotted as a function p_{Tt} .

- The final state parton distributions from pythia with $\sqrt{\langle k_T^2 \rangle} = 3.5$ GeV/ c seems to be similar to what we see in the data.
- \hat{p}_{out} quantity in pythia reflects rather well the magnitude of input $\sqrt{\langle k_T^2 \rangle}$ parameter. The inclusive momentum imbalance measured by $\sqrt{\langle (\hat{p}_{Tt} - \hat{p}_{Ta})^2 \rangle}$ is equal to input $\sqrt{\langle k_T^2 \rangle}$ in the same way as $\sqrt{\langle (\hat{p}_{Tt} - \hat{p}_{T_{ax}})^2 \rangle}$.
- According to pythia, a large fraction of the jet multiplicity is due to the initial and final state showering.

3 k_T -smearing.

The existence of \vec{k}_T -vector has, in general, two effects. It changes the direction of the parton momenta causing the accoplanarity as discussed in the previous section. The k_T -vector also changes the magnitude of partons momenta causing the smearing of jet transverse momentum distribution and the unbalance of dijet momenta. The details of k_T -smearing is discussed in this section.

We considered three different classes of smearing which are relevant to this analysis.

- 1D smearing
- 2D vector smearing
- 2D Lorentz invariant smearing.

It is discussed in [15] that the k_T -smearing at high- \hat{p}_T can be approximated by 1D smearing with the variance $\langle k_{Tx}^2 \rangle / 2$. Since we are not sure at which \hat{p}_T this assumption does not affect the k_T extraction, we considered only the 2D Lorentz invariant smearing. Some comments on 1D and 2D vector smearing are to be found in A.4.1 and A.4.2

For the parameterization used in this analysis the k_T -smearing can be written as

$$\begin{aligned} \Sigma_Q(\hat{p}_T) &= \hat{p}_T f_Q(\hat{p}_T) = \frac{d\sigma_Q}{d\hat{p}_T} \quad \text{Unsmearred inv. dist.} \\ \Sigma'_Q(\hat{p}_{Tt}) &= k_T - \text{smearred } \Sigma_Q(\hat{p}_T) \approx \frac{1}{\sqrt{2\pi\sigma_{sm}^2}} \int_{-\infty}^{\infty} \Sigma_Q(\hat{p}_T - k_T) \cdot \exp\left(-\frac{k_T^2}{2\sigma_{sm}^2}\right) dk_T \end{aligned} \quad (15)$$

where σ_{sm}^2 is the smearing variance which is

$$\begin{aligned} &= \langle k_{Tx}^2 \rangle \text{ in the case of 1D smearing} \\ &\approx \langle k_{Tx}^2 \rangle \text{ in the case of 2D vector smearing} \\ &\approx \langle k_{Tx}^2 \rangle / 2 \text{ in the case of 2D Lorentz invariant smearing.} \end{aligned}$$

The explanation for the latter two cases can be found in following sections.

3.1 2D Lorentz invariant smearing.

The Lorentz invariant 2D smearing preserves the invariant mass ($\hat{M}_{inv} = 4\hat{p}_T^2$) of the parton pair before and after smearing. In this case the individual \vec{k}_T -vector associated with trigger (k_{Tt}) and associated (k_{Ta}) jet are correlated. The concept of individual \vec{k}_T -vectors assigned to each jet is not quite reasonable and only the net pair momentum $\hat{p}_{T\text{pair}}$ has physical meaning of being a boost vector from dijet rest frame in transverse plane, where trigger and associated jets momenta are opposite, to the lab frame. It is the same analogy to the dijet unbalance and accoplanarity in longitudinal direction which is due to $x_F = x_1 - x_2$.

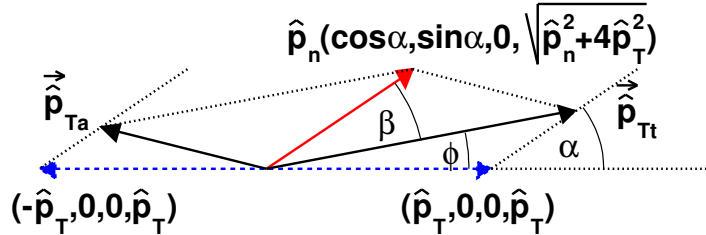


Figure 18: Back to back partons in hard scattering rest frame (blue dashed arrows) with four-momenta $(\hat{p}_T, 0, 0, \hat{p}_T)$ and $(-\hat{p}_T, 0, 0, \hat{p}_T)$ in $(-, -, -, +)$ metrics moving along $\hat{p}_{T\text{pair}}$.

The schematic view of Lorentz invariant smearing is shown on Fig. 18. It is easy to see that as in the case of noninvariant smearing all vectors are adding up as

$$\vec{\hat{p}}_n \equiv \vec{\hat{p}}_{Tt} + \vec{\hat{p}}_{Ta} = \vec{k}_{Tt} + \vec{k}_{Ta} \quad (16)$$

but in the invariant smearing \vec{k}_{T_t} and \vec{k}_{T_a} (and thus $\vec{p}_{T_{\text{pair}}}$) are collinear

$$\vec{k}_{T_t} \times \vec{k}_{T_a} = 0 \quad (17)$$

In order to evaluate the \hat{p}_{T_t} or \hat{p}_{T_a} distribution after k_T -smearing we have to find the new formula for $\mathcal{P}(\hat{p}_{T_{t,a}})|_{\hat{p}_T}$ as we have done in Eq. (70). k_{T_t} and k_{T_a} vectors are not any longer statistically independent and the only vector which can be assumed as 2D Gaussian random vector is \hat{p}_n (the net pair momentum see Eq. (16))

$$\frac{d\mathcal{P}(\hat{p}_n)}{\hat{p}_n d\hat{p}_n} = \frac{1}{2\pi \langle k_T^2 \rangle} \exp\left(-\frac{\hat{p}_n^2}{2 \langle k_T^2 \rangle}\right). \quad (18)$$

In order to calculate $\mathcal{P}(\hat{p}_{T_{t,a}})|_{\hat{p}_T}$ in the Lorentz invariant smearing one has to calculate the magnitude of the boost vector $\hat{p}_{T_{\text{pair}}}$ knowing only the \hat{p}_T and \hat{p}_{T_t} four momenta.

Knowledge of \hat{p}_T and \hat{p}_{T_t} determines also $\vec{k}_{T_t} = \vec{p}_{T_t} - \vec{p}_T$ and in order to evaluate the boost vector $\vec{p}_{T_{\text{pair}}}$ the only missing quantity is the magnitude of \vec{k}_{T_a} . We derived the magnitude of \vec{k}_{T_a} from the requirement

$$M_{inv}^2 = 4\hat{p}_T^2 = 2\hat{p}_{T_t}\hat{p}_{T_a} - 2\vec{p}_{T_t}\vec{p}_{T_a} \quad (19)$$

and we eliminate \vec{p}_{T_a} by substitution $\vec{p}_{T_a} = \vec{k}_{T_a} - \vec{p}_T$ and $\hat{p}_{T_a} = \sqrt{k_{T_a}^2 + \hat{p}_T^2 - 2k_{T_a}\hat{p}_T \cos \alpha}$ and thus \vec{k}_{T_a} magnitude can be found as a solution of a quadratic equation

$$\hat{p}_{T_t} \sqrt{k_{T_a}^2 + \hat{p}_T^2 - 2k_{T_a}\hat{p}_T \cos \alpha} - \hat{p}_{T_t}k_{T_a} \cos \beta + \hat{p}_{T_t,x}\hat{p}_T = 2\hat{p}_T^2. \quad (20)$$

and the two solutions, $k_{T_{a+}}$ and $k_{T_{a-}}$, are

$$\begin{aligned} k_{T_{a+}} &= \frac{\hat{p}_T}{\hat{p}_{T_t}(1 - \cos^2 \beta)} (2\hat{p}_T \cos \beta + \hat{p}_{T_t} \cos \alpha - \hat{p}_{T_t,x} \cos \beta + \sqrt{D}) \\ k_{T_{a-}} &= \frac{\hat{p}_T}{\hat{p}_{T_t}(1 - \cos^2 \beta)} (2\hat{p}_T \cos \beta + \hat{p}_{T_t} \cos \alpha - \hat{p}_{T_t,x} \cos \beta - \sqrt{D}) \\ D &= 4\hat{p}_T^2 + (\cos^2 \alpha + \cos^2 \beta - 1)\hat{p}_{T_t}^2 + 4\hat{p}_T(\hat{p}_{T_t} \cos \alpha \cos \beta - \hat{p}_{T_t,x}) - 2\hat{p}_{T_t}\hat{p}_{T_t,x} \cos \alpha \cos \beta + \hat{p}_{T_t,x}^2. \end{aligned} \quad (21)$$

All variables in Eq. (21) are known except $\cos \beta$. However, we can easily evaluate

$$\begin{aligned} \cos \alpha &= \frac{(\vec{p}_{T_t} - \vec{p}_T) \cdot \vec{p}_T}{|\vec{p}_{T_t} - \vec{p}_T| |\vec{p}_T|} = \frac{\hat{p}_{T_t,x} - \hat{p}_T}{\sqrt{(\hat{p}_{T_t,x} - \hat{p}_T)^2 + \hat{p}_{T_t,y}^2}} \\ \cos \phi &= \hat{p}_{T_t,x} / \hat{p}_{T_t} \\ \cos \beta &= \cos \alpha \cos \phi + \sqrt{(1 - \cos^2 \alpha)(1 - \cos^2 \phi)} \end{aligned} \quad (22)$$

Since now all the quantities are known, we can evaluate the $\mathcal{P}(\hat{p}_{T_{t,a}})|_{\hat{p}_T}$ as

$$\mathcal{P}(\hat{p}_{T_t})|_{\hat{p}_T} = \left(\frac{\hat{p}_T^2 + 1.8}{\hat{p}_{T_t}} + \frac{\hat{p}_{T_t}}{2.4} \right) \frac{1}{\langle k_T^2 \rangle} \left[\int_{0+\epsilon}^{\pi/2} \exp\left(-\frac{(k_{T_t} + k_{T_{a+}})^2}{2 \langle k_T^2 \rangle}\right) d\phi + \int_{\pi/2}^{\pi-\epsilon} \exp\left(-\frac{(k_{T_t} + k_{T_{a-}})^2}{2 \langle k_T^2 \rangle}\right) d\phi \right] d\hat{p}_{T_t} \quad (23)$$

The ϵ parameter here is to eliminate the ‘‘collinear divergence’’ when $\phi \rightarrow 0$ or π and both nominator and denominator in Eq. (21) go to zero. We can completely ignore this since the ϵ -region around 0 and π is infinitely small or we can replace the collinear case by simple formula

$$k_{T_a} = \hat{p}_T - \hat{p}_{T_a} = \frac{\hat{p}_T}{\hat{p}_{T_t}} (\hat{p}_{T_t} - \hat{p}_T) \quad (24)$$

where we used $4\hat{p}_T^2 = 4\hat{p}_{T_t}\hat{p}_{T_a}$. The Gaussian functions in Eq. (23) contain various powers of $\cos \phi$ which makes it impossible to find an analytical integral. The numerical solutions for various \hat{p}_T values are shown on Fig. 19.

An analytical solution of noninvariant smearing

$$\mathcal{P}(\hat{p}_{T_t})|_{\hat{p}_T} = \frac{1}{\langle \sigma_{sm}^2 \rangle} \exp\left(-\frac{\hat{p}_T^2 + \hat{p}_{T_t}^2}{2 \langle \sigma_{sm}^2 \rangle}\right) I_0\left(\frac{\hat{p}_T \hat{p}_{T_t}}{\langle \sigma_{sm}^2 \rangle}\right) \hat{p}_{T_t} d\hat{p}_{T_t} \quad (25)$$

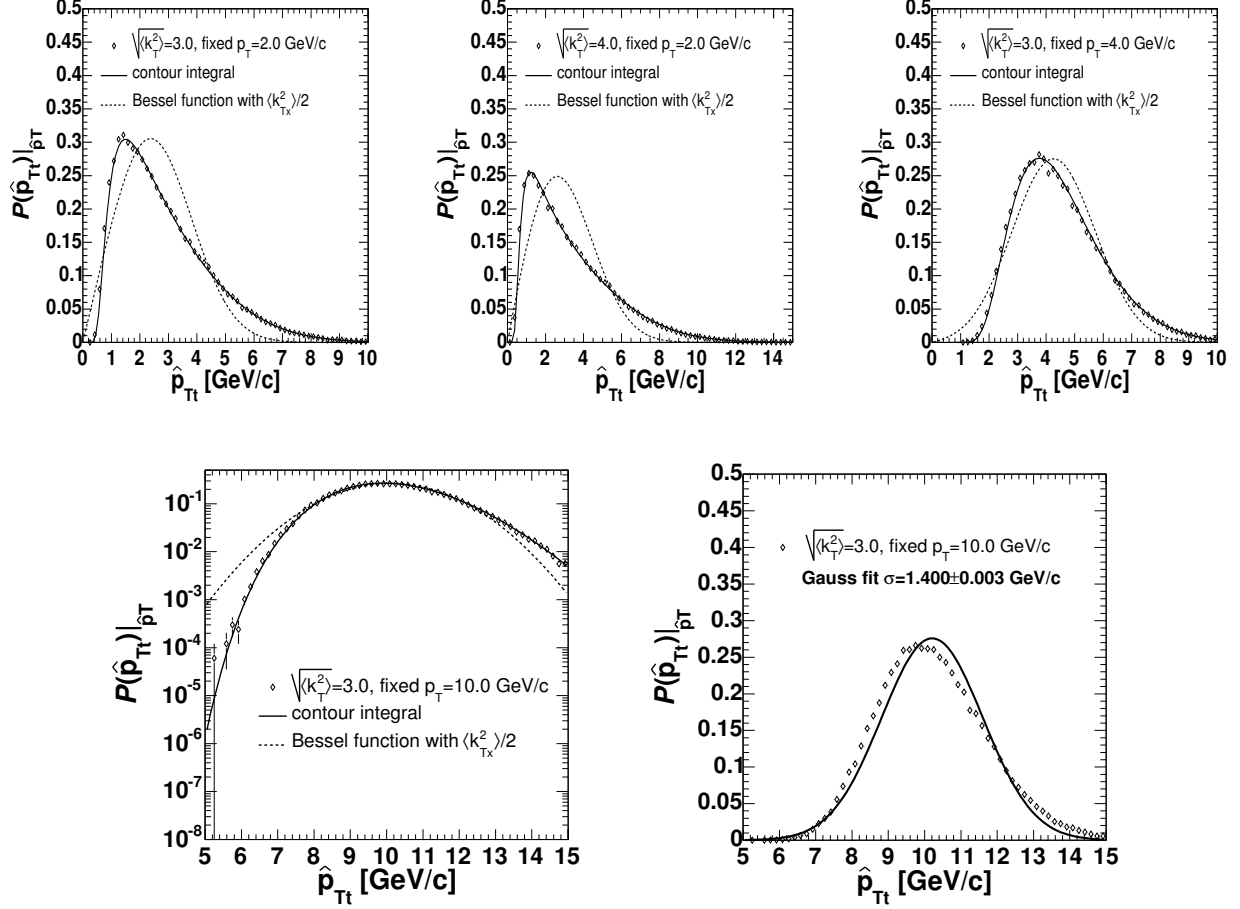


Figure 19: The conditional probabilities for detecting a parton of momentum \hat{p}_{Tt} resulting from a Lorentz invariant smearing of fixed parton of momentum $\hat{p}_T=2$ (upper left), 4 (upper right) and 10 (lower two panels). Simulated distributions shown with open diamonds. The contour integral according Eq. (23) is represented by a solid line. The noninvariant Bessel function according Eq. (25) with $\sigma_{sm}^2 = \langle k_{Tx}^2 \rangle / 2$ is represented by a dotted line. The lower right plot shows the simulated $\mathcal{P}(\hat{p}_{Tt})|_{\hat{p}_T}$ distribution with the Gaussian fit.

with $\sigma_{sm}^2 = \langle k_{Tx}^2 \rangle / 2$ is shown with dotted lines. As one can see at high \hat{p}_T

$$\mathcal{P}(\hat{p}_{Tt})|_{\hat{p}_T \rightarrow \infty} \approx \exp\left(-\frac{(\hat{p}_{Tt} - \hat{p}_T)^2}{\langle k_{Tx}^2 \rangle}\right). \quad (26)$$

The question would be, at which \hat{p}_T is the Gaussian approximation good enough and how does one cope with the low- \hat{p}_T region where the deviation from a Gaussian shape is quite substantial.

Another interesting observation one can make is that even at $\hat{p}_T=10$ GeV/c, the invariant smearing with $\langle k_T^2 \rangle=3$ GeV/c still deviates from a Gaussian shape. The Gaussian fits gives $\sigma = 1.4$ GeV/c, whereas the expected value is $\sqrt{\langle k_{Tx}^2 \rangle}/2=1.5$ GeV/c.

Comparing simulated distributions with Eq. (23) (Fig. 19) one can notice excellent agreement between simulated distributions and an evaluation according to Eq. (23). However, the generalized Bessel smearing function Eq. (25) with $\sigma_{sm}^2 = \langle k_{Tx}^2 \rangle / 2$ also fits the simulation reasonably well and it has the advantage that this “elementary” function does not require numerical integration.

4 Fragmentation function

We have shown (see Eq. (7)) that the width of the away side correlation peak is related to the product of $\langle z_t \rangle \sqrt{\langle k_T^2 \rangle}$. In order to extract the $\langle k_T^2 \rangle$ value, knowledge of $\langle z_t \rangle$ and \hat{x}_h is necessary. Fragmentation functions from e^+e^- collisions, weighted by the appropriate hard-scattering constituent cross-sections and Q^2 evolution could in principle be used. However, the shape of the fragmentation function can be deduced from present measurements using the combined analysis of the inclusive and trigger-associated particles' x_E -distributions.

4.1 Inclusive fragmentation

Generally, the invariant cross section for inclusive hadron production from jets can be parametrized in the following way. First, we assume that the number of parton fragments (consider only pions for simplicity) at a given p_T corresponds to the sum over all contributions from parton momenta \hat{p}_T from $p_T < \hat{p}_T < \sqrt{s}/2$. The joint probability of detecting a pion with $p_T = z\hat{p}_T$ originating from a parton with \hat{p}_T can be written as

$$\begin{aligned} \frac{d^2\sigma_\pi}{\hat{p}_T d\hat{p}_T dz} &= \frac{d\sigma_q}{\hat{p}_T d\hat{p}_T} \times D_\pi^q(z) \\ &= f_q(\hat{p}_T) \times D_\pi^q(z). \end{aligned} \quad (27)$$

Here we use $f_q(\hat{p}_T)$ which represents the final state scattered-parton invariant spectrum $d\sigma_q/\hat{p}_T d\hat{p}_T$, and $D_\pi^q(z)$, which represents the fragmentation function. The first term in Eq. (27) can be viewed as a probability of finding a parton with transverse momentum \hat{p}_T and the second term corresponds to the probability that the parton \hat{p}_T fragments into a particle of momentum $p_T = z\hat{p}_T$. With a simple change of variables from \hat{p}_T to $p_T = z\hat{p}_T$, we obtain the joint probability of a pion with p_T which is a fragment with momentum fraction z from a parton with $\hat{p}_T = p_T/z$:

$$\frac{d^2\sigma_\pi}{p_T dp_T dz} = f_q\left(\frac{p_T}{z}\right) \cdot D_\pi^q(z) \frac{1}{z^2}. \quad (28)$$

The p_T and z dependences do not factorize. However, the p_T spectrum may be found by integrating over all values of $\hat{p}_T \geq p_T$ to $\hat{p}_{Tmax} = \sqrt{s}/2$, which corresponds to values of z from $x_T = 2p_T/\sqrt{s}$ to 1.

$$\frac{1}{p_T} \frac{d\sigma_\pi}{dp_T} = \int_{x_T}^1 f_q\left(\frac{p_T}{z}\right) \cdot D_\pi^q(z) \frac{dz}{z^2} \quad (29)$$

Alternatively, for any fixed value of p_T one can evaluate the $\langle z(p_T) \rangle$, integrated over the parton spectrum:

$$\langle z(p_T) \rangle = \frac{\int_{x_T}^1 z D_\pi^q(z) f_q(p_T/z) \frac{dz}{z^2}}{\int_{x_T}^1 D_\pi^q(z) f_q(p_T/z) \frac{dz}{z^2}}. \quad (30)$$

From the scaling properties of QCD and from the shape of the π^0 invariant cross section itself, which is a pure power law for $p_T \geq 3$ GeV/c [10], one can deduce that $f_q(\hat{p}_T)$ should have a power law shape. In this case the hadron spectrum also has power law shape because

$$\frac{1}{p_T} \frac{d\sigma}{dp_T} \approx \int_{x_T}^1 D_\pi^q(z) \cdot \left(\frac{p_T}{z}\right)^{-n} \frac{dz}{z^2} \approx p_T^{-n} \int_{x_T}^1 D_\pi^q(z) \cdot z^{n-2} dz \quad (31)$$

and the last integral depends only weakly on p_T due to x_T . For small parton \hat{p}_T (below 3-4 GeV/c) the power law shape is no longer valid. The $f_q(\hat{p}_T)$ should also diminish for very high $\hat{p}_T \rightarrow \sqrt{s}/2$ where the phase space available for hard parton production diminishes, again not relevant for the present purposes.

We used a power law parameterization for the final state scattered-parton invariant spectrum:

$$f_q(\hat{p}_T) \propto \frac{1}{\hat{p}_T^n} \quad (32)$$

where n is a free parameter which can be determined from the fit of Eq. (29) to the measured π^0 cross section. There is, however, one more missing piece of information - the shape of the fragmentation function D_π^q . In order to extract this information from the data on associated x_E -distributions will be analyzed.

4.2 Associated x_E distributions

The x_E variable, defined by Eq. (4), to first order, approximates the slope of the fragmentation function in the limit of high values of p_{Tt} , where there is sufficient collinearity between the trigger particle and the fragmenting parton. In this case where $j_T \ll p_{Tt}$ and $k_T \ll p_{Tt}$ one can assume that $p_{Tt} = \hat{p}_{Tt}/z_t$ and $x_E \cdot z_t = \hat{x}_h p_{Ta} \cdot \cos \Delta\phi / \hat{p}_{Ta} = \hat{x}_h z_a$, and thus the slopes of $D(z_a)$ and x_E are related as

$$\langle z_a \rangle = \langle x_E \rangle \frac{\langle z_t \rangle}{\hat{x}_h}. \quad (33)$$

The x_E distributions of particles associated with trigger particles in the 3-8 GeV/c range of transverse momentum are plotted in Fig. 20. The dashed lines represent the exponential fits. The slopes of these exponentials range from -5.8 ($3 < p_{Tt} < 4$ GeV/c) to -7.8 ($7 < p_{Tt} < 8$ GeV/c). This is qualitatively and quantitatively different from the similar measurement done by CCOR collaboration at $\sqrt{s}=62.4$ GeV where the slopes of exponential fits to the x_E distributions were found to be ≈ -5.3 and independent of the trigger transverse momenta. That observation also supported the hypothesis of the x_E distribution being a good approximation of the fragmentation function. We also note that the x_E distributions are not quite exponential and at large values of x_E there is a tail similar to the power law tail of the single inclusive p_T -distribution.

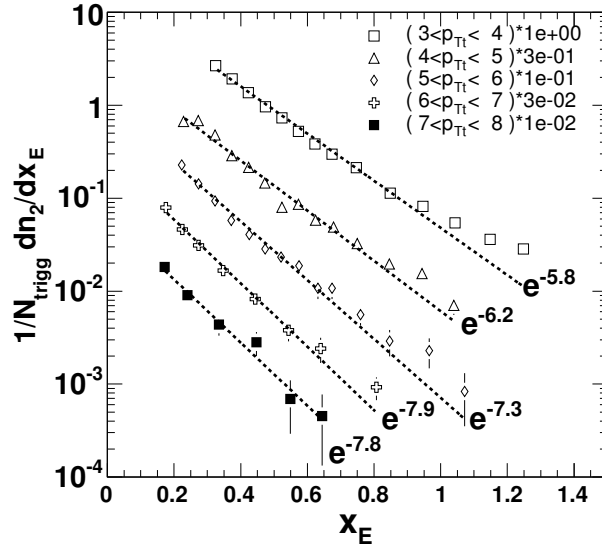


Figure 20: The distribution of associated particles with x_E variable for various trigger particle p_{Tt} indicated in the legend.

The reason why the x_E distributions do not have the same slope and why there is a “power law” tail at large x_E is the same as that which causes $\langle z_t \rangle \sqrt{\langle k_T^2 \rangle}$ to decrease with the associated particle transverse momentum. By sampling different regions of p_{Ta} , the average momentum of the parton fragmenting into a trigger particle also changes. This kind of trigger bias causes the hard scattering kinematics, the value of \hat{s} , to not be fixed for the case where p_{Tt} is fixed but p_{Ta} varies. Taking this into account, one can not treat the associated x_E distribution as a rescaled fragmentation function, but rather as a folding of the two fragmentation processes of trigger and associated jets.

The description of an associated distribution detected under the condition of the existence of a trigger particle requires an extension of the formulae discussed in 4.1 and is a subject of the next section.

4.3 Conditional fragmentation

For the description of the detection a single particle which is the result of jet fragmentation, recall Eq. (27)

$$\frac{d^2\sigma_\pi}{d\hat{p}_T dz_t} = \frac{d\sigma_q}{d\hat{p}_T} \times D_\pi^q(z_t) = \hat{p}_T f_Q(\hat{p}_T) \times D_\pi^q(z_t) \equiv \Sigma_Q(\hat{p}_T) \times D_\pi^q(z_t) \quad (34)$$

where we have now explicitly labeled the z of the trigger particle as z_t , and defined

$$\Sigma_Q(\hat{p}_T) \equiv \hat{p}_T f_Q(\hat{p}_T) \quad .$$

When k_T smearing is introduced, configurations for which the high p_T parton pair is on the average moving towards the trigger particle are favored due to the steeply falling \hat{p}_T spectrum, such that:

$$\langle \hat{p}_{Tt} - \hat{p}_T \rangle \simeq \frac{1}{2} \langle \hat{p}_{Tt} - \hat{p}_{Ta} \rangle \equiv s(k_T)$$

with small variance σ_s^2 , and we explicitly introduced \hat{p}_{Tt} and \hat{p}_{Ta} to represent the transverse momenta of the trigger and away partons. The single inclusive p_{Tt} spectrum is now given by

$$\frac{d^2\sigma_\pi}{d\hat{p}_{Tt}dz_t} = \Sigma'_Q(\hat{p}_{Tt}) \times D_\pi^q(z_t)$$

where the trigger parton \hat{p}_{Tt} spectrum after k_T smearing is

$$\frac{d\sigma_q}{\hat{p}_{Tt}} = \Sigma'_Q(\hat{p}_{Tt}) \quad .$$

Then, the conditional probability for finding the away side parton with \hat{p}_{Ta} and z_a , given \hat{p}_{Tt} (and z_t), is:

$$\left. \frac{dP(\hat{p}_{Ta}, z_a)}{d\hat{p}_{Ta}dz_a} \right|_{\hat{p}_{Tt}} = C(\hat{p}_{Ta}, \hat{p}_{Tt}, k_T) D_\pi^q(z_a)$$

where $C(\hat{p}_{Ta}, \hat{p}_{Tt}, k_T)$ represents the distribution of the transverse momentum of the away parton \hat{p}_{Ta} , given \hat{p}_{Tt} and k_T , which can be written as:

$$C(\hat{p}_{Ta}, \hat{p}_{Tt}, k_T) = \frac{1}{\sqrt{2\pi\sigma_s^2}} \exp\left(\frac{-[\hat{p}_{Ta} - (\hat{p}_{Tt} - 2s(k_T))]^2}{2\sigma_s^2}\right) \quad . \quad (35)$$

Then

$$\frac{d\sigma_q}{d\hat{p}_{Tt}dz_t d\hat{p}_{Ta}dz_a} = \frac{d\sigma_q}{d\hat{p}_{Tt}dz_t} \times \left. \frac{dP(\hat{p}_{Ta}, z_a)}{d\hat{p}_{Ta}dz_a} \right|_{\hat{p}_{Tt}} \quad .$$

In general, $\sigma_s/s(k_T)$ is small (see section 3) so that $C(\hat{p}_{Ta}, \hat{p}_{Tt}, k_T)$ is well approximated by a δ function and we may take

$$\hat{p}_{Ta} = \hat{p}_{Tt} - 2s(k_T) = \hat{x}_h \hat{p}_{Tt} \quad ,$$

so that

$$\frac{d\sigma_q}{d\hat{p}_{Tt}dz_t dz_a} = \Sigma'_Q(\hat{p}_{Tt}) D_\pi^q(z_t) D_\pi^q(z_a)$$

where

$$z_a = \frac{p_{Ta}}{\hat{p}_{Ta}} = \frac{p_{Ta}}{\hat{x}_h \hat{p}_{Tt}} = \frac{z_t p_{Ta}}{\hat{x}_h \hat{p}_{Tt}} \quad .$$

Changing variables from \hat{p}_{Tt}, z_t to p_{Tt}, z_t as above, and similarly from z_a to p_{Ta} , we obtain

$$\frac{d\sigma_\pi}{d\hat{p}_{Tt}dz_t dp_{Ta}} = \frac{1}{\hat{x}_h z_t} \Sigma'_q\left(\frac{p_{Tt}}{z_t}\right) D_\pi^q(z_t) D_\pi^q\left(\frac{z_t p_{Ta}}{\hat{x}_h \hat{p}_{Tt}}\right) \quad (36)$$

where for integrating over z_t or finding $\langle z_t \rangle$ for fixed p_{Tt} , p_{Ta} , the minimum value of z_t is $z_t^{\min} = 2p_{Tt}/\sqrt{s} = x_{Tt}$ and the maximum value is:

$$z_t^{\max} = \hat{x}_h \frac{p_{Tt}}{p_{Ta}} = \frac{\hat{x}_h}{x_h} \quad ,$$

where the function $\hat{x}_h(p_{Tt}, p_{Ta})$ is given by Eq. (5).

As we discussed in section 3 the Gaussian approximation for the smearing function Eq. (35) does not work so well in the low \hat{p}_T region (see Fig. 19). The product of the steeply falling parton distribution function and the fragmentation function (see A.5) is peaked at $z \approx 1$ preferring “small” parton momenta. We have developed more accurate description of the conditional yields taking into account the k_T smearing. The basic idea of this

approach is following: Numerical unfolding of $\Sigma'_Q(\hat{p}_{Tt})$ obtained from the simultaneous fit to the x_E -distributions discussed in section 4 is performed. Knowing an unsmeared parton distribution $\Sigma_Q(\hat{p}_T)$ the conditional probability distributions of the near and away side partons given fragments momenta p_{Tt} , p_{Ta} and the average $\langle k_T \rangle$ can be calculated without Eq. (35) assumption.

Let us consider the configuration depicted on Fig. 21. The two back-to-back partons in \hat{s} frame undergo the Lorentz boost determined by net pair momentum

$$\vec{p}_n = \vec{p}_{T\text{pair}} = \vec{\hat{p}}_{Tt} + \vec{\hat{p}}_{Ta} = \vec{k}_{Tt} + \vec{k}_{Ta} \quad (37)$$

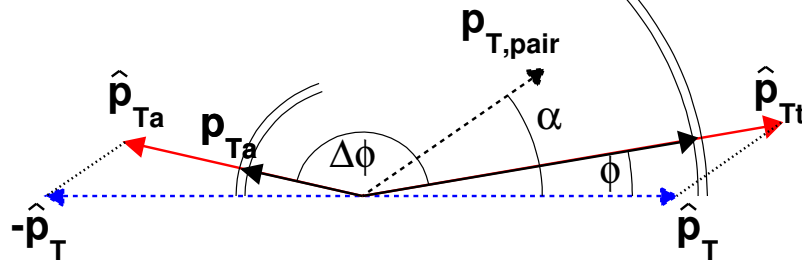


Figure 21: Back to back partons in hard scattering rest frame (blue dashed arrows) with four-momenta $(\hat{p}_T, 0, 0, \hat{p}_T)$ and $(-\hat{p}_T, 0, 0, \hat{p}_T)$ in $(-, -, -, +)$ metrics moving along \hat{p}_n for event where detection of p_{Tt} and p_{Ta} is required (the j_T contribution is neglected). The $p_{Tt} > p_{Ta}$ condition implies that the events with \hat{p}_n pointing more in the direction of p_{Tt} are selected.

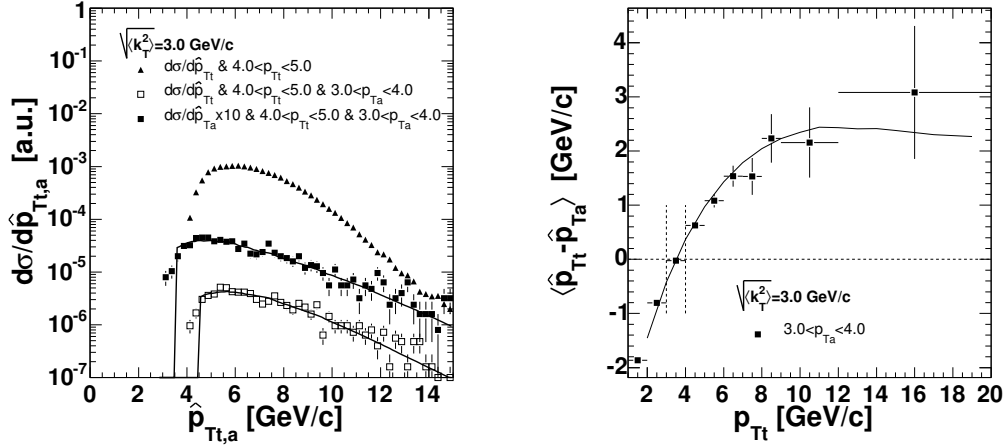


Figure 22: *Left*: The parton distribution $d\sigma/d\hat{p}_{Tt}|_{p_{Tt}, p_{Ta}}$ and $d\sigma/d\hat{p}_{Ta}|_{p_{Tt}, p_{Ta}} \times 10$ from the pythia simulation and calculated according Eq. (39) and Eq. (40). The sharp cut off in the calculation is not seen in simulations because of finite bin size $4.0 < p_{Tt} < 5.0$ GeV/c and $3.0 < p_{Ta} < 4.0$ GeV/c used in the simulation. *Right*: Simulated average momentum unbalance for the associated particles in $3.0 < p_{Ta} < 4.0$ GeV/c bin and calculated according Eq. (43). The two vertical dashed line indicates the range where p_{Tt} and p_{Ta} bins are equal and the parton momenta unbalance vanishes (fixed correlations).

If we denote an angle between the unsmeared parton momentum and k_T -vector (or \vec{p}_n) as α (see Fig. 21) then with help of Eq. (75) we can write the conditional probability distribution of trigger parton momenta, \hat{p}_{Tt} , as

$$\left. \frac{d\sigma}{d\hat{p}_{Tt} d\alpha d\hat{p}_T} \right|_{p_{Tt}, p_{Ta}} = \hat{p}_{Tt} \cdot \Sigma_Q(\hat{p}_T) \cdot \hat{p}_n \cdot G(\hat{p}_n(\vec{r}_t)) \cdot D_\pi^q\left(\frac{p_{Tt}}{\hat{p}_{Tt}}\right) \frac{p_T}{\hat{p}_{Tt}^2} \cdot D_\pi^q\left(\frac{p_{Ta}}{\hat{p}_{Ta}}\right) \frac{p_{Ta}}{\hat{p}_{Ta}^2} \quad (38)$$

where $G(\hat{p}_n) = \exp(-\hat{p}_n^2/2\langle k_T^2 \rangle)$ describes the Gaussian probability distribution of the net pair momentum magnitude distribution, $\Sigma_Q(\hat{p}_T)$ is the unsmeared parton momentum distribution, D_π^q is the fragmentation function

and $\vec{r}_t = (\hat{p}_{Tt}, \phi, \hat{p}_T, k_T)$ is the phase space vector. The \hat{p}_{Tt} is chosen to be an integration variable and \hat{p}_{Ta} is fully determined by given values of \hat{p}_{Tt} , \hat{p}_T , angle ϕ and by the requirement of Lorentz invariance (see section 3).

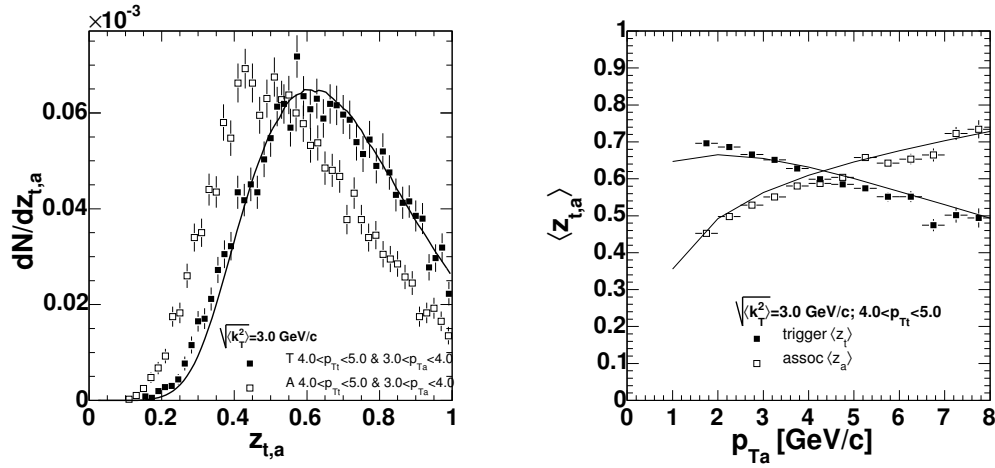


Figure 23: *Left:* The conditional distribution $dN/dz_{t,a}|_{p_{Tt}, p_{Ta}}$ for $4 < p_{Tt} < 5$ GeV/c and $3 < p_{Ta} < 4$ GeV/c on the trigger side (solid squares) and associated side (empty squares) from the pythia simulations. The solid line corresponds to the Eq. (39) expressed in terms of z_t . *Right:* Average z of a trigger and associated particle as a function of p_{Ta} from pythia and according Eq. (41).

In order to evaluate $\langle z_t(k_T) \rangle|_{p_{Tt}, p_{Ta}}$ and $\hat{x}_h(k_T)|_{p_{Tt}, p_{Ta}}$ we have to evaluate first the parton distribution for events where given p_{Tt} and p_{Ta} are detected. This conditional cross section can be expressed as a contour integral over ϕ angle (see Fig. 21)

$$\begin{aligned} \frac{d\sigma}{d\hat{p}_{Tt}} \Big|_{p_{Tt}, p_{Ta}} &= 2 \int_0^{\sqrt{s}/2} \int_0^\pi \frac{d\sigma}{d\hat{p}_{Tt} d\hat{p}_T d\phi} \Big|_{p_{Tt}, p_{Ta}} d\phi d\hat{p}_T \\ &= D_\pi^q\left(\frac{p_{Tt}}{\hat{p}_{Tt}}\right) \frac{2}{\hat{p}_{Tt}} \int_0^{\sqrt{s}/2} \Sigma_Q(\hat{p}_T) \int_0^\pi \hat{p}_n(\vec{r}_t) G(\hat{p}_n(\vec{r}_t)) \cdot D_\pi^q\left(\frac{p_{Ta}}{\hat{p}_{Ta}(\vec{r}_t)}\right) \frac{1}{\hat{p}_{Ta}^2(\vec{r}_t)} d\phi d\hat{p}_T \end{aligned} \quad (39)$$

The $d\sigma/d\hat{p}_{Ta}|_{p_{Tt}, p_{Ta}}$ distribution can be derived from Eq. (39) just by rotation $\hat{p}_{Tt} \rightarrow \hat{p}_{Ta}$ and $\hat{p}_{Ta} \rightarrow \hat{p}_{Tt}$

$$\frac{d\sigma}{d\hat{p}_{Ta}} \Big|_{p_{Tt}, p_{Ta}} = D_\pi^q\left(\frac{p_{Ta}}{\hat{p}_{Ta}}\right) \frac{2}{\hat{p}_{Ta}} \int_0^{\sqrt{s}/2} \Sigma_Q(\hat{p}_T) \int_0^\pi \hat{p}_n(\vec{r}_a) G(\hat{p}_n(\vec{r}_a)) \cdot D_\pi^q\left(\frac{p_{Tt}}{\hat{p}_{Tt}(\vec{r}_a)}\right) \frac{1}{\hat{p}_{Tt}^2(\vec{r}_a)} d\phi d\hat{p}_T \quad (40)$$

where $\vec{r}_a = (\hat{p}_{Ta}, \phi, \hat{p}_T, k_T)$. The $\langle z_t(k_T) \rangle|_{p_{Tt}, p_{Ta}}$ and $\hat{x}_h(k_T)|_{p_{Tt}, p_{Ta}}$ quantities can then be evaluated as

$$\langle z_t(k_T) \rangle|_{p_{Tt}, p_{Ta}} = \frac{\mathcal{Z}(1)}{\mathcal{Z}(0)} \quad (41)$$

where

$$\mathcal{Z}(n) = \int_{x_{Tt}}^1 z_t^{n-1} D_\pi^q(z_t) \int_0^{\sqrt{s}/2} \Sigma_Q(\hat{p}_T) \int_0^\pi \hat{p}_n G(\hat{p}_n(\vec{r}_{zt})) \cdot D_\pi^q\left(\frac{p_{Ta}}{\hat{p}_{Ta}(\vec{r}_{zt})}\right) \frac{1}{\hat{p}_{Ta}^2(\vec{r}_{zt})} d\phi d\hat{p}_T dz_t \quad (42)$$

and $\vec{r}_{zt} = (p_{Tt}/z_t, \phi, \hat{p}_T, k_T)$. The $\hat{x}_h(k_T)|_{p_{Tt}, p_{Ta}}$ is evaluated as

$$\hat{x}_h(k_T)|_{p_{Tt}, p_{Ta}} = \frac{\langle \hat{p}_{Ta} \rangle}{\langle \hat{p}_{Tt} \rangle} \Big|_{p_{Tt}, p_{Ta}} = \frac{\mathcal{X}_a(1) \mathcal{X}_t(0)}{\mathcal{X}_a(0) \mathcal{X}_t(1)} \quad (43)$$

where

$$\begin{aligned} \mathcal{X}_t(n) &= \int_{p_{Tt}}^{\sqrt{s}/2} \hat{p}_{Tt}^{n-1} D_\pi^q\left(\frac{p_{Tt}}{\hat{p}_{Tt}}\right) \int_0^{\sqrt{s}/2} \Sigma_Q(\hat{p}_T) \int_0^\pi \hat{p}_n(\vec{r}_t) G(\hat{p}_n(\vec{r}_t)) \cdot D_\pi^q\left(\frac{p_{Ta}}{\hat{p}_{Ta}(\vec{r}_t)}\right) \frac{1}{\hat{p}_{Ta}^2(\vec{r}_t)} d\phi d\hat{p}_T \hat{p}_{Tt} \\ \mathcal{X}_a(n) &= \int_{p_{Ta}}^{\sqrt{s}/2} \hat{p}_{Ta}^{n-1} D_\pi^q\left(\frac{p_{Ta}}{\hat{p}_{Ta}}\right) \int_0^{\sqrt{s}/2} \Sigma_Q(\hat{p}_T) \int_0^\pi \hat{p}_n(\vec{r}_a) G(\hat{p}_n(\vec{r}_a)) \cdot D_\pi^q\left(\frac{p_{Tt}}{\hat{p}_{Tt}(\vec{r}_a)}\right) \frac{1}{\hat{p}_{Tt}^2(\vec{r}_a)} d\phi d\hat{p}_T \hat{p}_{Ta} \end{aligned}$$

We have tested the above formulae on pythia simulation. The partons' distributions from pythia events with the condition of detecting $p_{T_t}=4.5$ GeV/ c and $p_{T_a}=3.5$ GeV/ c are compared to calculation according to Eq. (39) and Eq. (40) with $\Sigma_Q(\hat{p}_T)=\hat{p}_T^{-7}$ and $D_\pi^q=\exp(-6z)$ are shown on Fig. 22.

The momentum unbalance saturates at $p_{T_t}\approx 10$ GeV/ c around $\sqrt{\langle k_{Tx}^2 \rangle}$ and then starts to decrease. The maximum value depends on the k_T magnitude and on the asymmetry between p_{T_t} and p_{T_a} . Eventually, the unbalance should vanish at high p_{T_t} as a consequence of $\Sigma_Q(\hat{p}_T)$ flattening. The peak magnitude $\sqrt{\langle k_{Tx}^2 \rangle}$ is definitely not a small value. The comparison of $\langle z_t \rangle$ and $\langle z_a \rangle$ found in pythia and derived according to Eq. (41) is shown on Fig. 23. The overall agreement between the pythia simulations and the calculation is excellent. The small deviations may be attributed to the fact that in the pythia simulation, 1 GeV/ c -wide bins were used for trigger and associated particle identification, whereas the calculation was performed for fixed values of p_{T_t} and p_{T_a} . We could certainly extend the integration over fragments' momenta but this would bring only small improvement with the cost of huge CPU demand.

The last missing piece of information needed before solving Eq. (7) is the fragmentation function D_π^q and unsmeared $\Sigma_Q(\hat{p}_T)$. The description of how this knowledge was extracted from the data is a subject of next section.

4.4 Fragmentation function from the combined fit

There are various parameterizations of the fragmentation function used in the literature. Inspired by DIS measurements done at HERA, we found the pure exponential approximation of $D(z)$ to be almost sufficient. However, the exponential form of $D(z)$ does not vanish as $z \rightarrow 1$ and thus may lead to overestimation of the $\langle z_t \rangle$. A wealth of hadron fragmentation also exists from e^+e^- data. The set of data has been analyzed by Kniehl, Kramer, and Potter (KKP) [13] to parameterize the different fragmentation functions. They use a general form

$$D_i^f(z) = N z^\alpha (1-z)^\beta \quad (44)$$

where i is the fragmenting parton and f is the final state hadron. They tabulated N , α , and β for the different parton/hadron combinations. KKP suggested a further parametrization as well

$$D(z) = z^\alpha (1-z)^\beta (1 + \frac{\gamma}{z}) \quad (45)$$

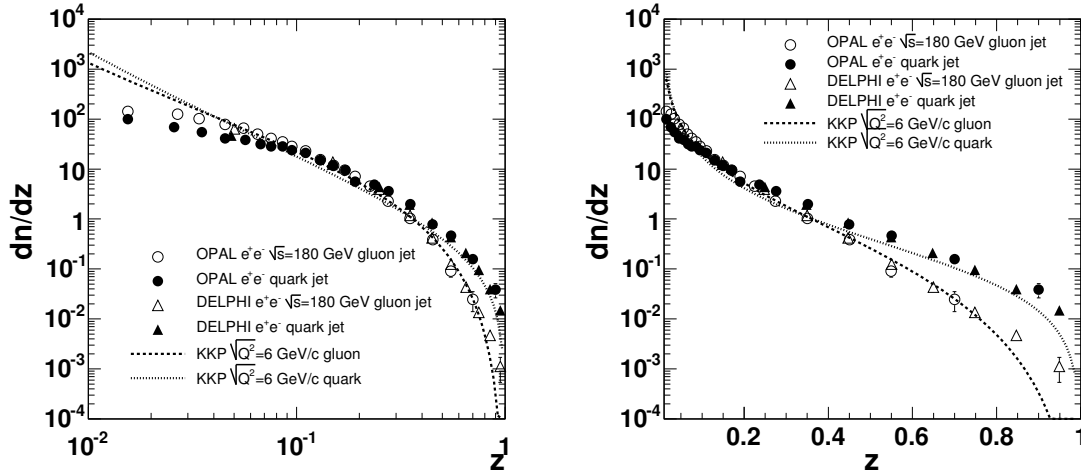


Figure 24: dn/dz distribution measured at LEP for gluon (open symbols) and quark (solid symbols) jets. Left and right plots are identical except the semilog scale used on the x -axis in former case. Dashed and dotted lines represent the NLO KKP fragmentation function for factorization scale $\sqrt{Q^2}=6$ GeV/ c .

We have chosen a variation on Eqn. 45 which gives a better fit to OPAL and DELPHI gluon fragmentation data [14]

$$D(z) = z^\alpha (1-z)^\beta (1+z)^\gamma \quad (46)$$

There is a clear distinction between slopes of dn/dz distributions originating from quark and gluon fragmentation. This is well reproduced by KKP fragmentation function (dashed and dotted lines). The calculation of the KKP fragmentation function was done in NLO with the factorization scale $\sqrt{Q^2}=6$ GeV/c (this value was chosen more or less arbitrarily). The left panel of Fig. 24 indicates increasing deviation between the data and KKP NLO calculated fragmentation function in the low- z region. Since the $\langle z \rangle$ calculation presented in this analysis is dominated by high- z region ($f_Q(\hat{p}_T) \times D_\pi^q$ product is strongly peaked around $z=1$) we do not consider this deviation as significant.

4.4.1 Effective “ k_T smeared” $f_Q(\hat{p}_T)$ and D_π^q distributions

First we have considered the case where we have neglected the influence of k_T on the x_E (see Eq. (4)) and final state parton distribution $f_Q(\hat{p}_T)$. Following definition (15) we denote

$$\begin{aligned}\Sigma_Q(\hat{p}_T) &= \hat{p}_T f_Q(\hat{p}_T) = \frac{d\sigma_{q,\text{unsmeared}}}{d\hat{p}_T} \\ \Sigma'_Q(\hat{p}_{Tt}) &= \hat{p}_{Tt} f'_Q(\hat{p}_{Tt}) = \frac{d\sigma_{q,\text{smeared}}}{d\hat{p}_{Tt}}\end{aligned}\quad (47)$$

We can not, however, eliminate the k_T from the data and thus the extracted parton spectrum has to be viewed as an effective k_T -smeared final state parton spectrum $f'_Q(\hat{p}_{Tt})$. In order to determine the free parameters of the parton \hat{p}_T spectrum, Eq. (60) in App. A.3, and the α , β and γ parameters of the fragmentation function Eq. (46) we performed a simultaneous fit of Eq. (29) to the single inclusive π^0 - p_T distribution [10] and

$$\left. \frac{dn_2}{dx_E} \right|_{p_{Tt}, k_T=0} = \frac{dp_{Ta}}{dx_E} \times \left. \frac{dn_2}{dp_{Ta}} \right|_{p_{Tt}, k_T=0} \simeq p_{Tt} \times \frac{1}{p_{Tt}^2} \int_{x_{Tt}}^1 D_\pi^q(z_t) D_\pi^q\left(\frac{p_{Ta}}{p_{Tt}} z_t\right) \Sigma'_Q\left(\frac{p_{Tt}}{z_t}\right) \frac{dz_t}{z_t} \quad (48)$$

where we used Eq. (6) with $\langle k_T^2 \rangle = 0$ GeV/c and solve $x_E = \sqrt{p_{Ta}^2 - \langle p_{out}^2 \rangle} / p_{Tt}$ for p_{Ta}^2

$$p_{Ta}^2 \simeq \frac{x_E^2 p_{Tt}^2 + \langle j_{Ty}^2 \rangle}{1 - \langle j_{Ty}^2 \rangle / p_{Tt}^2} \simeq x_E^2 p_{Tt}^2 \quad (49)$$

The $\langle k_T^2 \rangle$ magnitude is explicitly neglected and this is also the major advantage of using dn_2/dx_E distributions rather than dn_2/dp_{Ta} because the former are less affected by k_T -smearing.

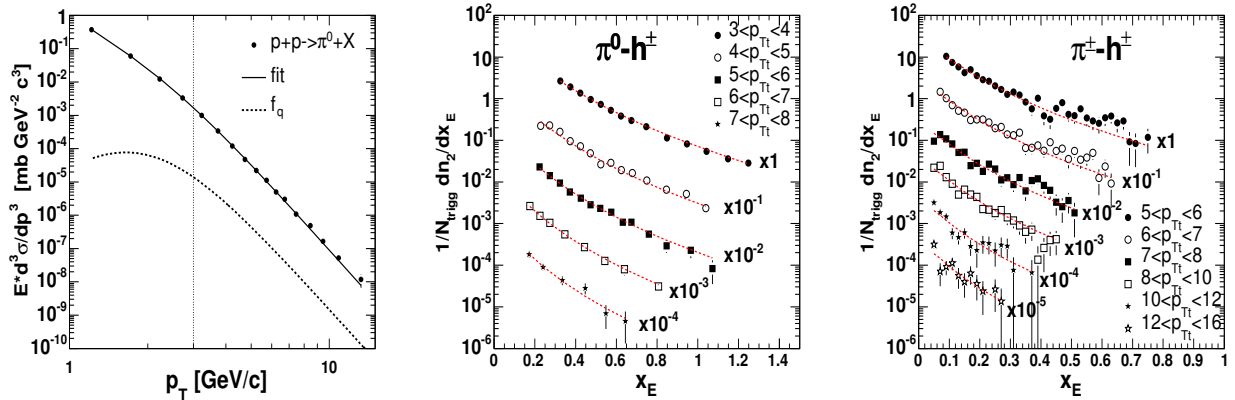


Figure 25: *Left*: The single inclusive π^0 - p_T distribution [10] and fit of Eq. (29) (solid line) and extracted parton \hat{p}_T spectrum parametrized by Eq. (32) (dashed line arbitrarily normalized). The vertical dotted line at 3 GeV indicates the onset of the power-law region. *Middle and Right*: The x_E distributions associated with trigger π^0 and $\pi^\pm - h^\pm$ for various p_{Tt} indicated in the legend. The dashed lines correspond to the fit using Eq. (48).

The absolute normalization of $d\sigma_\pi/p_T dp_T$ and dn_2/dx_E is arbitrary. The simultaneous fitting procedure uses the numerical integration of Eq. (29) and Eq. (48) with four free parameters for n , Eq. (32), and the α , β , γ

parameters of the fragmentation function Eq. (46) and six free parameters - one for $\frac{1}{p_T} \frac{d\sigma_\pi}{dp_T}$ normalization and five for the normalization of the five $dn_2(p_{Tt})/dx_E$ distributions. The combined fit was performed using x_E distributions extracted from π^0 and $\pi^\pm - h^\pm$ associated charged hadron yields (see Fig. 25). Using π^0 as a trigger particle allows us to study a relatively broad range of p_{Tt} between 3-16 GeV/c. We can also explore the correlations associated with high- p_T charged pions detecting by use of RICH detector which allows relatively safe pion identification at high- p_T above the cherenkov threshold of 5 GeV/c. The D_π^q parameters extracted from the combined fit to $\pi^\pm - h^\pm$ data allows us to not only explore the higher p_{Tt} region but it also allows us to estimate the systematic error on D_π^q by comparison of the D_π^q parameters extracted from the $\pi^0 - h^\pm$ and $\pi^\pm - h^\pm$ correlations.

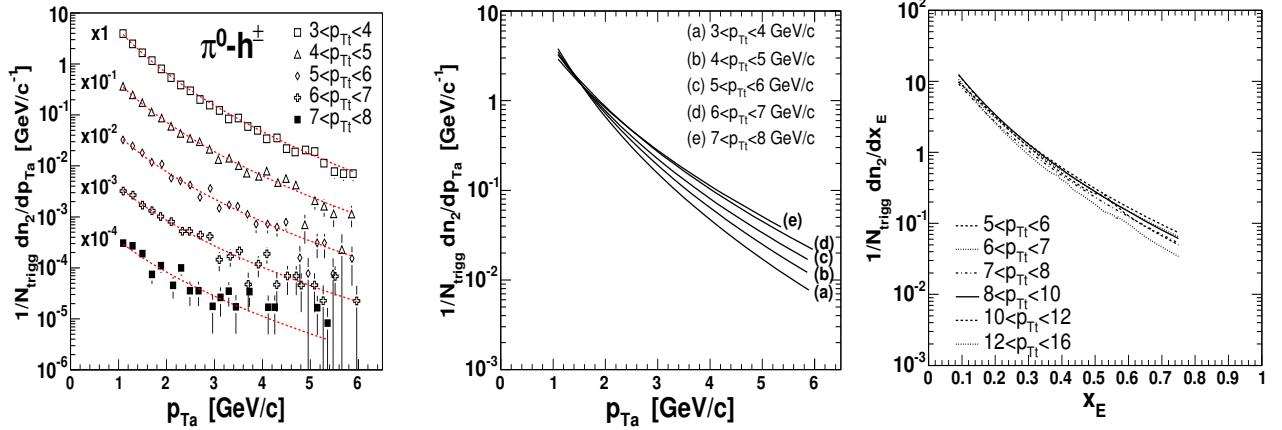


Figure 26: *Left*: The p_{Ta} distributions associated with trigger π^0 for various p_{Tt} indicated in the legend. The dashed lines correspond to the fit of $\left. \frac{dn_2}{dp_{Ta}} \right|_{p_{Tt}, k_T=0}$ (see Eq. (48)). *Middle*: The same fit results from the left panel plotted without the data and the scaling factors. *Right*: The same fit results as shown on the middle panel of Fig. 25 without data and scaling factors.

In order to verify the assumption of Eq. (48), we performed the direct fit of the dn_2/dp_{Ta} distributions as a function of p_{Tt} (see Fig. 26). The fitting procedure is more complicated because the additional integration over k_T needs to be performed. The results obtained using these two approaches are, within the error-bars, the same and together with excellent agreement between D_π^q parameters extracted from $\pi^0 - h^\pm$ and $\pi^\pm - h^\pm$ (see Tab. 3) confirmed the validity of this approach.

The results of the combined fit plotted without multiplicative factors are shown in Fig. 26. Comparison of associated p_{Ta} and x_E distributions demonstrates what has been discussed in section 4.1. The x_E distributions are less sensitive to the variation of p_{Tt} than it is in the case of p_{Ta} distributions. The x_E distributions are less affected by the k_T -smearing and their shapes approximate more closely universal nature of the fragmentation function.

Table 3: Resulting parameters obtained from the simultaneous fit to the single inclusive π^0 distribution and π^0 and π^\pm associated x_E distributions.

	D_π^q according Eq. (46)		D_π^q according Eq. (45)	$D_\pi^q \propto \exp(\gamma z)$
	full π^0 - p_T range, $\lambda=0.1$	π^0 - $p_T > 3$ GeV/c	full π^0 - p_T range $\lambda=0.1$	π^0 - $p_T > 3$ GeV/c
n	8.89 ± 0.11	8.29 ± 0.09	9.13 ± 0.13	8.98 ± 0.09
α	0.80 ± 0.06	0.88 ± 0.05	2.20 ± 0.10	
β	0.07 ± 0.17	0.03 ± 0.19	3.95 ± 0.45	
γ	-11.38 ± 0.59	-10.61 ± 0.21	-0.02 ± 0.004	-11.73 ± 0.14
$\chi^2(\text{DOF})$	378.8(188)	376.3(185)	430.8(188)	773.3(185)

The results of the simultaneous fit to the single inclusive π^0 distribution and to associated x_E distributions (Fig. 25) are presented in Tab. 3. The fit was performed using the Eq. (46) parametrization for D_π^q . In order to check the systematic due to this assumption, the fit with a simple $D_\pi^q \propto \exp(\gamma z)$ parametrization is also performed. The

shapes of these two parameterizations are not very different, however, the exponent of the power law distribution of single inclusive p_T distributions is somewhat larger than the asymptotic power $n \approx 8$ obtained by simple power law fit to the inclusive π^0 distribution above 3 GeV/c. This indicates that the simple exponential parametrization of the fragmentation function is less realistic than Eq. (46). The difference between $\langle z_t \rangle$ parameterizations was used for bracketing the systematic error on k_T .

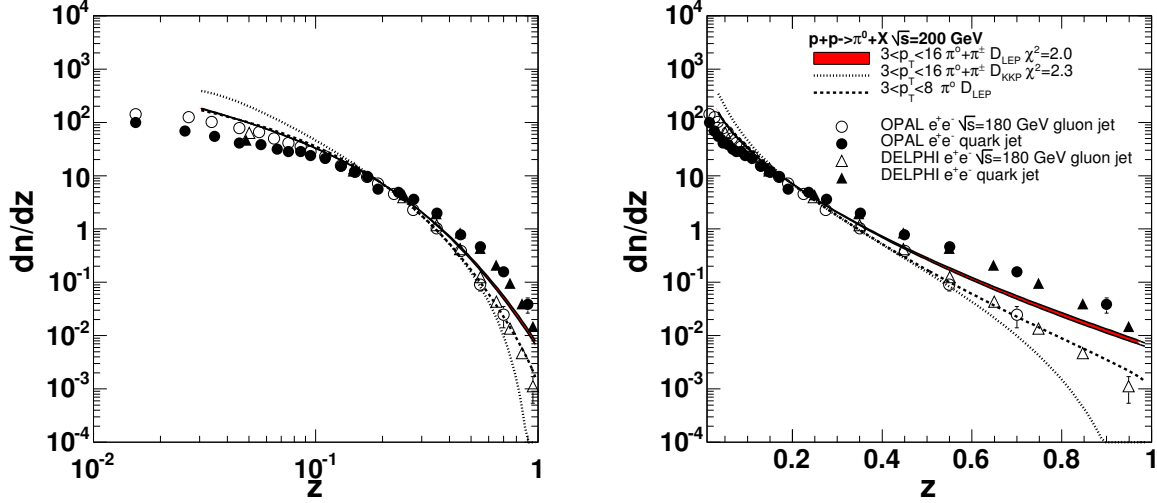


Figure 27: Extracted fragmentation function, normalized at $z=0.2$, parametrized as Eq. (46). Left and right plots are identical except the semilog scale for z -variable. Red band indicates the uncertainty of extracted fit-parameters due to the $p_{T\text{-range}}$ of π^0 inclusive distribution used for fitting. The dashed line represents the fit result to the $\pi^0 - h^\pm$ (lower p_{Tt}) data only. The dotted line represents the fit results when the Eq. (45) parametrization was used. This functional form was not used for further analysis because of the larger χ^2 value obtained from this fit (see Tab. 3). Gluon (open symbols) and quark (solid symbols) jet fragmentation function measured in e^+e^- at $\sqrt{s}=180$ GeV.

The fragmentation function using parameters from Tab. 3 are shown in Fig. 27 together with data from $e^+ + e^-$ collisions measured at $\sqrt{s}=180$ GeV [14] (D_π^q used in this analysis is arbitrarily normalized). The D_π^q parameters extracted from the combined fits to the $\pi^0 - h^\pm$ data only, or to the $\pi^0 - h^\pm$ and $\pi^\pm - h^\pm$ combined data show interesting p_{Tt} dependence. The fit to lower p_{Tt} $\pi^0 - h^\pm$ data results in steeper D_π^q more close to the e^+e^- gluon fragmentation function.

However, this way of parameterization of $\Sigma'_Q(\hat{p}_{Tt})$ does not serve any information about the k_T smearing, so we do not use this results on $\Sigma'_Q(\hat{p}_{Tt})$ and D_π^q parameters for further analysis. For the final analysis we used $\Sigma_Q(\hat{p}_T)$ smeared by Gaussian approximation for the k_T as described in the following section.

4.4.2 Unsmearred $f_Q(\hat{p}_T)$ and D_π^q distributions

In section 3 and appendix A.4.1 and A.4.2 we have discussed the effect of k_T smearing and we argued that the k_T smearing affects substantially the parton distribution function. Therefore it is obvious that the more correct way of extracting the $f_Q(\hat{p}_T)$ and D_π^q distributions is to fit a unsmearred $f_Q(\hat{p}_T)$ (or $\Sigma_Q(\hat{p}_T)$) distribution and perform the smearing during the fitting procedure. When we did that we have realized that the best parameterization for the unsmearred distribution is a modified power law distribution

$$f_q(\hat{p}_T) \propto \hat{p}_T^{-(n_1+n_2 \cdot \log(\hat{p}_T/100))} \quad . \quad (50)$$

with the “running exponent” and sharp cut off around 1 GeV/c. We have repeated the combined fit with smeared parton distribution

$$\left. \frac{dn_2}{dx_E} \right|_{p_{Tt}, k_T > 0} \simeq p_{Tt} \times \frac{1}{p_{Tt}^2} \int_{x_{Tt}}^1 D_\pi^q(z_t) D_\pi^q\left(\frac{p_{Ta}}{p_{Tt}} z_t\right) \int_{-\infty}^{\infty} \Sigma_Q(\hat{p}_T) \exp\left(-\frac{\left(\frac{p_{Tt}}{z_t} - \hat{p}_T\right)^2}{\langle k_{Tx}^2 \rangle}\right) d\hat{p}_T \frac{dz_t}{z_t} \quad (51)$$

We used Eq. (51) with parameterization Eq. (62) and performed the combined fit with fixed value of $\langle k_T^2 \rangle$. The fit results for $\sqrt{\langle k_T^2 \rangle} = 2.2$ GeV/c are shown on Fig. 28. For the unsmeared distribution the power law distribution gives better agreement with data than the Eq. (60) parameterization used an extraction of effective $f_Q(\hat{p}_T)$.

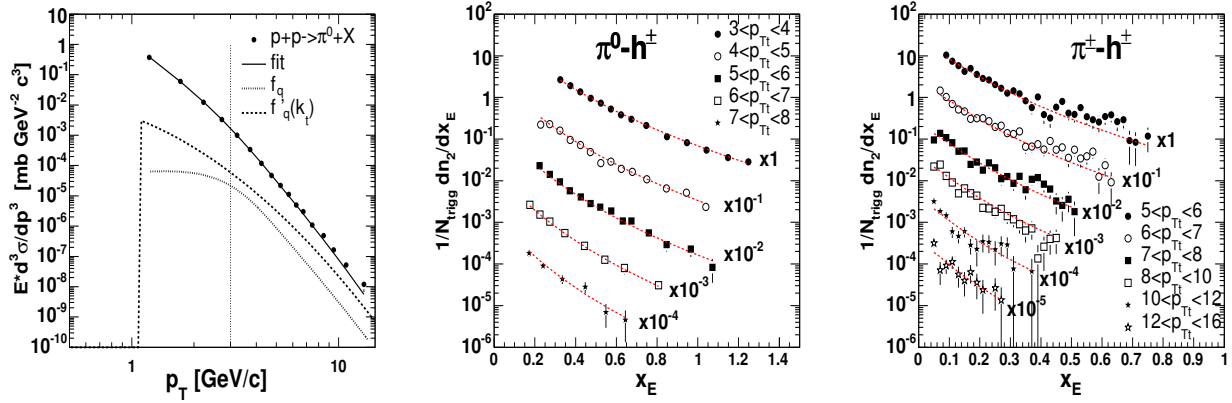


Figure 28: *Left:* The single inclusive π^0 - p_T distribution [10] and fit of Eq. (51) (solid line) and extracted parton spectrum parametrized by Eq. (62) (dashed line arbitrarily normalized). The vertical dotted line at 3 GeV indicates the onset of the power-law region. *Middle and Right:* The x_E distributions associated with trigger π^0 and $\pi^\pm - h^\pm$ for various p_{T_t} indicated in the legend. The dashed lines correspond to the combined fit using Eq. (51).

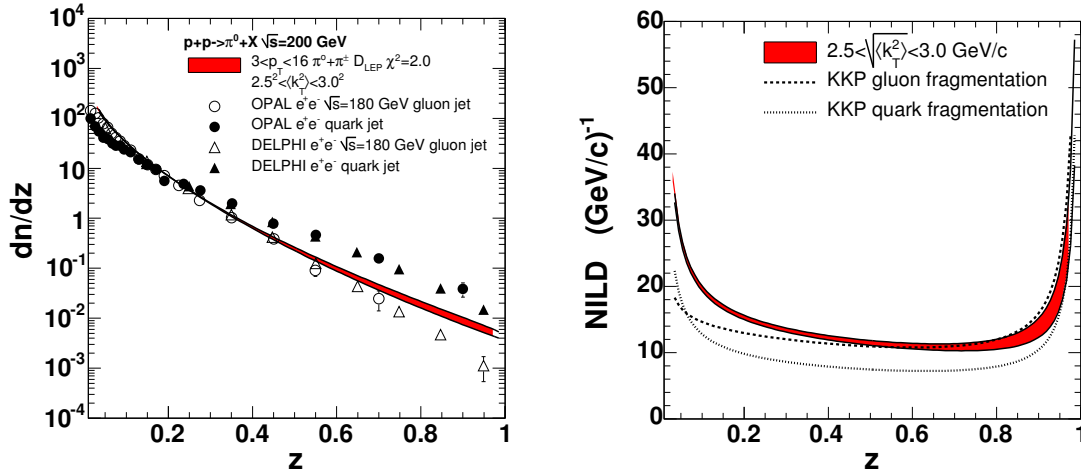


Figure 29: *Left:* Extracted fragmentation function, normalized at $z=0.2$, parametrized as Eq. (46) from the combined fit to π^0 inclusive and associated x_E distributions using formula 51. Red band indicates the parameter range corresponding to the k_T variation between 2.5 and 3 GeV/c. Gluon (open symbols) and quark (solid symbols) jet fragmentation function measured in e^+e^- at $\sqrt{s}=180$ GeV. *Right:* Negative Inverse Logarithmic Derivative of the fragmentation function extracted from the combined fit with $2.5 < \sqrt{\langle k_T^2 \rangle} < 3.0$ GeV/c. The same analysis of the KKP parameterization of the gluon (dashed line) and quark (dotted line) fragmentation function.

Comparing the fragmentation function extracted from the combined fit using k_T smeared or unsmeared distribution one can conclude that the exact shape of D_π^q is more or less sensitive to the exact way of $f_Q(\hat{p}_T)$ parameterization. The latter case is, however, more realistic. We compare the Negative Inverse Logarithmic Derivative

(NILD, right panel of Fig. 29) with KKP parameterization of the gluon and quark jet fragmentation function.

Parameters of $f_Q(\hat{p}_T)$ distribution (see Eq. (62)) and fragmentation function (see Eq. (46)) extracted from the combined fit are summarized in Tab. 4.

Table 4: $f_Q(\hat{p}_T)$ and D_π^q parameters from the combined fit (see Eq. (62) and Eq. (46))

n1	=	8.00 ± 0.23
n2	=	1.19 ± 0.10
α	=	0.59 ± 0.08
β	=	0.09 ± 0.2
γ	=	12.96 ± 0.88

5 $\langle k_T \rangle$ results

The $\hat{x}_h^{-1} \langle z_t \rangle \sqrt{\langle k_T^2 \rangle}$ extracted according Eq. (7) for varying p_{Tt} and p_{Ta} are shown on Fig. 10. In order to extract a $\sqrt{\langle k_T^2 \rangle}$ values we have solved

$$x_h^{-1} \sqrt{\langle p_{out}^2 \rangle - \langle j_{Ty}^2 \rangle} (x_h^2 + 1) - \hat{x}_h^{-1} \langle k_T, x_h \rangle \langle z_t(k_T, x_h) \rangle \sqrt{\langle k_T^2 \rangle} = 0 \quad (52)$$

for $\sqrt{\langle k_T^2 \rangle}$ where the $\langle z_t \rangle$ and $\hat{x}_h = \langle \hat{p}_{Ta} \rangle / \langle \hat{p}_{Tt} \rangle$ are evaluated according Eq. (41) and Eq. (43) respectively. $f_Q(\hat{p}_T)$ and D_π^q parameterizations summarized in Tab. 4 were used. Resulting $\sqrt{\langle k_T^2 \rangle}$ values for $3 < p_{Tt} < 4$ GeV/c and $5 < p_{Tt} < 10$ GeV/c as a function of p_{Ta} are shown on the left panel of Fig. 30. The colored rectangles indicate the systematic errors. The main contributions come from the uncertainty of the p_{out} extraction in $1.4 < p_{Ta} < 5.0$ GeV/c bin (see Fig. 35 in appendix A.2), from the systematic uncertainty given by parameterization of $f_Q(\hat{p}_T)$ (see appendix A.3) and from the assumptions discussed in section 4.4 (*e.g.* Eq. (48)).

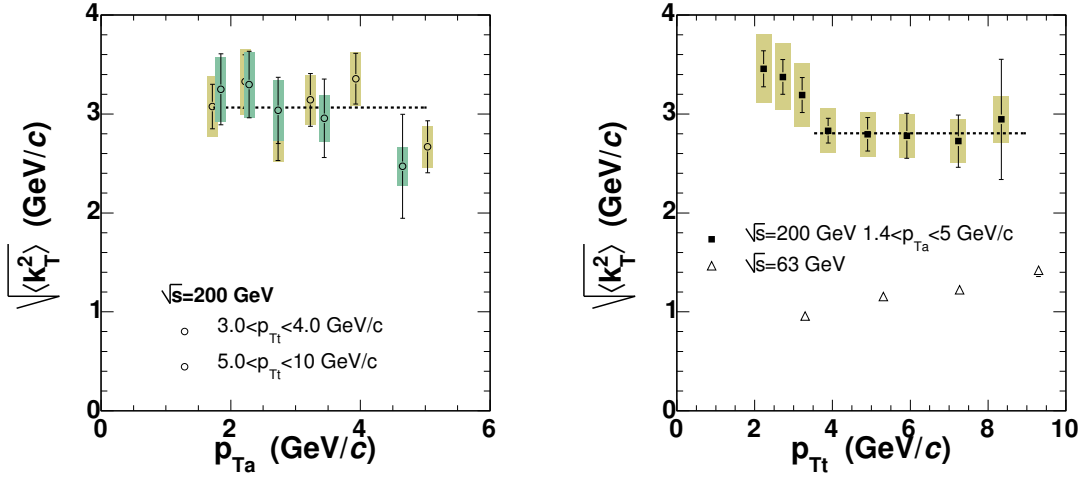


Figure 30: $\sqrt{\langle k_T^2 \rangle}$ as solution of Eq. (52) for $3 < p_{Tt} < 4$ GeV/c and $5 < p_{Tt} < 10$ GeV/c as a function of p_{Ta} (left panel) and for $1.4 < p_{Ta} < 5$ GeV/c as a function of p_{Tt} (right panel). The colored rectangles indicate the systematic error. The CCOR measurement at $\sqrt{s}=62.4$ GeV [4] (empty triangles on the right panel).

Table 5: The $\sqrt{\langle k_T^2 \rangle}$ values shown on Fig. 30. All units in rad and GeV/c.

1.4 < p_{Ta} < 5.0		3 < p_{Tt} < 4		5 < p_{Tt} < 10	
p_{Tt}	$\sqrt{\langle k_T^2 \rangle}$	p_{Ta}	$\sqrt{\langle k_T^2 \rangle}$	p_{Ta}	$\sqrt{\langle k_T^2 \rangle}$
2.23	3.456 ± 0.183	1.72	3.075 ± 0.225	1.85	3.249 ± 0.360
2.72	3.374 ± 0.176	2.22	3.328 ± 0.271	2.28	3.297 ± 0.337
3.22	3.191 ± 0.177	2.73	2.798 ± 0.268	2.73	3.037 ± 0.334
3.89	2.831 ± 0.126	3.23	3.143 ± 0.266	3.44	2.956 ± 0.396
4.90	2.795 ± 0.170	3.93	3.357 ± 0.256	4.65	2.472 ± 0.526
5.91	2.780 ± 0.228	5.04	2.669 ± 0.264		
7.24	2.726 ± 0.263				
8.34	2.946 ± 0.608				

The p_{Tt} below 3 GeV/c are smaller than the $\sqrt{\langle k_T^2 \rangle}$ and these should be eliminated from the analysis. When we eliminate these low p_{Tt} points we extracted the average value

$$\sqrt{\langle k_T^2 \rangle} = 2.81 \pm 0.10(\text{stat})_{-0.27}^{+0.19}(\text{sys}) \text{ GeV/c} \quad (53)$$

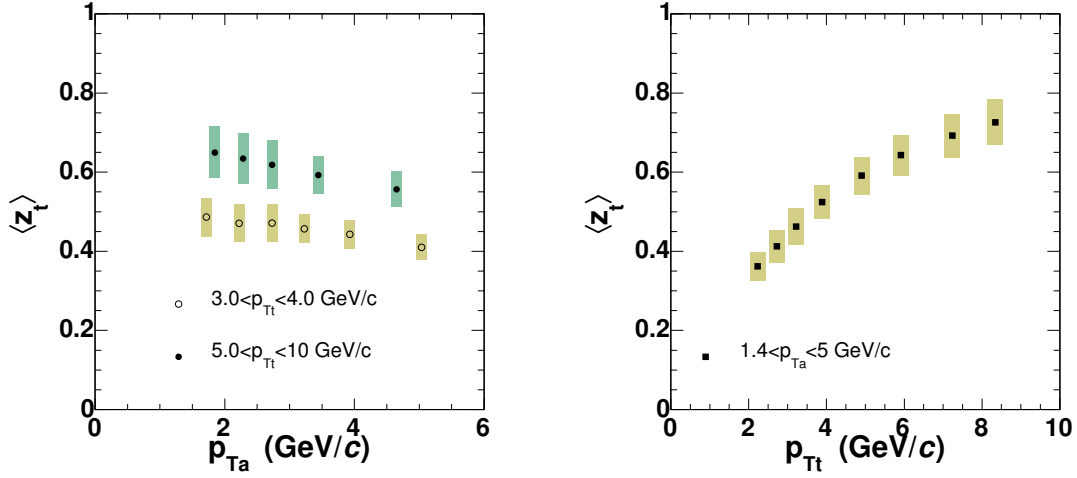


Figure 31: The $\langle z_t \rangle$ values as solution of Eq. (41) for $3 < p_{Tt} < 4$ GeV/c and $5 < p_{Tt} < 10$ GeV/c as a function of p_{Ta} (left panel) and for $1.4 < p_{Ta} < 5$ GeV/c as a function of p_{Tt} (right panel).

Table 6: The $\langle z_t \rangle$ and \hat{x}_h values (see definition 5) values shown on Fig. 31 and Fig. 32. All units in rad and GeV/c.

$1.4 < p_{Ta} < 5.0$			$3 < p_{Tt} < 4$			$5 < p_{Tt} < 10$		
p_{Tt}	$\langle z_t \rangle$	\hat{x}_h	p_{Ta}	$\langle z_t \rangle$	\hat{x}_h	p_{Ta}	$\langle z_t \rangle$	\hat{x}_h
2.23	0.362 ± 0.005	0.98 ± 0.01	1.72	0.486 ± 0.009	0.846 ± 0.014	1.85	0.650 ± 0.009	0.78 ± 0.04
2.72	0.413 ± 0.005	0.93 ± 0.01	2.22	0.471 ± 0.007	0.899 ± 0.011	2.28	0.634 ± 0.006	0.82 ± 0.03
3.22	0.462 ± 0.005	0.90 ± 0.01	2.73	0.471 ± 0.003	0.960 ± 0.005	2.73	0.619 ± 0.003	0.88 ± 0.02
3.89	0.525 ± 0.003	0.89 ± 0.01	3.23	0.457 ± 0.001	0.990 ± 0.001	3.44	0.593 ± 0.003	0.93 ± 0.02
4.90	0.591 ± 0.003	0.88 ± 0.01	3.93	0.443 ± 0.001	1.032 ± 0.004	4.65	0.557 ± 0.006	0.98 ± 0.01
5.91	0.643 ± 0.004	0.87 ± 0.02	5.04	0.410 ± 0.003	1.051 ± 0.009			
7.24	0.692 ± 0.003	0.87 ± 0.02						
8.34	0.726 ± 0.004	0.84 ± 0.05						

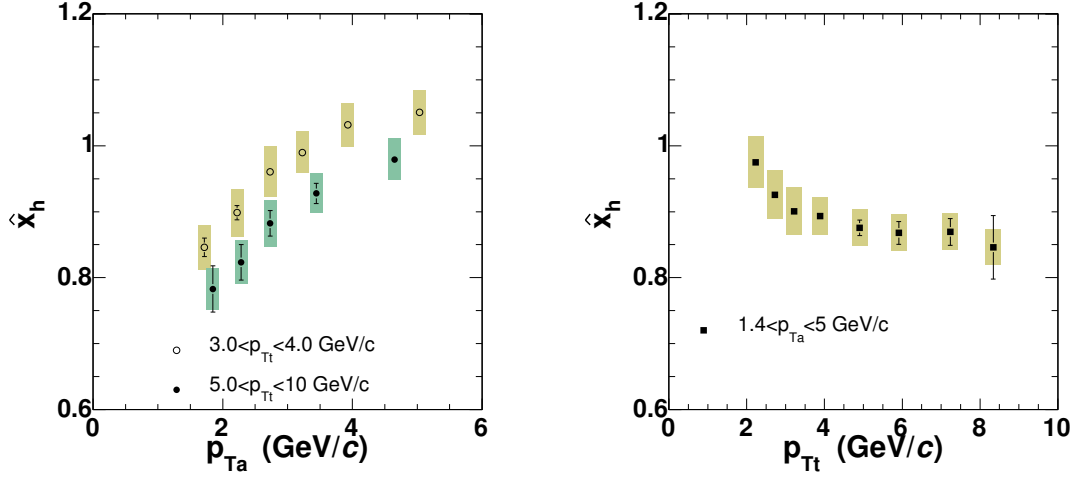


Figure 32: The \hat{x}_h values (see definition 5) as solution of Eq. (43) for $3 < p_{Tt} < 4$ GeV/c and $5 < p_{Tt} < 10$ GeV/c as a function of p_{Ta} (left panel) and for $1.4 < p_{Ta} < 5$ GeV/c as a function of p_{Tt} .

$$\langle \hat{p}_n \rangle \equiv \langle p_T \rangle_{pair} = \sqrt{\frac{\pi}{2}} \sqrt{\langle k_T^2 \rangle} = 3.51 \pm 0.13^{+0.23}_{-0.34}(\text{sys}) \text{ GeV}/c \quad (54)$$

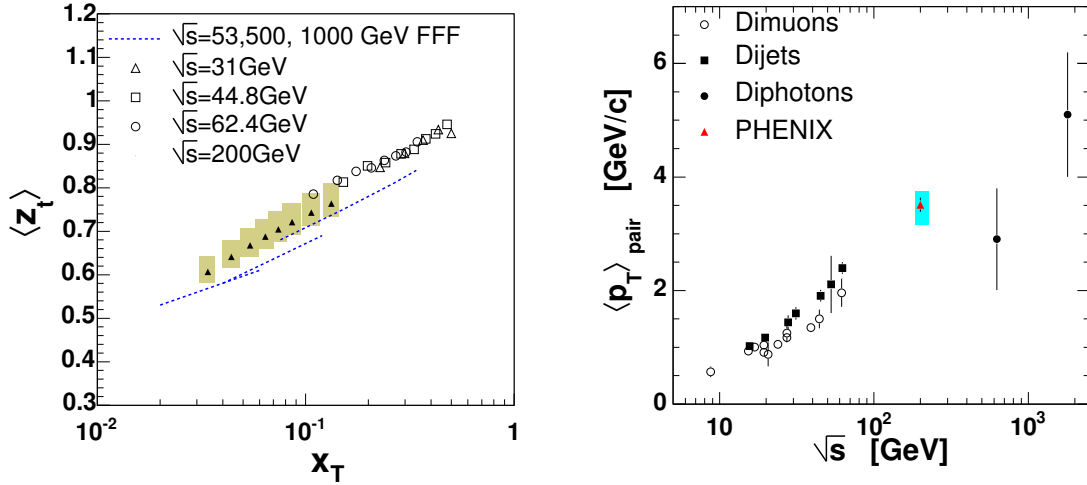


Figure 33: *Left*: $\langle z_t \rangle$ from this analysis together with the *FFF* calculation [16] and CCOR measurements [17]. Colored rectangles indicate the systematic errors. *Right*: Compilation of mean pair p_T measurements [15] and comparisons to the $\langle p_T \rangle_{pair} = \sqrt{\frac{\pi}{2}} \sqrt{\langle k_T^2 \rangle}$ measured in this analysis.

6 Summary

We have made the first measurement of jet j_T and k_T for $p + p$ collisions at $\sqrt{s} = 200$ GeV using the method of two-particle correlations. Analysis of the angular widths of the near-side peak in the correlation function has determined that the jet fragmentation transverse momentum j_T is constant with trigger particle p_{T_t} with a value of

$$\sqrt{\langle j_T^2 \rangle} = 0.59 \pm 0.01 \text{ GeV}/c$$

is comparable with previous lower \sqrt{s} measurements. The width of the away-side peak is shown to be a measure of the convolution of j_T with the jet momentum fraction z , and the partonic transverse momentum k_T . The $\langle z_t \rangle$ is determined through a combined analysis of the measured π^0 inclusive and associated spectra by determining the jet fragmentation function. The derived fragmentation function is indicative of gluonic jet domination in the explored p_T range. The final extracted values of k_T are then determined to be also independent of the transverse momentum of the trigger particle, with values of

$$\sqrt{\langle k_T^2 \rangle} = 2.81 \pm 0.10(\text{stat})_{-0.27}^{+0.19}(\text{sys}) \text{ GeV}/c$$

We have found some kinematical effect which were not taken into account in previous analysis [1]

- x_E distribution reflects also $\langle z_a \rangle$ and not only $\langle z_t \rangle$ (see Eq. (33)).
- Trigger associated p_{T_a} or x_E distributions reflect the fragmentation function in more complicated way we originally thought. When we change the associated p_{T_a} (or x_E) the $\langle z_t \rangle$ is changed even in the case of fixed trigger momentum p_{T_t} .

All software used for this analysis is available in CVS repository

<http://www.phenix.bnl.gov/viewcvs/offline/analysis/jtkt/>

A Appendix

A.1 First and second moments of normally distributed quantities

Let x be a 1D variable with normal (Gaussian) distribution and $r = \sqrt{x^2 + y^2}$ is a 2D variable with x and y of normal distribution then the following relations can be easily derived

$$\begin{aligned} \langle x \rangle &= 0 & \langle r \rangle &= \sqrt{\frac{\pi}{2}} \sigma_1 \\ \langle |x| \rangle &= \sqrt{\frac{2}{\pi}} \sigma_1 & \langle |r| \rangle &= \langle r \rangle \\ \langle x^2 \rangle &= \sigma_1^2 & \langle r^2 \rangle &= 2\sigma_1^2 \equiv \sigma_2^2 \end{aligned}$$

Both \vec{j}_T and \vec{k}_T are two dimensional vectors. We assume Gaussian distributed x and y components and thus the mean value $\langle k_{Tx} \rangle$ and $\langle k_{Ty} \rangle$ is equal to zero. The non-zero moments of 2D Gaussian distribution are *e.g.* the root mean squares $\sqrt{\langle j_T^2 \rangle}$, $\sqrt{\langle k_T^2 \rangle}$ or the mean absolute values of the \vec{j}_T , \vec{k}_T projections into the perpendicular plane to the jet axes $\langle |j_{Ty}| \rangle$ and $\langle |k_{Ty}| \rangle$. Note that there are a trivial correspondences

$$\sqrt{\langle k_T^2 \rangle} = \frac{2}{\sqrt{\pi}} \langle k_T \rangle = \sqrt{\pi} \langle |k_{Ty}| \rangle \quad (55)$$

A.2 The correct way to analyze the azimuthal correlation function.

Construction and fitting of the two-particle azimuthal correlation function is discussed in section 1.3. Traditionally the correlation function is fitted by two Gaussian functions - one for intra-jet correlation (near peak) and one for the inter-jet correlations (away-side peak). From the extracted variances of the Gaussian functions the j_T and p_{out} magnitudes are extracted.

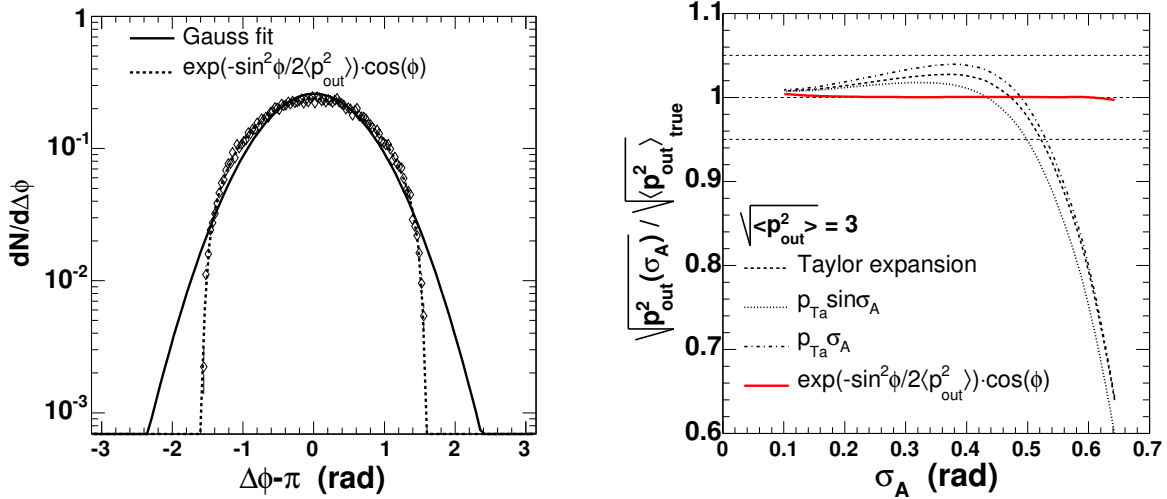


Figure 34: *Left:* Simulated away-side $dN/d\Delta\phi$ distribution fitted by the Gaussian (solid line) and Eq. (57). *Right:* The relative error on p_{out} determination from the azimuthal correlation function based on the Taylor expansion of $\langle \sin \Delta\phi^2 \rangle$ (dashed line), with an assumption of $\sqrt{\langle p_{\text{out}}^2 \rangle} = p_{Ta} \sin \sigma_A$ (dotted line) and $\sqrt{\langle p_{\text{out}}^2 \rangle} = p_{Ta} \sigma_A$ (dotted-dashed line). The solid red line corresponds to $\sqrt{\langle p_{\text{out}}^2 \rangle}$ from Eq. (57).

There is, however, a fundamental problem with this approach. The p_{out} -vector defined in Eq. (2) is equal to $p_{Ta} \sin \Delta\phi$ event by event. However, we measure the width of the correlation peak and this corresponds to $\sqrt{\langle \Delta\phi^2 \rangle} = \sigma_A$. The relation $\sqrt{\langle p_{\text{out}}^2 \rangle} \approx p_{Ta} \sin \sigma_A$ is not good approximation for $\sigma_A > 0.4$ rad (see right panel of Fig. 34). The assumption that the away-side correlation has a Gaussian shape is also good only for small values of σ_A (see left panel of Fig. 34).

One way of relating $\sqrt{\langle p_{\text{out}}^2 \rangle}$ and σ_A was proposed *e.g.* by Peter Levai, Jiangyong and others and used in several other analyzes [2]. Since $\sqrt{\langle p_{\text{out}}^2 \rangle} = p_{T_a} \sqrt{\langle \sin^2 \Delta\phi \rangle}$ one possibility how to relate p_{out} and σ_A is to expand

$$\langle \sin^2 \Delta\phi \rangle = \left\langle \Delta\phi^2 - \frac{1}{3}\Delta\phi^4 + \frac{2}{45}\Delta\phi^6 - \frac{1}{315}\Delta\phi^8 + \dots \right\rangle = \sigma_A^2 - \sigma_A^4 + \frac{2}{3}\sigma_A^6 - \frac{1}{3}\sigma_A^8 + \dots \quad (56)$$

where we assumed the Gaussian distribution of $\Delta\phi$. The comparison of $p_{T_a} \cdot (\sigma_A^2 - \sigma_A^4 + \frac{2}{3}\sigma_A^6 \dots)$ with true p_{out} magnitude (simple monte carlo) for various σ_A values is shown on Fig. 34. It is obvious that there is only a little difference between $\sqrt{\langle p_{\text{out}}^2 \rangle} = p_{T_a} \sin\sigma_A$, $\sqrt{\langle p_{\text{out}}^2 \rangle} = p_{T_a} \sigma_A$ and the Taylor series. In the region where $\sigma_A > 0.4$ rad, all approximations seems to be equally bad.

However, p_{out} , the only quantity with a truly Gaussian distribution (if we neglect the radiative corrections responsible for non-Gaussian tails in p_{out} distribution which are anyway not relevant for the k_T analysis) can be directly extracted from the correlation function. With the assumption of Gaussian distribution in p_{out} , we can write the away-side $\Delta\phi$ -distribution (normalized to unity) as

$$\left. \frac{dN_{\text{away}}}{d\Delta\phi} \right|_{\pi/2} = \frac{dN}{dp_{\text{out}}} \frac{dp_{\text{out}}}{d\Delta\phi} = \frac{-p_{T_a} \cos \Delta\phi}{\sqrt{2\pi \langle p_{\text{out}}^2 \rangle} \text{Erf}\left(\frac{\sqrt{2}p_{T_a}}{\sqrt{\langle p_{\text{out}}^2 \rangle}}\right)} \exp\left(-\frac{p_{T_a}^2 \sin^2 \Delta\phi}{2 \langle p_{\text{out}}^2 \rangle}\right) \quad (57)$$

This is the correct way of extracting a dimensional quantity from the azimuthal correlation function in the case of narrow associated bin. Similar line of arguments can be drawn also in the case of near peak. There is, however, one more complication in the case of broad associated p_{T_a} bin. In this analysis we have used $1.4 < p_{T_a} < 5.0$ bin and in this case Eq. (57) has to be integrated over p_{T_a} providing the the knowledge of the dn/dp_{T_a} shape. We performed the same simulation as described in the previous text but the p_{T_a} was simulated according the real data distribution (left panel of Fig. 35). The error due to the finite size of p_{T_a} bin is smaller than 10% (see Fig. 35) so we do not consider the p_{T_a} “smearing” important for this analysis.

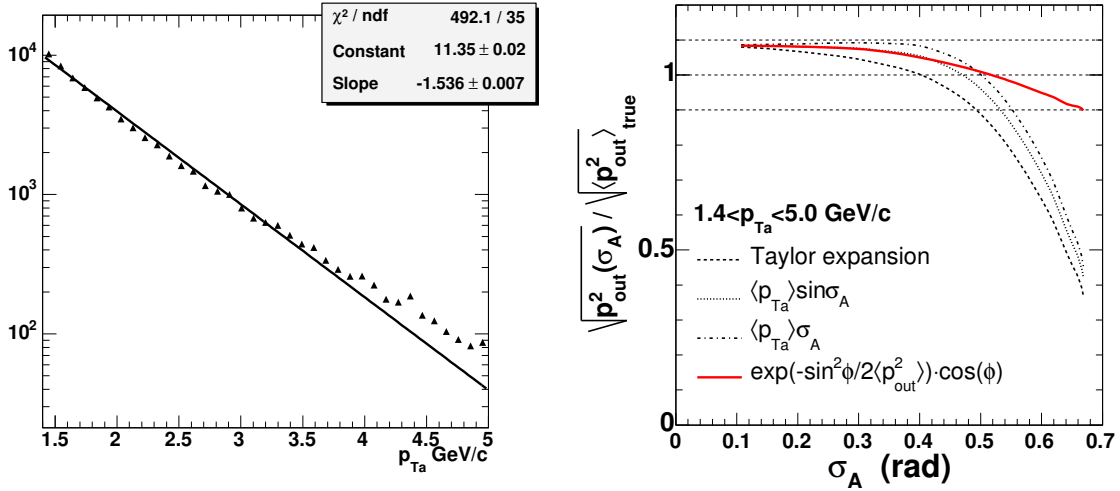


Figure 35: Left: dN/dp_{T_a} distribution for $4 < p_{T_t} < 5$ GeV/c trigger bin. Right: The relative error on p_{out} determination from the azimuthal correlation function, constructed with $1.4 < p_{T_a} < 5.0$ GeV/c, based on the Taylor expansion of $\langle \sin^2 \Delta\phi \rangle$ (dashed line), with an assumption of $\sqrt{\langle p_{\text{out}}^2 \rangle} = \langle p_{T_a} \rangle \sin \sigma_A$ (dotted line) and $\sqrt{\langle p_{\text{out}}^2 \rangle} = \langle p_{T_a} \rangle \sigma_A$ (dotted-dashed line). The solid red line corresponds to $\sqrt{\langle p_{\text{out}}^2 \rangle}$ from Eq. (57).

The trigger and associated j_T -vectors form a vector perpendicular to the sum of $\vec{p}_{T_t} + \vec{p}_{T_a}$ and $j_{T_y}(1+x_{\text{h}}^2)$ distribution has a Gaussian shape. The near-side distribution can be written as

$$\frac{dN_{\text{near}}}{d\Delta\phi} = \exp\left(-\frac{p_{T_a}^2 \sin^2(\phi)(p_{T_t}^2 + p_{T_a}^2 + 2p_{T_a}p_{T_t} \cos(\phi))}{2(p_{T_t} + p_{T_a} \cos(\phi))^2 \langle j_{T_y}^2 \rangle}\right) \cdot \mathcal{J} \quad (58)$$

where

$$\mathcal{J} = \frac{4p_{Ta}^2 + 6p_{Ta}p_{Tt}^2 + (11p_{Ta}^2 + 4p_{Tt}^3)\cos(\phi) + 6p_{Ta}p_{Tt}^2\cos(2\phi) + p_{Ta}^2p_{Tt}\cos(3\phi)}{4(p_{Tt} + p_{Ta}\cos(\phi))^2\sqrt{p_{Ta}^2 + p_{Tt}^2} + 2p_{Ta}p_{Tt}\cos(\phi)} \quad (59)$$

This expression is more complicated and an error on j_{Ty} from the approximation Eq. (1) is around 2-3% for the j_{Ty} values about 0.5 GeV/c, which is negligible.

A.3 $f_Q(\hat{p}_T)$ parameterizations for the case of $\hat{p}_T \rightarrow 0$ and $\hat{p}_T \rightarrow \sqrt{s}/2$

For the case of smeared final state parton distribution function used in this analysis we explored a modified power law distribution

$$f_q(\hat{p}_T) \propto \frac{1}{(M_0^2 + \hat{p}_T^2)^{n/2}} \quad M_0 = \frac{m_0}{\ln(\hat{p}_T/\lambda)} \quad (60)$$

where m_0 , n and λ are free parameters. This functional form converges quickly to the power law shape for $\hat{p}_T \gg M_0$, diminishes at low \hat{p}_T due to the presence of M_0 term in the denominator.

In order to ensure the $f_q(\hat{p}_T)$ diminishes also at high \hat{p}_T we explored

$$f_q(\hat{p}_T) \propto \frac{(1 - (2\hat{p}_T/\sqrt{s})^2)^8}{(M_0^2 + \hat{p}_T^2)^{n/2}}. \quad (61)$$

The M_0 parameter has the same meaning as in Eq. (60) and the additional term in the denominator ensures that $f_Q(\hat{p}_T)$ vanishes at the end of the phase space [12]. However, as discussed in App. A.5, this analysis is sensitive only to $z \approx 1$ region of the fragmentation function and hence the contribution from the high \hat{p}_T region is not important.

In section 3 and appendix A.4.1 and A.4.2 the effect of k_T smearing was discussed. In order to calculate the conditional yield (see section 4.3 for details) the unsmeared $\Sigma_Q(\hat{p}_T)$ distribution (see Eq. (15)) has to be evaluated. We have realized that the best parameterization for the unsmeared distribution is just a pure power law, or slightly modified power law distribution

$$f_q(\hat{p}_T) \propto \hat{p}_T^{-(n_1 + n_2 \log(\hat{p}_T/100))}. \quad (62)$$

with the “running exponent” and sharp cut off around 1 GeV/c.

A.4 Resolution Smearing of a Momentum Spectrum

The most frequently used smearing corresponds to the smearing of single dimensional quantity, e.g. energy, measured with a device of finite resolution. If the distribution to be smeared has an exponential form the folding integral has an analytical solution. Suppose that x_o is a quantity to be measured which is distributed with a steeply falling exponential distribution:

$$d\mathcal{P}(x_o) = f(x_o) dx_o = e^{-bx_o} dx_o \quad (63)$$

Further suppose that the true quantity x_o is measured with a Gaussian resolution function so that the result of the measurement is the quantity x , where

$$\mathcal{R}(x, x_o) dx = \text{Prob}(x)|_{x_o} dx = \frac{1}{\sqrt{2\pi\sigma^2}} \exp\left(-\frac{(x - x_o)^2}{2\sigma^2}\right) dx$$

The result for the measured spectrum is simply

$$f(x) dx = \int_{x_o=x-\infty}^{x_o=x+\infty} dx_o f(x_o) \text{Prob}(x)|_{x_o} dx$$

$$f(x) = \frac{1}{\sqrt{2\pi\sigma^2}} \int dx_o \exp(-bx_o) \exp\left(-\frac{(x - x_o)^2}{2\sigma^2}\right)$$

Complete the square:

$$f(x) = e^{-bx} e^{\frac{b^2\sigma^2}{2}} \times \frac{1}{\sqrt{2\pi\sigma^2}} \int_{x_o=x-\infty}^{x_o=x+\infty} dx_o \exp\left(-\frac{(x - b\sigma^2 - x_o)^2}{2\sigma^2}\right)$$

The result, since the Gaussian is normalized over $(-\infty, +\infty)$, is simply

$$f(x) = e^{\frac{b^2\sigma^2}{2}} \times e^{-bx} = e^{-b(x-b\sigma^2/2)}. \quad (64)$$

The slopes before and after smearing are identical.

A.4.1 1D smearing.

1D folding would be a good approximation for the k_T smearing only when the k_T -vector is collinear with parton momenta. This assumption is not acceptable in the momentum regime where the magnitude of k_T is comparable to \hat{p}_T . In the $\hat{p}_T \gg k_T$ region, the transverse component k_{Ty} can be neglected and the 1D smearing may be used. In the high- \hat{p}_T region, however, parton distribution flattens and the smearing has a smaller effect.

The k_T -smearing “stretches” the $\langle \hat{p}_T \rangle$ up. It means that the smeared parton sample at given \hat{p}_{Tt} is dominated by contributions from smaller momenta with the \vec{k}_T vector aligned with the direction of the parton momentum. This is a consequence of the folding of steeply falling spectra. The smearing can be quantified by the ratio of smeared/unsmeared distributions denoted according [15] as $K(\hat{p}_T)$ and by the mean shift of transverse momentum before and after smearing

$$\Delta \hat{p}_T = \hat{p}_{Tt} - \langle \hat{p}_T \rangle = \hat{p}_{Tt} - \frac{\int_0^\infty \hat{p}_T \cdot \Sigma_Q(\hat{p}_T) \cdot \exp\left(-\frac{(\hat{p}_T - \hat{p}_{Tt})^2}{2\sigma_{sm}^2}\right) d\hat{p}_T}{\int_0^\infty \Sigma_Q(\hat{p}_T) \cdot \exp\left(-\frac{(\hat{p}_T - \hat{p}_{Tt})^2}{2\sigma_{sm}^2}\right) d\hat{p}_T} \quad (65)$$

As discussed by Mike in [8] and in A.4, in case of an exponential function $\Sigma_Q(\hat{p}_T) = \exp(-\alpha \hat{p}_T)$ there is an analytical solution $e^{-\alpha x} \otimes g(x, \sigma) = e^{-\alpha y} \cdot e^{\frac{\alpha^2 \sigma^2}{2}}$ and thus

$$\Delta p_{T=\hat{p}_{Tt}} - \frac{\sqrt{2\pi\sigma_{sm}^2}(\hat{p}_{Tt} - \alpha\sigma_{sm}^2)}{\sqrt{2\pi\sigma_{sm}^2}} = \alpha\sigma_{sm}^2 \quad \text{and} \quad K(x) = \exp \frac{\alpha^2 \sigma^2}{2} = \text{const.} \quad (66)$$

The Δp_T -shift according Eq. (65) is by factor of 2 larger than the shift calculated according the definition in [8]. However, we believe that definition Eq. (65) is more appropriate. The K factor is, in the case of exponential function, independent of p_T .

In case of a power law spectra there is no analytical solution. The \hat{p}_T -shift depends on the local slope which implies that the smearing effect vanishes at high- \hat{p}_T . As it was already mentioned, the \vec{k}_T -vector is a two dimensional quantity. The smearing in two dimensions will converge to the 1D smearing discussed above at very high p_T . The question of when is the p_T high enough that the perpendicular component may be neglected is, however, not easy to answer. The estimates of “the p_T magnitude has to be 3x larger then k_T ” are misleading. This can be easily demonstrated by use of simple monte carlo where random vectors of magnitude according to a power law or exponential function are generated and a random \vec{k}_T -vector of Gaussian magnitude is added. This corresponds to the 2D smearing procedure - see next section.

A.4.2 2D vector smearing.

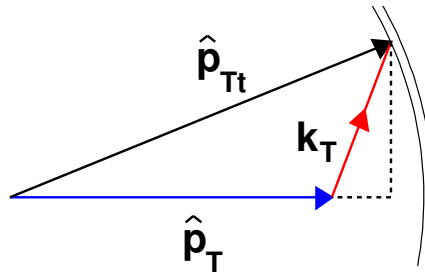


Figure 36: Hard scattered parton \hat{p}_T after experiencing a k_T -kick labeled as \hat{p}_{Tt} . The conditional probability $\mathcal{P}(\hat{p}_{Tt})|_{\hat{p}_T}$ corresponds to the contour integral reflecting all possible relative orientations of \hat{p}_T and \hat{p}_{Tt} .

Let us consider a parton of momentum \hat{p}_T and a \vec{k}_T -vector of 2D probability distribution

$$\mathcal{P}(k_T) = \frac{1}{2\pi \langle k_{Tx}^2 \rangle} \exp\left(-\frac{k_T^2}{2 \langle k_{Tx}^2 \rangle}\right) dk_T. \quad (67)$$

Here we consider the isotropic k_T -distribution where $\langle k_{Tx}^2 \rangle = \langle k_{Ty}^2 \rangle$. The “smeared” or final state parton is denoted as usually as \hat{p}_{Tt} . The smeared parton has a relative azimuthal angle $\Delta\phi$ with respect to \hat{p}_T (see Fig. 36).

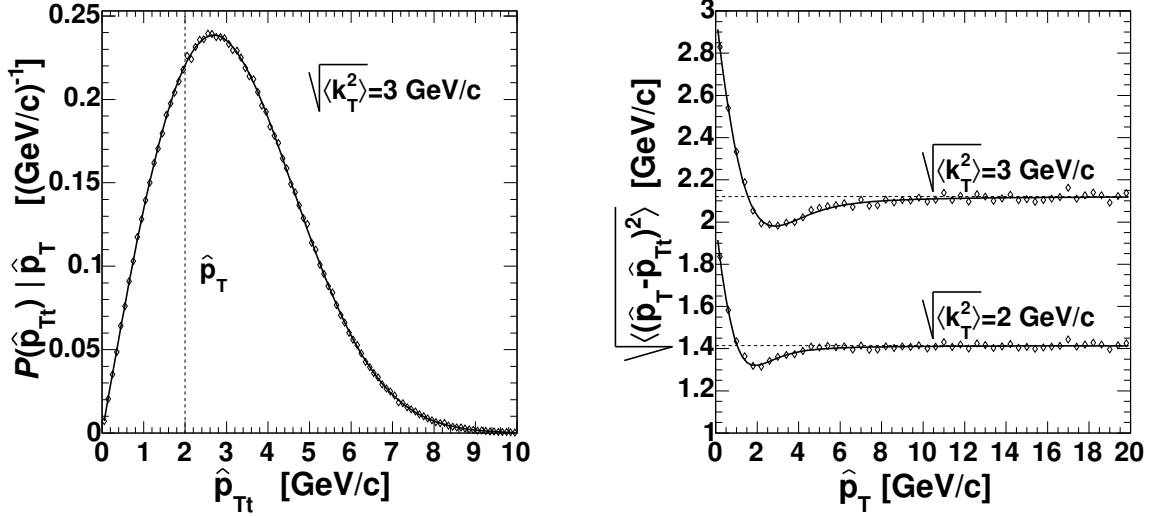


Figure 37: *Left*: Conditional probability distribution for smeared parton momenta originating from parent parton of the momentum $\hat{p}_T = 2$ GeV/c where the $\langle k_T^2 \rangle = 3$ GeV/c was used. Open diamonds simulation, solid line corresponds to Eq. (70). *Right*: Variance $\sqrt{\langle (\hat{p}_T - \hat{p}_{Tt})^2 \rangle}$ as a function of \hat{p}_T according Eq. (72) for two values of $\sqrt{\langle k_T^2 \rangle} = 2.0$ and 3.0 GeV/c.

Variance $\langle (\hat{p}_T - \hat{p}_{Tt})^2 \rangle$, which corresponds to the quantity σ_{sm} we are looking for can be evaluated analytically. We first decompose the \vec{k}_T -vector into its x and y components

$$k_T^2 = [\hat{p}_T^2 \sin^2(\Delta\phi) + (\hat{p}_T \cos(\Delta\phi) - \hat{p}_{Tt})^2] = \hat{p}_T^2 + \hat{p}_{Tt}^2 - 2\hat{p}_T \hat{p}_{Tt} \cos(\Delta\phi) \quad (68)$$

and the probability of finding parton \hat{p}_{Tt} given \hat{p}_T can be written as as a contour integral (see Fig. 36)

$$\mathcal{P}(\hat{p}_{Tt})|_{\hat{p}_T} = \frac{1}{2\pi \langle k_{Tx}^2 \rangle} \exp\left(-\frac{\hat{p}_T^2 + \hat{p}_{Tt}^2}{2 \langle k_{Tx}^2 \rangle}\right) \int_0^{2\pi} \exp\left(-\frac{\hat{p}_T \hat{p}_{Tt} \cos \Delta\phi}{2 \langle k_{Tx}^2 \rangle}\right) d\Delta\phi \hat{p}_{Tt} d\hat{p}_{Tt} \quad (69)$$

The last term corresponds to the modified Bessel function of the first kind, $2\pi I_0$ and the probability distribution can be written as

$$\mathcal{P}(\hat{p}_{Tt})|_{\hat{p}_T} = \frac{1}{\langle k_{Tx}^2 \rangle} \exp\left(-\frac{\hat{p}_T^2 + \hat{p}_{Tt}^2}{2 \langle k_{Tx}^2 \rangle}\right) I_0\left(\frac{\hat{p}_T \hat{p}_{Tt}}{\langle k_{Tx}^2 \rangle}\right) \hat{p}_{Tt} d\hat{p}_{Tt} \quad (70)$$

An excellent agreement between formula Eq. (70) and the simulated distribution for fixed $\hat{p}_T = 2$ GeV/c and $\langle k_T^2 \rangle = 3$ GeV/c is demonstrated by Fig. 37. Note that the shape of this function deviates from the Gaussian shape significantly, however, at $\hat{p}_T \gg k_T$ Eq. (70) resumes Gaussian shape.

The $\langle (\hat{p}_T - \hat{p}_{Tt})^2 \rangle$ value can be then calculated as

$$\langle (\hat{p}_T - \hat{p}_{Tt})^2 \rangle = \frac{\int_0^\infty (\hat{p}_T - \hat{p}_{Tt})^2 \mathcal{P}(\hat{p}_{Tt})|_{\hat{p}_T} d\hat{p}_{Tt}}{\int_0^\infty \mathcal{P}(\hat{p}_{Tt})|_{\hat{p}_T} d\hat{p}_{Tt}} \quad (71)$$

This integral has an analytic solution

$$\langle (\hat{p}_T - \hat{p}_{Tt})^2 \rangle = \frac{e^{-\xi}}{2\sqrt{\langle k_{Tx}^2 \rangle}} \left[4e^\xi \sqrt{\langle k_{Tx}^2 \rangle} (\langle k_{Tx}^2 \rangle + \hat{p}_T^2) - \hat{p}_T (2 \langle k_{Tx}^2 \rangle + \hat{p}_T^2) \sqrt{2\pi} I_0(\xi) - \hat{p}_T^3 \sqrt{2\pi} I_1(\xi) \right] \quad (72)$$

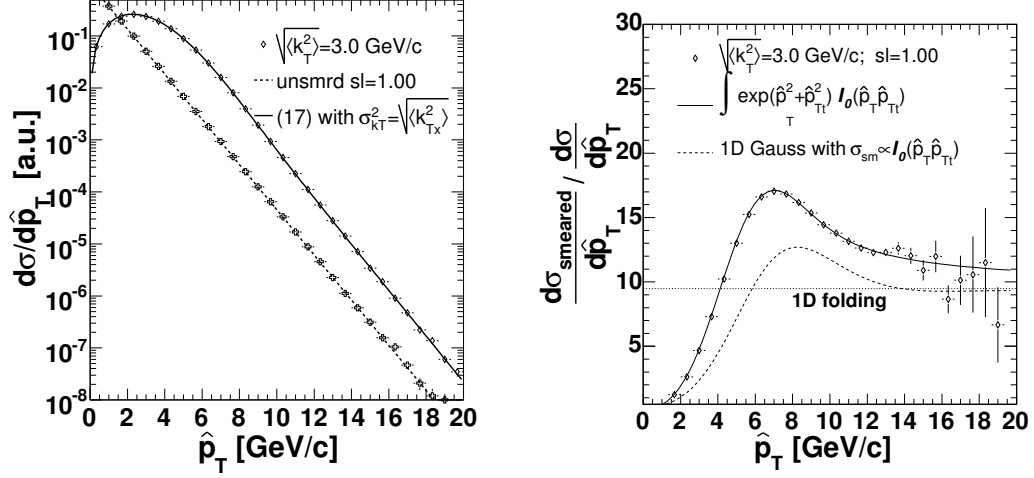


Figure 38: *Left*: Monte carlo simulated unsmeared (open crosses) and smeared (open diamonds) exponential distributions. The solid line correspond to the analytical smearing according Eq. (73). *Right*: The smeared/unsmeared ratio from simulation (open diamonds) and calculation according Eq. (73) (solid line). The usual 1D smearing according Eq. (15) with the variance σ_{sm} taken from Eq. (72) represented by dashed line. The dotted line represents Eq. (15) with constant variance $\langle k_{Tx}^2 \rangle$.

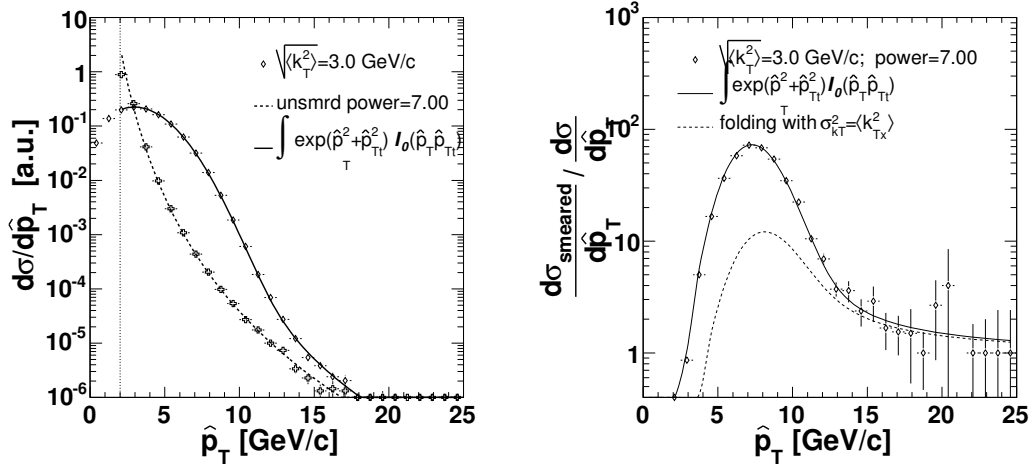


Figure 39: *Left*: Monte carlo simulated unsmeared (open crosses) and smeared (open diamonds) $1/\hat{p}_T^7$ distributions. The solid line correspond to the analytical smearing according Eq. (73). *Right*: The smeared/unsmeared ratio from simulation (open diamonds) and calculation according Eq. (73) (solid line). The 1D smearing according Eq. (15) with constant variance $\sigma_{sm} = \langle k_{Tx}^2 \rangle$.

where $\xi \equiv \hat{p}_T^2 / 4 \langle k_{Tx}^2 \rangle$.

The variance calculated according to Eq. (72) corresponds to the width of the Gaussian function used for k_T -smearing in Eq. (15). It is, obviously, p_T dependent. At low- \hat{p}_T where $\hat{p}_{Tt} \approx k_T$ the magnitude of $\sqrt{\langle (\hat{p}_T - \hat{p}_{Tt})^2 \rangle}$ should approach the $\sqrt{\langle k_T^2 \rangle}$ value and at high- \hat{p}_T limit $\sqrt{\langle k_{Tx}^2 \rangle}$ (see right panel of Fig. 37). This is also confirmed by simulations.

We thought that the the 1D smearing with p_T -dependent variance is the correct approach. However, the agreement between simulation and the improved folding Eq. (15) with σ_{sm} calculated according Eq. (72) is still not satisfactory (see the mismatch of dashed lines and simulations at Fig. 38 and Fig. 39). Surprisingly, the deviation

between 1D and 2D folding persists to relatively high transverse momenta. It is obvious that the transverse component k_{Ty} of the \vec{k}_T -vector cannot be neglected. In this case the usual 1D folding formula Eq. (15) is not a good approximation and an exact 2D formula

$$\Sigma'_Q(\hat{p}_{Tt}) = \int_0^\infty \Sigma_Q(\hat{p}_T) \mathcal{P}(\hat{p}_{Tt})|_{\hat{p}_T} d\hat{p}_T = \frac{\hat{p}_{Tt}}{\langle k_{Tx} \rangle} \int_0^\infty \Sigma_Q(\hat{p}_T) \exp\left(-\frac{\hat{p}_T^2 + \hat{p}_{Tt}^2}{2\langle k_{Tx}^2 \rangle}\right) I_0\left(\frac{\hat{p}_T \hat{p}_{Tt}}{\langle k_{Tx}^2 \rangle}\right) d\hat{p}_T \quad (73)$$

has to be used instead. 2D smearing calculated according Eq. (73) is represented by solid lines on Fig. 38 (for $\Sigma_Q(\hat{p}_T)$ =exponential function) and Fig. 39 ($\Sigma_Q(\hat{p}_T)$ =power law function). As one can see, the agreement is excellent! The variance used for this calculations corresponds to the $\langle k_{Tx}^2 \rangle$.

However, this is still not the end of the story. In reality, the \vec{k}_T -vector smearing has to preserve the invariant mass of the dijet system and this requirement leads to the correlation between \vec{k}_T -vectors on trigger and associated jet respectively. This calculation is discussed in 3.

A.4.3 Lorentz transform formulae

The net parton pair momentum $\vec{\hat{p}}_n$ is the vector sum of trigger and associated \vec{k}_T in the case on Lorentz non-invariant smearing where \vec{k}_{Ta} and \vec{k}_{Tt} are uncorrelated. In the case of Lorentz invariant smearing the \hat{p}_n is a scalar sum of the magnitude of k_{Ta} and k_{Tt} because in this case the two k_T -vectors are collinear (see Eq. (16) and Eq. (17)) and $\vec{\hat{p}}_n$ represents the boost vector from the parton CMS, where two jets are exactly back-to-back, to lab frame. The general Lorentz transform in two dimensions can be written as

$$\vec{\hat{p}}_{Tt} = \vec{\hat{p}}_T + \vec{\eta} \left(\frac{\vec{\eta} \cdot \vec{\hat{p}}_T}{1 + \gamma} + \hat{p}_{T0} \right)$$

where $\vec{\eta} = \gamma\vec{\beta}$ and \hat{p}_{T0} is the energy of the jet in the partonic CMS. We assume massless partons so $\hat{p}_{T0} = \hat{p}_T$. Let us rotate the dijet system in CMS such that trigger jet transverse momentum is $(\hat{p}_T, 0)$ and associated jet $(-\hat{p}_T, 0)$. The boost vector can be written as

$$\vec{\beta} = \frac{\vec{\hat{p}}_n}{E_n} \quad E_n = \sqrt{\hat{p}_n^2 + M_{inv}^2} = \sqrt{\hat{p}_n^2 + 4\hat{p}_T^2}$$

It is easy to see that

$$\vec{\eta} = \frac{\vec{\hat{p}}_n}{2\hat{p}_T} \quad \text{and} \quad \frac{1}{1 + \gamma} = \frac{2\hat{p}_n}{2\hat{p}_n + E_n}$$

and

$$\begin{aligned} \hat{p}_{Tt,x} &= \hat{p}_T + \frac{\hat{p}_n^2 \cos^2 \alpha}{2(2\hat{p}_T + E_n)} + \frac{\hat{p}_n}{2} \cos \alpha & \text{and} & \quad \hat{p}_{Tt,y} = \frac{\hat{p}_n^2 \sin \alpha \cos \alpha}{2(2\hat{p}_T + E_n)} + \frac{\hat{p}_n}{2} \sin \alpha \\ \hat{p}_{Ta,x} &= -\hat{p}_T - \frac{\hat{p}_n^2 \cos^2 \alpha}{2(2\hat{p}_T + E_n)} + \frac{\hat{p}_n}{2} \cos \alpha & \text{and} & \quad \hat{p}_{Ta,y} = -\frac{\hat{p}_n^2 \sin \alpha \cos \alpha}{2(2\hat{p}_T + E_n)} + \frac{\hat{p}_n}{2} \sin \alpha \end{aligned}$$

A.5 Fragmentation function with parton momentum

The parton distribution function is a steeply falling function of partons' momenta. However, when folded with the fragmentation function the distribution is less steep. In fact, the compensation of the falling trend of parton distribution by the rising fragmentation function $D(p_T/\hat{p}_T)$ takes place only in a limited momentum range due to the Jacobian when changing the variable $z \rightarrow \hat{p}_T$. In the simple case of the exponential shape of the fragmentation function we can write to probability distribution that the parton \hat{p}_T fragments with the momentum fraction z as

$$\left. \frac{d\mathcal{P}}{dz} \right|_{\hat{p}_T} = D(z) = \exp(-\lambda z) \frac{\lambda}{\exp(-\lambda x_T) - \exp(-\lambda)} \quad (74)$$

where the last term ensures the normalization. The probability that the fragment p_T is product of the fragmentation of the parton \hat{p}_T can be written as

$$\left. \frac{d\mathcal{P}}{d\hat{p}_T} \right|_{p_T} = D\left(\frac{p_T}{\hat{p}_T}\right) \cdot \frac{p_T}{\hat{p}_T^2} = \exp\left(-\frac{\lambda \cdot p_T}{\hat{p}_T}\right) \frac{\lambda \cdot p_T}{\hat{p}_T^2 (\exp(-\frac{2\lambda p_T}{\sqrt{s}}) - \exp(-\lambda))} \quad (75)$$

It is demonstrated in Fig. 40. The $D(\hat{p}_T)$ is rising only in the limited range below ≈ 10 GeV/c. Then the Jacobian of the $z \rightarrow \hat{p}_T$ turns the rising trend of $D(\hat{p}_T)$ into a steeply falling one. This feature eliminates the contribution

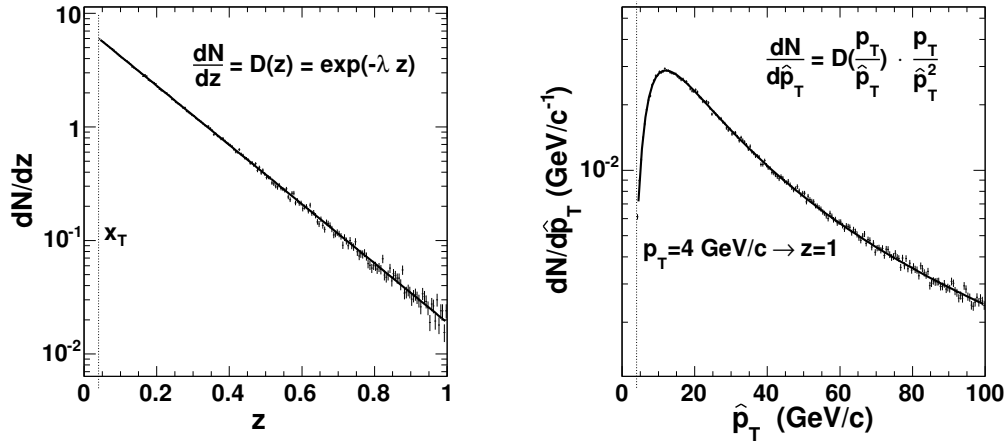


Figure 40: *Left*: Exponential fragmentation function $D(z) = \exp(-6z)$. *Right*: Fragmentation function as a function of \hat{p}_T .

of low z (high \hat{p}_T) partons.

A.6 π^0 reconstruction in run-3 data

For $\pi^0 - h^\pm$ correlations the sample of ERT triggered data was used. The event statistics are summarized in table 7.

BBCLL1	0.28 M
ERT_gamma1&BBCLL1	8.27 M
ERT_gamma2	7.69 M
ERT_gamma2&BBCLL1	2.10 M
ERT_gamma3&BBCLL1	47.12 M
ERT_gamma3&(BBCLL1 NTCLL1wide)	27.46 M
total	93.4 M

Table 7: Trigger statistics used for $\pi^0 - h^\pm$ analysis

All events were selected within the $\pm 30\text{cm}$ vertex cut and the same criteria as described in [1] were used for charged particle tracks. The EMCal hits with $E_{\text{cluster}} > 0.5 \text{ GeV}$, $\chi^2 < 3$ and photon pairs with the asymmetry $\alpha < 0.9$ were accepted.

Two examples of the invariant mass distribution $M_{\gamma\gamma}$ are shown on Fig. 42. The π^0 peak position depends on the transverse momentum of the γ -pair, $p_{T\gamma\gamma}$. It is due to the cluster overlapping at smaller opening angles and the details about that can be found elsewhere. For the purpose of this analysis, we just measure the π^0 peak position and width as a function of $p_{T\gamma\gamma}$ in the following way. For every $p_{T\gamma\gamma}$ bin the combinatorial background

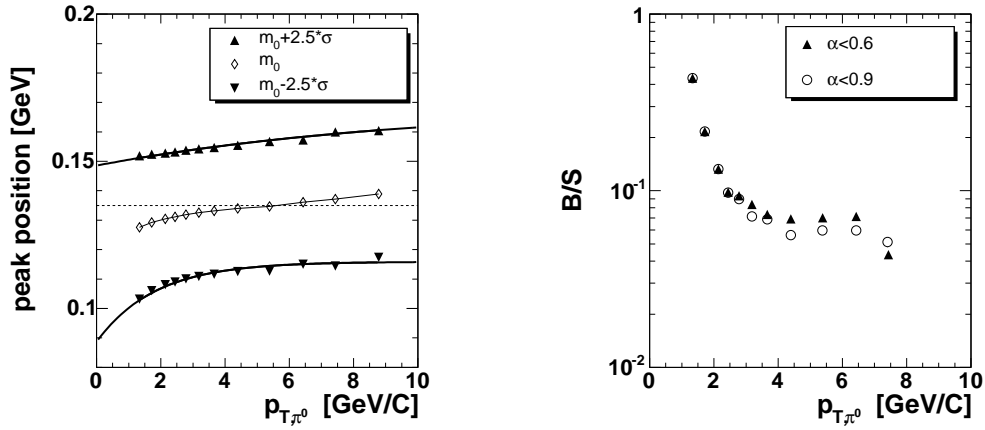


Figure 41: Left panel: the π^0 peak position and the width (2.5σ) as a function of $\pi^0 p_T$. The solid lines correspond to fit of Eq. (76). The dashed horizontal line denotes the tabulated π^0 mass. Right panel: the combinatorial background over the signal ratio for photon pairs with asymmetry $\alpha < 0.6$ and $\alpha < 0.9$

calculated using the mixed-event technique was subtracted and the residual peak is fitted by Gaussian function with the polynomial function of the first order which should account for the residual background distribution. The Gaussian integral is then compared to the integral of the unsubtracted spectrum within $\pm 2.5\sigma$ mass interval. The π^0 peak position, $m_0(p_{T\pi^0})$ and width $\sigma(p_{T\pi^0})$ are shown on Fig. 41. The combinatorial background over the signal ratio for photon pairs with two different asymmetry cuts are show on the right panel of Fig. 41. It is obvious that the majority ($> 94\%$) of γ -pair, in case of low multiplicity pp collisions, are coming from the π^0 decays and above 2 GeV/c, the contribution of the combinatorial background can be neglected.

The range of photon-pair mass $M_{\gamma\gamma}^\pm(p_{T\gamma\gamma})$ where photon pairs from π^0 decays dominate as a function of $p_{T\gamma\gamma}$ was parametrized by

$$M_{\gamma\gamma}^\pm(p_{T\gamma\gamma}) = e^{a-bp_{T\gamma\gamma}} + c \quad (76)$$

where a, b and c are free parameters determined from the fit to the measured $m_0(p_{T\pi^0}) \pm 2.5\sigma(p_{T\pi^0})$ distributions (see Tab. 8).

	$m_0 - 2.5\sigma$	$m_0 + 2.5\sigma$
a =	0.116	0.169
b =	-0.027	-0.020
c =	0.549	0.101

Table 8: Extracted fit parameter of Eq. (76) to $m_0(p_{T\pi^0}) \pm 2.5\sigma(p_{T\pi^0})$ distributions shown at Fig. 41

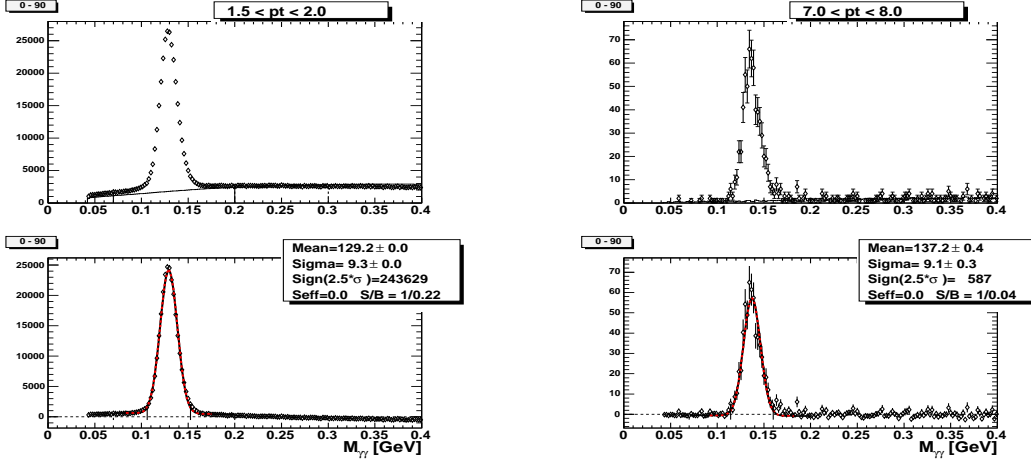


Figure 42: Two-photon invariant mass distribution for $1.5 < p_{T\gamma\gamma} < 2.0$ GeV/c (left panels) and $7.0 < p_{T\gamma\gamma} < 8.0$ (right panels). Upper plots show the raw $M_{\gamma\gamma}$ and mixed event distributions, lower panel shows the subtracted distributions. The asymmetry cut of 0.9 was applied.

Later in the analysis, the photon pair was accepted as π^0 decay product only if $M_{\gamma\gamma}$ of this pair was found to be within $M_{\gamma\gamma}^-(p_{T\gamma\gamma}) < M_{\gamma\gamma}(p_{T\gamma\gamma}) < M_{\gamma\gamma}^+(p_{T\gamma\gamma})$ boundary. The correlation functions are presented in section 1.2.

A.7 Data tables

Table 9: The σ_N and σ_A values shown on right panel of Fig. 7. All units in rad and GeV/c.

p_{Tt}	σ_N	σ_A
2.23	0.247 ± 0.002	0.565 ± 0.013
2.72	0.227 ± 0.003	0.548 ± 0.014
3.22	0.235 ± 0.004	0.521 ± 0.016
3.89	0.215 ± 0.004	0.464 ± 0.014
4.90	0.210 ± 0.006	0.431 ± 0.020
5.91	0.197 ± 0.009	0.396 ± 0.025
7.23	0.185 ± 0.012	0.350 ± 0.028

Table 10: The $\sqrt{\langle p_{\text{out}}^2 \rangle}$ values shown on Fig. 9. All units in GeV/c.

$1.4 < p_{T_a} < 5.0$		$3 < p_{T_t} < 4$		$5 < p_{T_t} < 10$	
p_{T_t}	$\sqrt{\langle p_{\text{out}}^2 \rangle}$	p_{T_a}	$\sqrt{\langle p_{\text{out}}^2 \rangle}$	p_{T_a}	$\sqrt{\langle p_{\text{out}}^2 \rangle}$
2.23	1.315 ± 0.043	1.72	0.996 ± 0.056	1.85	0.960 ± 0.102
2.72	1.250 ± 0.046	2.22	1.244 ± 0.079	2.24	1.100 ± 0.103
3.22	1.182 ± 0.049	2.73	1.222 ± 0.095	2.73	1.088 ± 0.110
3.89	1.011 ± 0.038	3.23	1.496 ± 0.105	3.44	1.285 ± 0.136
4.90	0.953 ± 0.052	3.93	1.793 ± 0.115	4.65	1.268 ± 0.210
5.91	0.868 ± 0.064	5.04	1.675 ± 0.141		
7.24	0.798 ± 0.068				

Table 11: The $\sqrt{\langle j_T^2 \rangle}$ values shown on Fig. 8. All units in rad and GeV/c.

$1.4 < p_{T_a} < 5.0$		$3 < p_{T_t} < 4$		$4 < p_{T_t} < 5$		$5 < p_{T_t} < 6$	
p_{T_t}	$\sqrt{\langle j_T^2 \rangle}$	p_{T_a}	$\sqrt{\langle j_T^2 \rangle}$	p_{T_a}	$\sqrt{\langle j_T^2 \rangle}$	p_{T_a}	$\sqrt{\langle j_T^2 \rangle}$
3.22	0.587 ± 0.009	1.72	0.562 ± 0.011	1.72	0.643 ± 0.036	1.52	0.529 ± 0.030
3.89	0.577 ± 0.009	2.22	0.597 ± 0.014	2.14	0.492 ± 0.032	2.22	0.581 ± 0.049
4.90	0.600 ± 0.017	2.73	0.572 ± 0.017	2.53	0.608 ± 0.035	2.88	0.590 ± 0.047
5.91	0.596 ± 0.026	3.23	0.590 ± 0.020	3.17	0.590 ± 0.032	4.01	0.603 ± 0.063
7.24	0.597 ± 0.038	3.93	0.603 ± 0.017	4.36	0.631 ± 0.052		
8.34	0.632 ± 0.085	5.04	0.506 ± 0.029				

Table 12: The near and away side conditional yield per number of triggers for $1.4 < p_{T_a} < 5.0$ GeV/c shown on Fig. 11. All units in rad and GeV/c.

p_{T_t}	Y_N	Y_A
2.23	1.911 ± 0.018	1.717 ± 0.044
2.72	1.863 ± 0.022	1.908 ± 0.055
3.22	2.032 ± 0.032	2.130 ± 0.071
3.89	1.966 ± 0.033	2.360 ± 0.074
4.90	2.120 ± 0.061	2.611 ± 0.123
5.91	2.153 ± 0.098	2.992 ± 0.196
7.24	2.174 ± 0.125	3.690 ± 0.242

Table 13: The $\hat{x}_h^{-1} \langle z_t \rangle \sqrt{\langle k_T^2 \rangle}$ values shown on Fig. 10. All units in rad and GeV/c.

$1.4 < p_{T_a} < 5.0$		$3 < p_{T_t} < 4$		$5 < p_{T_t} < 10$	
p_{T_t}	$\hat{x}_h^{-1} \langle z_t \rangle \sqrt{\langle k_T^2 \rangle}$	p_{T_a}	$\hat{x}_h^{-1} \langle z_t \rangle \sqrt{\langle k_T^2 \rangle}$	p_{T_a}	$\hat{x}_h^{-1} \langle z_t \rangle \sqrt{\langle k_T^2 \rangle}$
2.23	1.279 ± 0.051	1.72	1.760 ± 0.124	1.85	2.695 ± 0.369
2.72	1.501 ± 0.066	2.22	1.736 ± 0.131	2.24	2.537 ± 0.309
3.22	1.630 ± 0.083	2.73	1.373 ± 0.130	2.73	2.130 ± 0.261
3.89	1.664 ± 0.077	3.23	1.449 ± 0.120	3.44	1.894 ± 0.270
4.90	1.889 ± 0.132	3.93	1.440 ± 0.107	4.65	1.413 ± 0.300
5.91	2.062 ± 0.193	5.04	1.041 ± 0.104		
7.24	2.175 ± 0.246				
8.34	2.529 ± 0.617				

B Glossary of used symbols

p_{Tt}	- trigger particle p_T
p_{Ta}	- associated particle p_T
\hat{p}_T	- parton p_T
\hat{p}_{Ta}	- p_T of the parton from which the associated particle was produced
\hat{p}_{Tt}	- p_T of the parton from which the trigger particle was produced
$\langle k_T \rangle$	- 2D mean of k_T -vector
$\langle k_{Ty} \rangle$	- 1D mean absolute of k_T -vector y -projection
$\langle k_T^2 \rangle$	- 2D RMS of k_T -vector
k_{Tt}	- magnitude of \vec{k}_{Tt} vector associated with trigger jet
k_{Ta}	- magnitude of \vec{k}_{Ta} vector associated with away-side jet
$\langle j_T \rangle$	- 2D mean of j_T -vector
$\langle j_{Ty} \rangle$	- 1D mean absolute of j_T -vector y -projection
$\langle j_T^2 \rangle$	- 2D RMS of j_T -vector
z_t	- momentum fraction of parton's p_T taken away by trigger state particle
z_a	- momentum fraction of parton's p_T taken away by associated state particle
x_h	- p_{Ta}/p_{Tt} ratio of the associated particle momentum over the trigger particle momentum
\hat{x}_h	- $\hat{p}_{Ta}/\hat{p}_{Tt}$ ratio of the associated jet momentum over the trigger jet momentum
D_π^q	- fragmentation function
$f_Q(\hat{p}_T)$	- k_T -unsmeared final state parton invariant spectrum
$f'_Q(\hat{p}_{Tt})$	- k_T -smeared final state parton invariant spectrum
$\Sigma_Q(\hat{p}_T)$	- k_T -unsmeared final state parton cross section \hat{p}_T -distribution
$\Sigma'_Q(\hat{p}_{Tt})$	- k_T -smeared final state parton cross section \hat{p}_T -distribution
σ_{sm}	- variance of the Gaussian smearing function

References

- [1] analysis note #251.
- [2] P. Levai *et al* “Dijet correlations at ISR and RHIC energies” hep-ph/0502238.
- [3] PHENIX measurement of jet properties and their modification in heavy-ion collisions, J. Rak for the PHENIX collaboration, Submitted to J.Phys.G., hep-ex/0403038.
- [4] Angelis, A. L. S. and others, CCOR collaboration, Phys. Lett., B97 (1980).
- [5] Feynman, R. P. and Field, R. D. and Fox, G. C., Nucl. Phys., **B128** (1977).
- [6] M. J. Tannenbaum, analysis note #221.
- [7] G. W. van Apeldoorn *et al.*, Nucl. Phys. **B91**, 1 (1975).
- [8] M. J. Tannenbaum,
<http://www.phenix.bnl.gov/phenix/WWW/publish/sapin/spin/talks/discussion99/evgenwks99plus.pdf>
- [9] V. S. Pantuev; analysis note #288.
- [10] S. S. Adler *et al.*, hep-ex/0304038.
- [11] U.A. Wiedemann; hep-ph/0406319.
- [12] W. Vogelsang, private communication.
- [13] B. A. Kniehl, G. Kramer, and B. Potter Nuclear Physics **B 582** (2000) 514-536.
- [14] P. Abreu *et al.*, Eur. Phys. J. C13, 573 (2000).
G. Alexander *et al.*, Z. Phys. C69, 543 (1996).
- [15] L. Apanasevich *et al.*, Phys. Rev. **D59**, 074007 (1999).
- [16] R. P. Feynman, R. D. Field, and G. C. Fox, Phys. Rev. **D18**, 3320 (1978).
- [17] A. L. S. Angelis *et al.*, Nucl. Phys. **B209**, 284 (1982).